

MODELING INERTIAL MEASUREMENT UNITS AND ANALYZING THE
EFFECT OF THEIR ERRORS IN NAVIGATION APPLICATIONS

Except where reference is made to work of others, the work described in this thesis is my own or was done in collaboration with my advisory committee. This thesis does not include proprietary or classified information

Warren S. Flenniken, IV

Certificate of Approval:

A. Scottedward Hodel
Associate Professor
Electrical and Computer Engineering

David M. Bevly, Chair
Assistant Professor
Mechanical Engineering

George T. Flowers
Professor
Mechanical Engineering

Stephen L. McFarland
Dean
Graduate School

MODELING INERTIAL MEASUREMENT UNITS AND ANALYZING THE
EFFECT OF THEIR ERRORS IN NAVIGATION APPLICATIONS

Warren S. Flenniken, IV

A Thesis

Submitted to

the Graduate Faculty of

Auburn University

in Partial Fulfillment of the

Requirements for the

Degree of

Masters of Science

Auburn, Alabama
December 16, 2005

MODELING INERTIAL MEASUREMENT UNITS AND ANALYZING THE
EFFECT OF THEIR ERRORS IN NAVIGATION APPLICATIONS

Warren S. Flenniken, IV

Permission is granted to Auburn University to make copies of this thesis at
its discretion, upon the request of individuals or institutions and
at their expense. The author reserves all publication rights.

Signature of the Author

Date of Graduation

THESIS ABSTRACT

MODELING INERTIAL MEASUREMENT UNITS AND ANALYZING THE EFFECT OF THEIR ERRORS IN NAVIGATION APPLICATIONS

Warren S. Flenniken, IV

Master of Science, December 16, 2005
(B.A., Auburn University, 2005)
(B.M.E., Auburn University, 2000)
(B.A., Auburn University, 1998)

165 Typed Pages

Directed by David M. Bevly

In this thesis, a simple model that statistically represents an Inertial Measurement Unit (IMU) output has been studied. This model is then expanded to produce a model that incorporates terms that account for errors associated with high dynamics. Several techniques are used to determine the error statistics of the IMU model and categorize the performance of the IMU. These techniques include Allan variance charts, Monte Carlo simulations and autocorrelation functions. Equations for the position, velocity and heading error in a two and six degree of freedom system are developed. These analytical equations for the error growth are then verified using Monte Carlo simulations. Monte Carlo simulations are also used to compare the error bounds using both the simple model and high dynamic model. A novel Kalman filter is developed to couple GPS with an inertial measurement unit in order to bound the error growth. The Kalman filter estimates both a constant and drifting bias. The error bounds on the position, velocity and heading state estimations are compared to the error bounds in the simple model's uncoupled case. The framework formulated from these models is intended as an aid for understanding the effects that the different error sources have on position, velocity, and

heading calculations. With this information it is possible to determine the correct inertial measurement unit with identified error characteristics for a specific application.

ACKNOWLEDGEMENTS

I would first like to thank my advisor, Dr. David M. Bevly, for his guidance and knowledge over the last two years. I would also like to thank everyone in my lab for their assistance.

I would like to thank my wife, Shellie M. Flenniken, for giving me two wonderful sons, Warren S Flenniken V and Mitchell Scott Flenniken, during my graduate school tour. You are a wonderful and patient wife, and I will always love you for that.

For their financial and emotional support throughout my life, I would like to thank my parents, Warren S. Flenniken, III and Ellen Crawford Flenniken. Without you, I would have never been able to pursue this goal.

I would like to thank my brother, Jason Crawford Flenniken, for his companionship during the retreats to Spur Ranch. They were much needed and appreciated.

I would like to thank my in-laws, S. Felton Mitchell and L. Ann Mitchell for their financial and emotional support, as well. Both of you have been great and I will always remember it.

Finally I am dedicating this work to my grandfather, Warren S Flenniken, II, who passed away September 20, 2003. He was a great man and wonderful role model. He is missed by all that knew him.

Style of Journal Used:

ASME Journal of Dynamic Systems, Measurement, and Control

Computer Software Used:

Microsoft Word 2002

TABLE OF CONTENTS

LIST OF FIGURES.....	xi
LIST OF TABLES.....	xiv
1. INTRODUCTION	
1.1 Motivation.....	1
1.2 Background and Literature Review.....	2
1.3 Purpose.....	3
1.4 Outline.....	4
2. SIMPLE SENSOR MODELING	
2.1 Introduction.....	6
2.2 Sensor Model.....	7
2.3 Random Walk Evaluation.....	9
2.4 Walking Bias Evaluation.....	14
2.5 Constant Bias Evaluation.....	16
2.6 Rate Gyro Model Validation.....	16
2.7 Accelerometer Model Validation.....	21
2.8 Sensor Categorization.....	24
2.9 Summary and Conclusion.....	30
3. INTEGRATION ERRORS OF A TWO DEGREE OF FREEDOM IMU	
3.1 Introduction.....	31
3.2 IMU Integration Error.....	32

3.3	Monte Carlo Validation.....	40
3.4	Longitudinal Velocity Error Equations.....	43
3.5	Longitudinal Position Error Equations.....	45
3.6	Lateral Velocity Error Equations.....	46
3.7	Lateral Position Error Equations.....	48
3.8	Bias Contribution in the IMU Integration Errors.....	50
3.9	Gravitational Effects.....	55
3.10	Summary and Conclusion.....	60

4. INTEGRATION ERROR CORRECTIONS FOR A TWO DOF IMU

4.1	Introduction.....	61
4.2	Heading Error Reduction with a Two State Kalman Filter.....	61
4.3	Heading Error during a GPS Outage.....	67
4.4	Heading Error Reduction with a Three State Kalman Filter.....	72
4.5	Kalman Filter Comparisons.....	74
4.6	Position Estimation with a Six State Kalman Filter.....	78
4.7	Summary and Conclusion.....	81

5. INTEGRATION ERRORS OF A SIX DEGREE OF FREEDOM IMU

5.1	Introduction.....	82
5.2	Six Degree of Freedom Inertial Measurement Unit Model.....	82
5.3	Six Degree of Freedom Inertial Measurement Unit Integration.....	87
5.4	Six Dof IMU Integration Heading Errors.....	91
5.5	Six Dof IMU Integration Velocity Errors.....	93
5.6	Six Dof IMU Integration Position Errors.....	95
5.7	Summary and Conclusion.....	97

6. ADVANCED SENSOR MODELING

6.1	Introduction.....	99
6.2	The Inertial Measurement Unit Accelerometer Triad Error Model.....	99
6.3	The Inertial Measurement Unit Rate Gyro Triad Error Model.....	101
6.4	Model Error Parameter Descriptions.....	104
6.5	Inertial Measurement Unit Initialization Errors.....	107
6.6	Summary and Conclusion.....	110
7.	INTEGRATION ERRORS OF AN ADVANCED IMU MODEL	
7.1	Introduction.....	111
7.2	Launch Trajectory Profile.....	111
7.2	Comparison of the Simple and Advanced IMU Models.....	114
7.3	Advanced Model Error Parameter Contribution Levels.....	116
7.4	Summary and Conclusion.....	118
8.	CONCLUSIONS	
8.1	Summary.....	119
8.2	Recommendation for Future Work.....	122
	REFERENCES.....	124
	APPENDICES.....	128
A	The Allan Variance.....	129
B	Markov Process Statistics.....	135
C	An Introduction to the Kalman Filter.....	141
D	The Autocorrelation Function.....	146

LIST OF FIGURES

2.1	KVH-5000 Experimental Data Filtered and Unfiltered.....	10
2.2	Allan Variance Chart for the Unfiltered Experimental Data of the KVH- 5000.....	11
2.3	AQRS-104 Experimental Data Filtered and Unfiltered.....	12
2.4	Allan Variance Chart for the Unfiltered Experimental Data of the AQRS- 104.....	13
2.5	AQRS-104 Experimental Autocorrelation Plot.....	15
2.6	Allan Variance Comparison I of the KVH 5000 Experimental and Simulated Data.....	17
2.7	Allan Variance Comparison II of the KVH 5000 Experimental and Simulated Data.....	18
2.8	Allan Variance Comparison of the AQRS-104 Experimental and Simulated Data.....	19
2.9	AQRS-104 Autocorrelation Comparison of the Filtered Experimental Data..	20
2.10	Humphrey Accelerometer Actual Data filtered and Unfiltered Data.....	21
2.11	Humphrey Accelerometer Autocorrelation of the Filtered Experimental Data.....	23
2.12	Allan Variance Comparison of the Humphrey Accelerometer Experimental and Simulated Data.....	24
3.1	Tactical Grade IMU Position Error Bounds (Static).....	34
3.2	Tactical Grade IMU Velocity Error Bounds (Static).....	35
3.3	Tactical Grade IMU Heading Error Bounds (Static).....	36
3.4	Consumer Grade IMU Position Error Bounds (Static).....	37
3.5	Consumer Grade IMU Velocity Error Bounds (Static).....	38
3.6	Consumer Grade IMU Heading Error Bounds (Static).....	39

3.7	KVH Error Bound Comparison I.....	41
3.8	KVH Error Bound Comparison II.....	42
3.9	KVH Error Bound Comparison III.....	43
3.10	Comparison of a Tactical Grade IMU Position Error Bounds (Static).....	51
3.11	Comparison of a Tactical Grade IMU Velocity Error Bounds (Static).....	52
3.12	Effect of Tactical Grade IMU Biases on Position Error (Static).....	53
3.13	Effect of Tactical Grade IMU Biases on Velocity Error (Static).....	54
3.14	Tactical Grade IMU Position Error Bounds with Gravity Field.....	56
3.15	Tactical Grade IMU Velocity Error Bounds with Gravity Field.....	57
3.16	Consumer Grade IMU Position Error Bounds with Gravity Field.....	58
3.17	Consumer Grade IMU Velocity Error Bounds with Gravity Field.....	59
4.1	Consumer Grade Heading Error Comparison between the 2 state Kalman Filter Model and Rugge-Kutta Order Four.....	65
4.2	Tactical Grade Heading Error Comparison between the 2 state Kalman Filter Model and Rugge-Kutta Order Four.....	66
4.3	State Estimates for a Two State Kalman Filter with the Second State Modeled as a 1 st Order Markov Process.....	68
4.4	State Estimates for a Two State Kalman Filter with the Second State Modeled as a Random Walk.....	69
4.5	Error Bound Comparison between the Two State Kalman Filter Models when the Dominate Bias is not Constant.....	70
4.6	Error Bound Comparison between the Two State Kalman Filter Models when the Dominate Bias is a Constant.....	71
4.7	Consumer Grade Heading Error Comparison between the 3 State Kalman Filter Model, the 2 State Kalman Filter Model and A Rugge-Kutta Order Four Integration Method.....	74
4.8	Systron-Donner State Estimates for a Two State Kalman Filter with the Second State Modeled as a Random Walk.....	75
4.9	Systron-Donner State Estimates for a Two State Kalman Filter with the Second State Modeled as a 1 st Order Markov Process.....	76

4.10	Systron-Donner State Estimates for a Three State Kalman Filter with the Second State Modeled as a 1 st Order Markov Process and the Third State Modeled as a Random Walk.....	78
5.1	Definition of the Six Degrees of Freedom.....	83
5.2	Heading Error in a Six DoF Tactical Grade IMU.....	92
5.3	Heading Error in a Six DoF Consumer Grade IMU.....	93
5.4	Velocity Errors in a Six DoF Tactical Grade IMU.....	94
5.5	Velocity Error in a Six DoF Consumer Grade IMU.....	95
5.6	Position Error in a Six DoF Tactical Grade IMU.....	96
5.7	Position Error in a Six DoF Consumer Grade IMU.....	97
6.1	Inertial Measurement Unit Input/Output Error Types.....	104
6.2	Inertial Measurement Unit Triad Misalignment.....	105
6.3	Inertial Measurement Unit Triad Nonorthogonality.....	106
6.4	Initialization Vectors of the Body Coordinate Frame.....	109
7.1	Rocket Launch Trajectory I: Body Accelerations, Body Headings and ENU Velocities.....	113
7.2	Rocket Launch Trajectory I Altitude Vs. Range.....	114
7.3	Rocket Launch Trajectory Impact Point Scatter Plot.....	115
7.4	Rocket Launch Trajectory I Error Parameters Contribution Levels.....	117

LIST OF TABLES

2.1	Accelerometer Characteristics Used for this Analysis.....	25
2.2	Classification Characteristics Used to Categorize Accelerometers.....	26
2.3	Gyro Characteristics Used for this Analysis.....	27
2.4	Classification Characteristics Used to Categorize Rate Gyros.....	29
6.1	Advanced IMU Error Parameters.....	102
6.2	IMU Initialization Error Parameters.....	108

CHAPTER 1

INTRODUCTION

1.1. Motivation

When an instrument is used to collect data, the measurement obtained from that device is always corrupted by some error sources. Some of these errors are constant, some have known frequency content, and some are random. These errors are common in instruments used to calculate position, velocity, or heading of a vehicle. Because the errors are in the instruments measurement, it is inevitable that the calculations will contain errors.

A common technique used to calculate position, velocity, and heading of a vehicle is dead reckoning. One form of dead reckoning is to document an initial position, velocity, and heading relative to some known coordinate frame and then measure the accelerations and rotation rates of the vehicle versus time. As the accelerations and rotation rates are measured, they are integrated to calculate the vehicle's position, velocity, and heading. Because the acceleration and rotation rate measurements are noisy or imprecise, the calculated position, velocity, and heading will contain errors as well. This work is an analysis of these errors and how we as engineers can evaluate them, classify them, and remove them from the position, velocity, and heading calculations when accelerometers and rate gyros are used to dead reckon.

1.2. Background and Literature Review

Position, velocity and heading calculations have errors. In order to compensate for these errors, the errors found in the accelerometer and rate gyro used must be identified. A simple model has been developed that does this [Demoz]. The simple model classifies the common errors found in accelerometers and rate gyros into three categories: a constant offset error source, a moving bias error source and a random error source. A procedure has also been developed to obtain the statistics of each of these error sources. When the statistical values for each of the error sources are known, it is possible to use the simple model to statistically simulate an accelerometer's or rate gyro's output.

The outputs of rate gyros are normally integrated to obtain a heading estimate. Because the rate gyro measurements have errors, the calculated heading will contain errors as well. Error equations that depict the growth of the error in the heading calculation have been derived [Bevly]. However, these error equations were derived with the assumption that the rate gyro has only one error source, wide band noise. The value of this error model is that it may be used to obtain an estimation of the standard deviation of the heading estimate error over time.

The simple sensor model used to statistically represent the output of an accelerometer and rate gyro has been used in conjunction with the Global Position System to bound the errors found in position, velocity and heading calculations [Demoz]. A two state Kalman filter is used to estimate heading, and a five state Kalman filter is used to estimate position and velocity. In each of these filters, the error sources are assumed to be wide-band noise and either a moving bias error or a constant offset error.

More advanced models have been developed that incorporate errors that are affected by the true accelerations or rotation rates [Grewal]. These errors include scale factor errors, misalignment errors and nonorthogonality errors.

1.3. Purpose

The primary purpose of this work is to use the existing simple sensor model to identify the common error sources found in accelerometers and rate gyros, and then validate the procedure used to evaluate the statistical properties of each of these error sources. The simple model is then used to classify accelerometers and rate gyros into different grades. Error bounds of some component grades are provided which can be used to determine the utility of a specific grade sensor.

The second purpose of this work is to develop Kalman filter models that contain enough states so that all the errors in the simple sensor model can be estimated. With these Kalman filter models, it is shown that the errors during a loss of a GPS signal are minimized when compared to the existing Kalman filter models. A Kalman Filter is a state estimator that uses the knowledge of the input error sources to assist in estimating the true state over time. It is an ideal coupling tool to use in this scenario due to the fact that the GPS measurements are very precise but are received at a very low frequency, and the IMU measurements are relatively imprecise and can be received at relatively high frequencies when compared to GPS.

The third purpose of this work is the evaluation of the effects gravity has on a group of accelerometers and rate gyros when used in an inertial measurement unit. The

error growths of the position, velocity and heading calculation are shown when a gravity field is in place, and then the error growths are shown when the gravity field is removed. The comparison reveals the effect a gravity field has on an inertial measurement unit's total error.

The final purpose of this work is to identify the effects the error terms found in the more advanced sensor models have on the position, velocity and heading calculations [Grewal]. Simulated trajectories will be used to evaluate the contribution level each of these errors has on the calculated position, velocity, and heading. The simulated trajectories are designed to be somewhat practical and still excite the advanced sensor model's error terms

1.4. Outline

In this thesis a simple sensor model is first defined that is used to classify error sources commonly found in accelerometers and rate gyros. Many error sources are incorporated in the model; they include a constant bias error source, a moving bias error source, and a random error source. The model is used to statistically simulate the output of an accelerometer and rate gyro [Demoz]. Each term in the simple model will be described statistically in the form of norms and variances.

In this work a navigation technique known as dead reckoning is then used to determine a vehicle's position on the earth. Dead reckoning is the determination, without the aid of celestial observations, of the position of a ship or aircraft from the record of the courses sailed or flown, the distance made, and the known or estimated drift [Webster].

The position is calculated by integrating three accelerometers and three rate gyroscopes mounted to the vehicle platform. These sensor packages are commonly referred to as inertial measurement units or IMU's. The category of the sensors contained in the IMU determines the precision of the corresponding vehicle's position estimate. The dead reckoning technique is analyzed to determine the magnitude of the errors in the position, velocity and heading calculations. The magnitude of the error is then analyzed to determine how it is affected by the different error sources found in accelerometers and rate gyros

Using the simple sensor model, a one and two degree of freedom system simulations are set up to predict the error growth of tactical and consumer grade sensors. The Global Position System or GPS is used to correct the IMU position errors in a coupling algorithm. The algorithm chosen to couple the GPS and IMU's measurements is a Kalman Filter. Experimental data is used to show the utility of the Kalman filter models.

Finally, in this thesis a six degree of freedom system is developed. It is used to show the error growth of position velocity and heading over time. The accuracy of the simple model as well as a more advanced model is shown. The effects of each of the advanced IMU model's parameters are taken into account as well as the introduction of a gravity field. A Monte Carlo Simulation is used to show the bounds on the error growths for the position, velocity and heading calculations.

CHAPTER 2

SIMPLE SENSOR MODEL

2.1 Introduction

In this chapter a simple sensor model is laid out that incorporates three common error sources. They are a moving bias, a constant bias, and a random error. Other error sources such as gravitational errors, cross-coupling errors and sensor scale factor errors are considered in later chapters. In this chapter the biases and random error sources are analyzed statistically. The numerical values for the time constants, means, and variances are obtained by using common statistical methods, Allan variance charts, autocorrelation functions, and Monte Carlo simulations. The statistical parameters of the error sources are used to categorize and characterize the sensors. Inertial sensors can be categorized into four basic grades: navigational, tactical, automotive, and consumer. While the navigation sensors are the most precise they also cost the most at around \$100,000. The tactical sensors cost in the \$20,000 range, the automotive cost in the \$1,000 range and the consumer sensors, the least precise cost less than \$1,000. Several sensor grades are simulated and experimentally validated. The simulated sensors are used in later chapters to determine resulting levels of performance that can be achieved when combined with GPS. A table is provided at the end of this chapter which contains a number commonly

used in rate gyros and accelerometers with their specifications. An additional chart is provided that is used to classify the sensors into the grades mentioned above.

2.2 Sensor Model

One simple model of a gyro assumes that the gyro output (g_r) consists of the true vehicle rotation rate (r) plus a constant offset (c_r), a moving or walking bias (b_r), and wide band sensor noise (w_{gyro}). It is shown below.

$$g_r = r + c_r + b_r + w_{gyro} \quad (2.1)$$

The wide band sensor noise (w_{gyro}) is assumed to be normally distributed with a zero mean and sampled covariance

$$E[w_{gyro}^2] = \sigma_{gyro}^2 f_s \quad (2.2)$$

Observe in Equation (2.2) that wide band noise increases as the sample rate (f_s) of the sensor increases [Demoz]. The gyros moving bias (b_r) will be modeled as a first order Markov process. The Markov process takes in account the sampling frequency of the sensor. This is shown in Equations (2.3 – 2.5). For a more explicit definition of a first order Markov Process see Appendix B.

We assume the moving bias has the following statistics.

$$E[b_r] = 0 \text{ and } E[b_r^2] = \sigma_{gyro\,bias}^2 \quad (2.3)$$

and that

$$\dot{b}_r = -\frac{1}{\tau_r} b_r + w_{gyro\,bias} \quad (2.4)$$

where

$$w_{gyro\,bias} = \sqrt{\frac{2f_s \sigma_{gyro\,bias}^2}{\tau_r}} v \quad (2.5)$$

The noise that drives the bias, v , is normally distributed with zero mean and a sampled covariance of one.

$$v \sim N[0,1] \quad (2.6)$$

An Allan variance and autocorrelation analysis is used to determine the time constant (τ_r), random walk (σ_{gyro}), and bias variation ($\sigma_{gyro\,bias}$). The numerical values are evaluated with experimental data and verified with the manufactures specifications and documents containing published values. Once this method is validated, it is used for future analysis when exact sensor specifications are not known.

An accelerometer is modeled in the same fashion as a rate gyro. A simple model that relates the accelerometer output ($a_{\ddot{x}}$) to the true vehicle acceleration (\ddot{x}), a constant offset or bias ($c_{\ddot{x}}$), a moving or walking bias ($b_{\ddot{x}}$) and a white sensor noise (w_{accel}) can be written as

$$a_{\ddot{x}} = \ddot{x} + c_{\ddot{x}} + b_{\ddot{x}} + w_{accel} \quad (2.7)$$

The accelerometer sensor noise w_{accel} is assumed to be normally distributed with zero mean. The bias is modeled as a first order Markov process as shown in the gyro model where the noise is also normally distributed with zero mean and the sampled covariance [4]

$$E[w_{accel}^2] = \sigma_{accel}^2 f_s \quad (2.8)$$

$$E[w_{accel_{bias}}^2] = \frac{2f_s \sigma_{accel_{bias}}^2}{\tau_{\ddot{x}}} \quad (2.9)$$

2.3 Random Walk Evaluation

Figure 2.1 is a plot of a fourteen hour static run for a KVH-5000 rate gyro. The top plot is the actual sensor output. The bottom plot is a filtered version of the sensor output. The moving bias can partially be seen in the filtered inertial sensors data. For more thorough and theoretical treatment of the filtering methodology, see reference [Demoz].

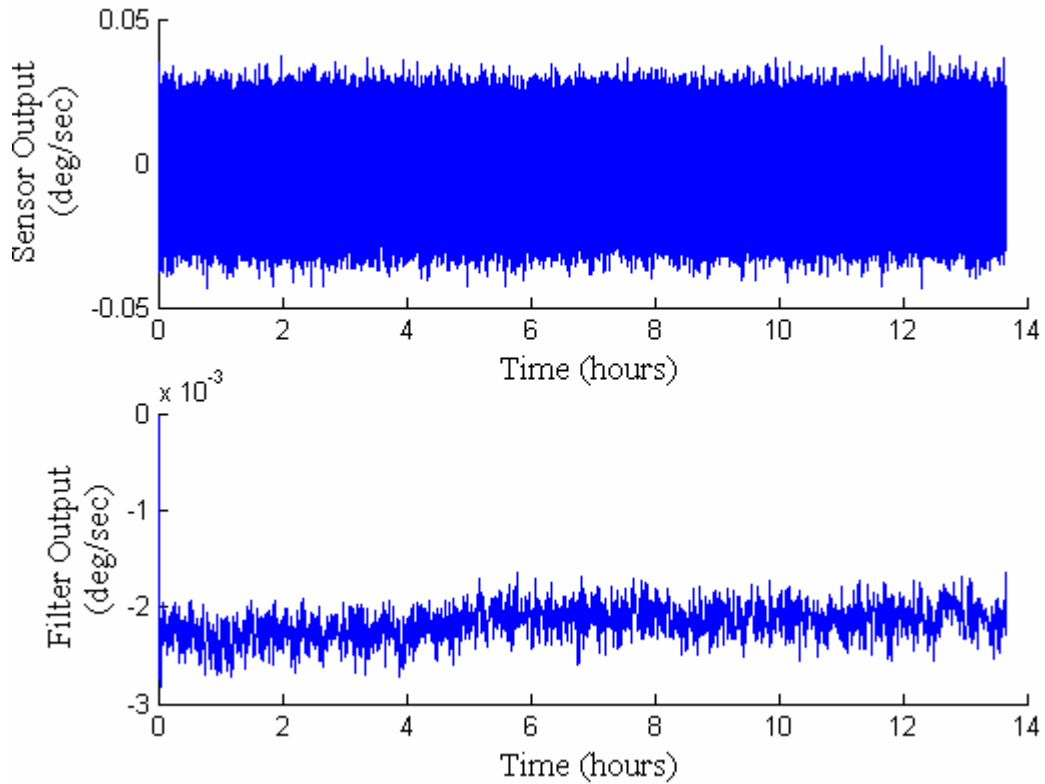


Figure 2.1 KVH-5000 Experimental data (top) and filtered experimental data (bottom)

An Allan variance chart is used to determine the statistics of the wide band noise present in a sensor. This noise is commonly referred to as the random walk of a sensor and is represented by the w in the model given in Equation (2.2) above. Allan variance charts have been used extensively to characterize noise and bias drift of inertial sensors [Allan]. Figure 2.2 shows the Allan variance of the raw unfiltered experimental data collected on the KVH-5000 rate gyroscope.

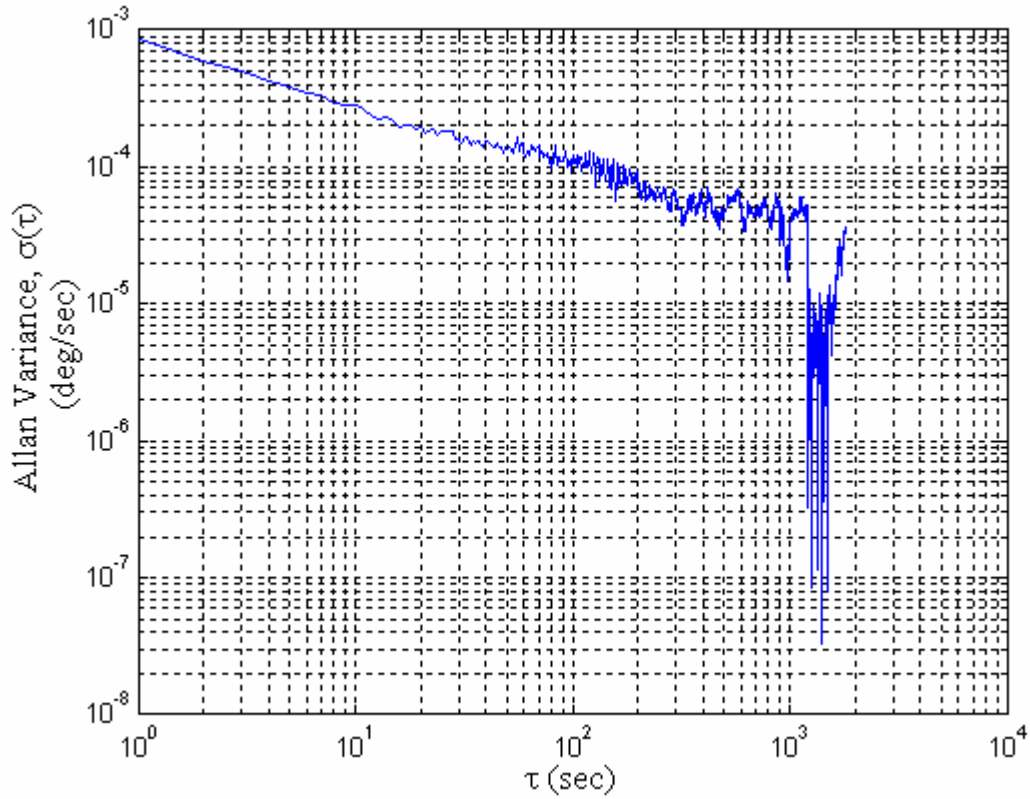


Figure 2.2.

Allan variance chart for the experimental data of the KVH-5000

The Allan variance chart provides a plot of the gyros Allan variance $\sigma(\tau_{av})$ versus the time averaging blocks τ_{av} . The angular random walk w_{gyro} can be found at the intersection of $\tau_{av} = 1$. From the Allan Variance chart in Figure 2.2, the angular random walk w_{gyro} of the KVH-5000's experimental data is found to be 8.5×10^{-4} deg/sec. The slope of the data in the chart determines the error mechanism that dominates the data. For this data the slope is near $-1/2$, which is characteristic of wide-band noise [4]. This indicates that this data is dominated by the random walk statistics, and all other error statistics are nearly negligible.

Shown in Figure 2.3 is a plot of a 3 hour static run for a Systron-Donner AQRS-104 rate gyro. The top plot is the actual sensor output while the bottom plot is a filtered version of the sensor output. Unlike the KVH-5000 static data, a moving bias can be seen in both the unfiltered data and in the filtered data.

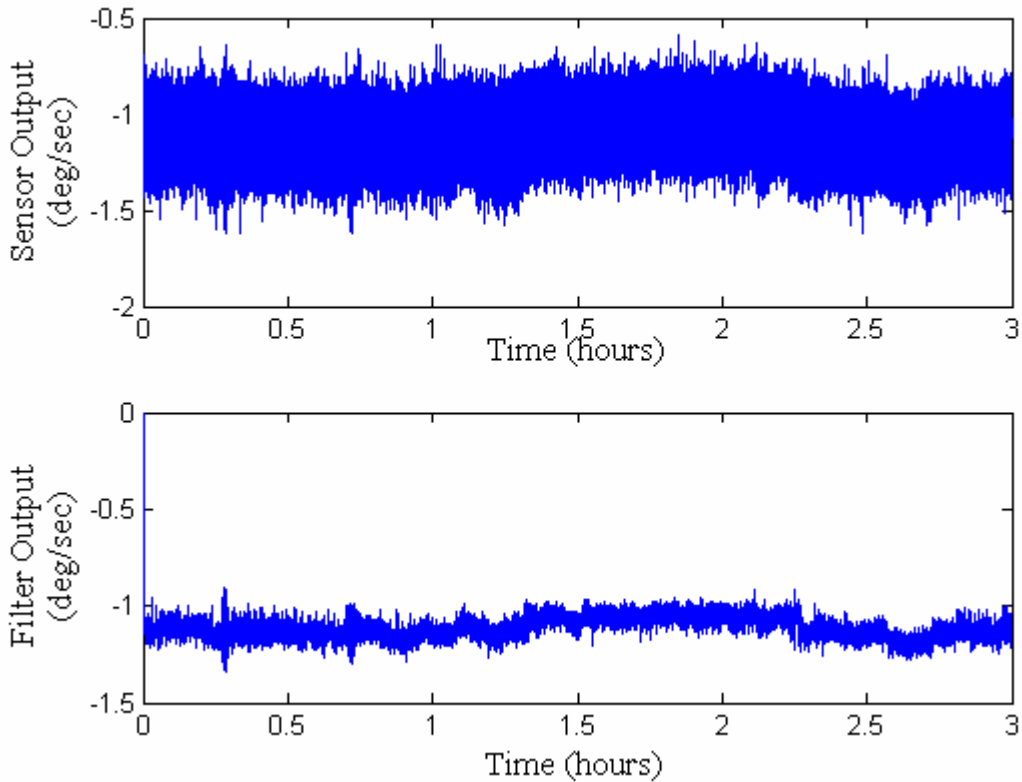


Figure 2.3 AQRS-104 Experimental Data Filtered and Unfiltered

Observe in Figure 2.4 that the angular random walk w_{gyro} for the AQRS-104 is equal to 2.1×10^{-2} deg/sec. Observe that the curve in Figure 2.4 changes slope from $-\frac{1}{2}$ to $+\frac{1}{2}$ at approximately $\tau_{av} = 10$ seconds. The initial slope of the curve is approximately

- $\frac{1}{2}$, which is characteristic of wide-band noise. The slope of the region after τ_{av} is equal to ten seconds is approximately $+\frac{1}{2}$, which is characteristic of exponentially correlated noise, or a first order Markov Process.

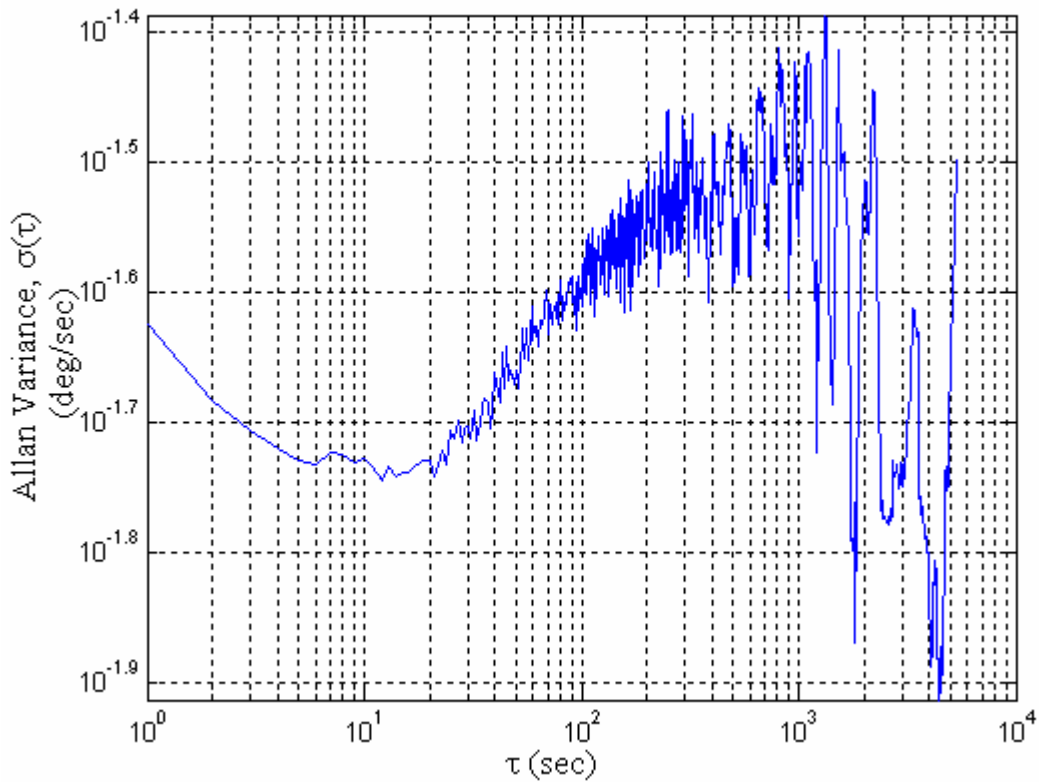


Figure 2.4

Allan Variance Chart for the Unfiltered Experimental Data of the AQRs-104

2.4 Walking Bias Evaluation

From the Allan Variance chart in Figure 2.4, it is clear that the effect of the exponentially correlated noise begins to dominate other sensor errors after a time constant of 10 seconds. This information is good, but in order to model the sensor accurately the time constant of the gyros walking bias (b_r) must be evaluated with much more precision. This is done with an autocorrelation function. Appendix D contains a detailed description of the autocorrelation function. Figure 2.5 shows the autocorrelation function of the AQRS-104 filtered experimental data. Since the gyros walking bias (b_r) is modeled as a first order Markov process, the time constant (τ_r) of the process can be determined by picking the value of the autocorrelation function after it decays to a point 36.8% of its point of origin, which is the defining point for a first order differential equations time constant. For this sensor, τ_r has a value of 1171 seconds.

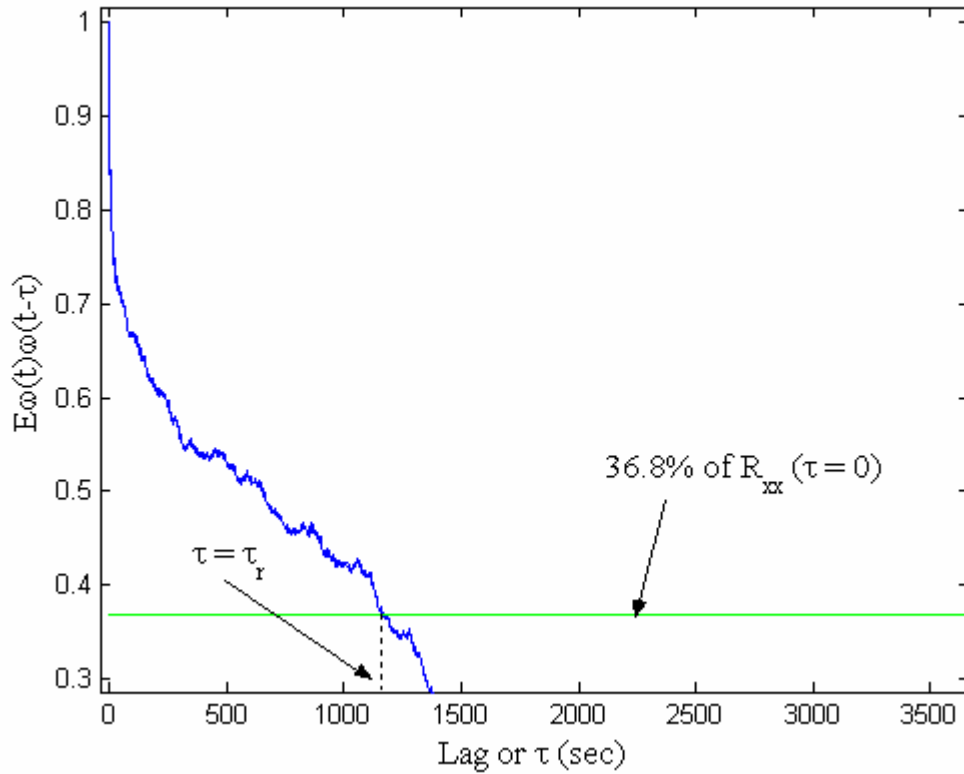


Figure 2.5 AQRs-104 Experimental Autocorrelation Plot

In order to model the gyro's walking bias (b_r) as a Markov process, the variance of the input noise ($w_{gyro\,bias}$) must be known as well as the time constant (τ_r). This is obtained by using the filtered experimental data and calculating its standard deviation. This standard deviation is considered to be $\sigma_{gyro\,bias}$. Calculate the variance of $w_{gyro\,bias}$ by using the following equation.

$$E[w_{gyro\,bias}^2] = \frac{2f_s \sigma_{gyro\,bias}^2}{\tau_r} \quad (2.10)$$

2.5 Constant Bias Evaluation

The constant offset bias of a sensor is simply the mean of the sensor output. It is important that the data used to calculate the constant offset bias be of a sufficient length to ensure that the actual sensor measurement has reached a steady state output. When the sensor has reached a steady state output, the calculated mean will be consistent with a constant offset bias of the actual sensor measurement. This may be observed in the Systron-Donner and KVH rate gyro measurements in Figures 2.1 and 2.3.

2.6 Rate Gyro Model Validation

Figure 2.6 is a comparison of the Allan Variance Charts for simulated data of a KVH-5000 rate gyro and the experimental data shown previously in Figure 2.2. The simulated data was created by using the simple sensor model presented in Equation (2.1). The initial numerical values used for the model error sources are found in the manufactures specification sheet [Bennett]. It is possible to obtain all of the values needed to model the sensor from the manufactures specification sheet because the sensor is dominated by wide-band noise.

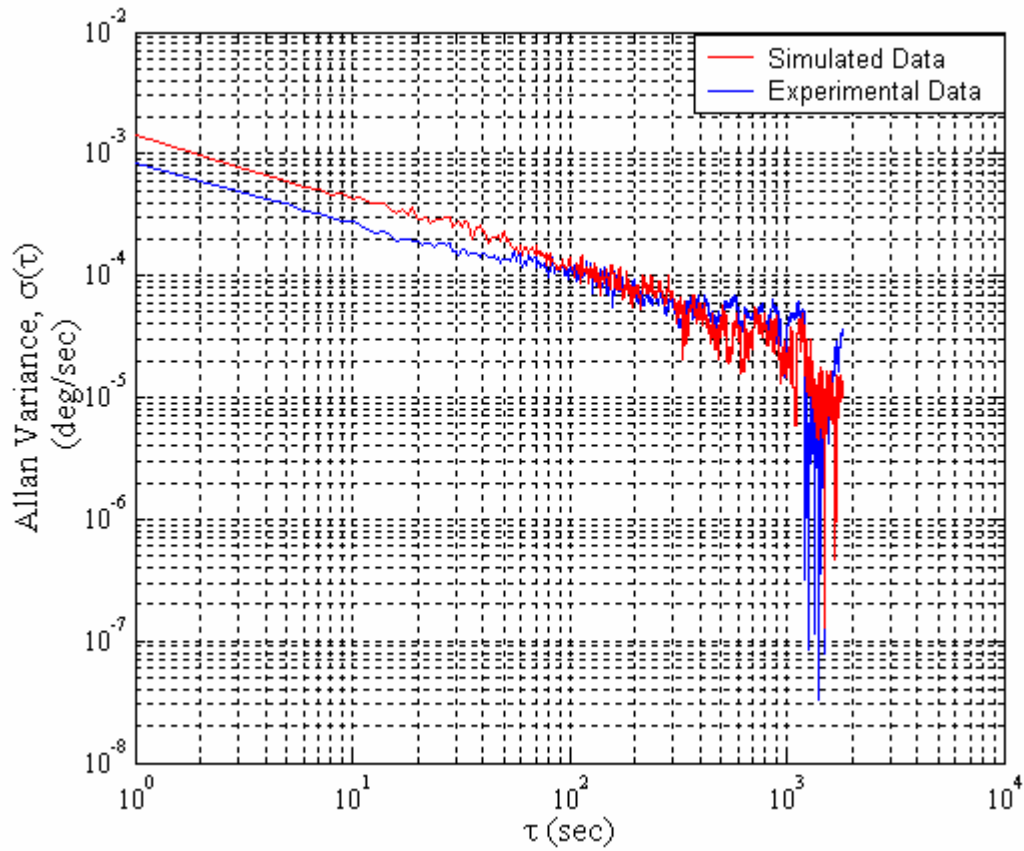


Figure 2.6

Allan Variance Comparison I of the KVH 5000 Experimental and Simulated Data

A comparison of experimental data to simulated data is given in Figure 2.6. Observe that the angular random walk for the experimental data and simulated data do not match. The angular random walk of the simulated data is 1.3×10^{-3} deg/sec and the angular random walk of the experimental data is 8.5×10^{-4} deg/sec. Figure 2.7 is a comparison of the Allan Variance charts after the angular random walk of the simulated data was set to the value of the experimental data.

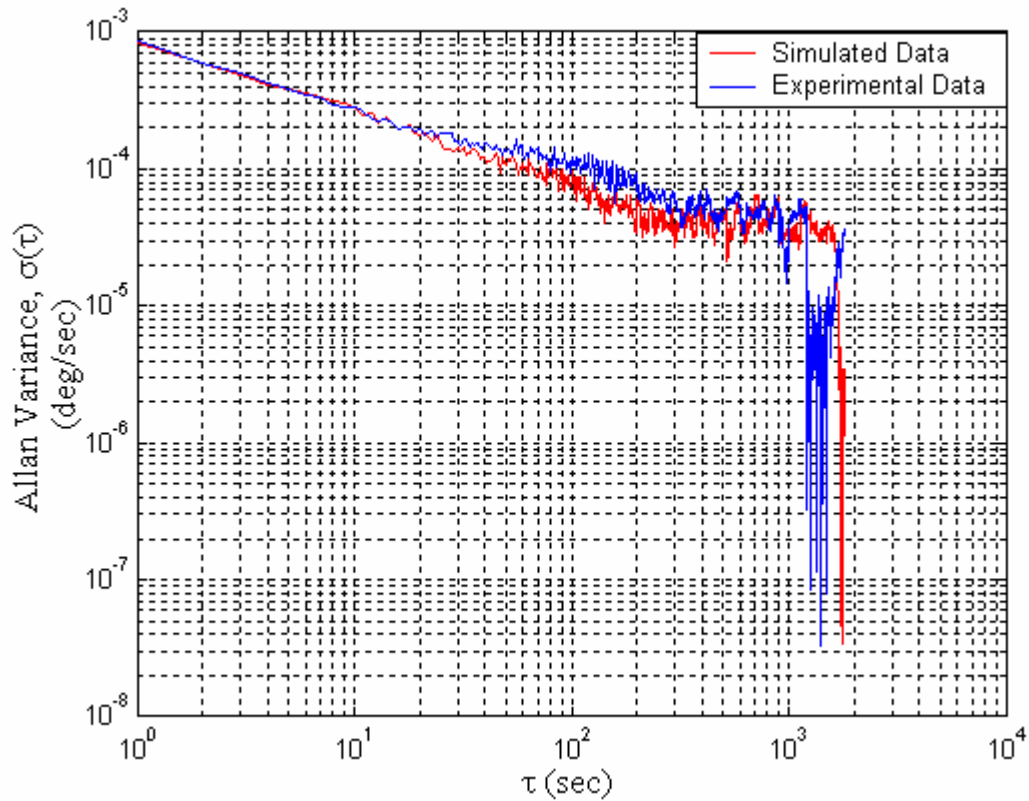


Figure 2.7

Allan Variance Comparison II of the KVH 5000 Experimental and Simulated Data

In Figure 2.8 a comparison of the Systron-Donner AQRS-104 Allan Variance Charts is shown. The experimental data used is the same as presented in Figure 2.4, and simulated data was produced by using the sensor model presented in Equation (2.1). The angular random walk and bias drift statistics for the model errors were found in the manufactures specification sheet [BEI]. The time constant of the Markov Process was found in previous work [Demoz]. The published angular random walk and bias drift for this sensor are 0.025 deg/sec and 0.05 deg/sec, respectively. The angular random walk

and bias drift of the experimental data are 0.02373 deg/sec and 0.054 deg/sec, respectively.

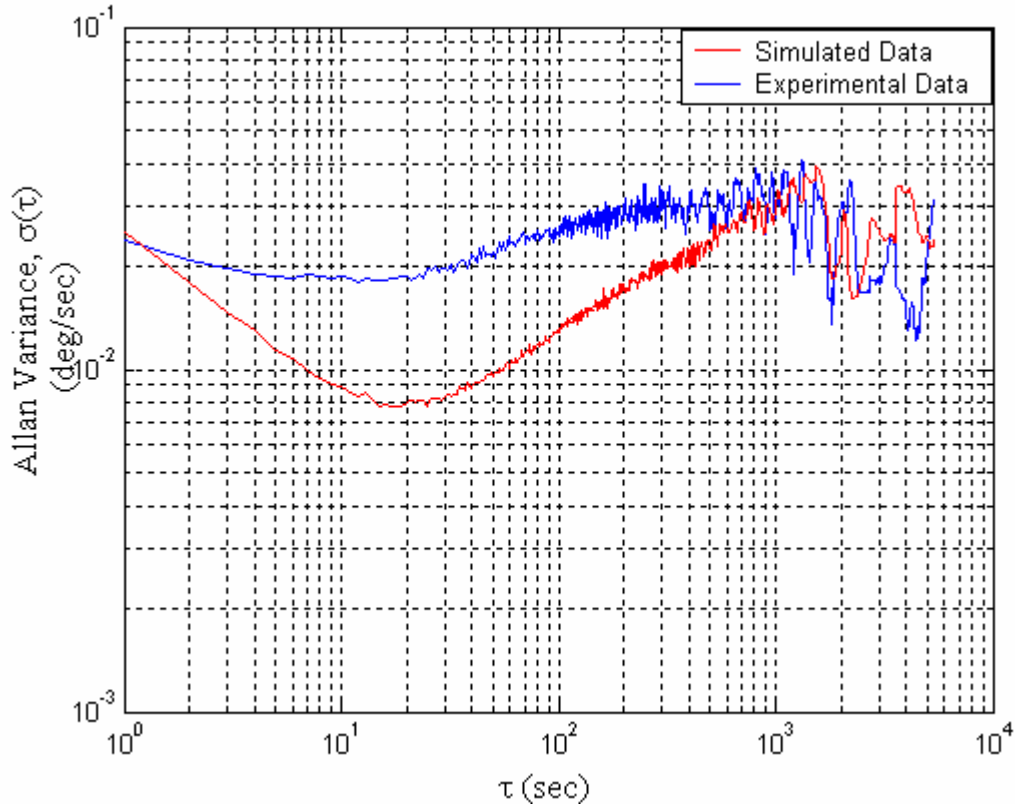


Figure 2.8

Allan Variance Comparison of the AQRS-104 Experimental and Simulated Data

The time constant of the sensor is published to be 1000 seconds. Figure 2.9 is a comparison of a decaying exponential curve with a time constant of 1000 seconds and the autocorrelation of the experimental data. The experimental data decays reasonable close to the exponential curve envelope. The actual time constant of the experimental data is 1171 seconds. The discrepancies in the slopes of the Allan variances are due to the fact

that the experimental data contains many more error sources that contribute to the sensors output. Recall that the simple model provided in this chapter only accounts for two error sources, wide-band noise and exponential correlated noise modeled as a 1st Order Markov Process. Therefore, the possibility of exact slope alignment is rare. However, the fact that the angular random walk values, the bias drift, and bias time constants values are very close provides some level of confidence that the simulated data is characteristic of the experimental data.

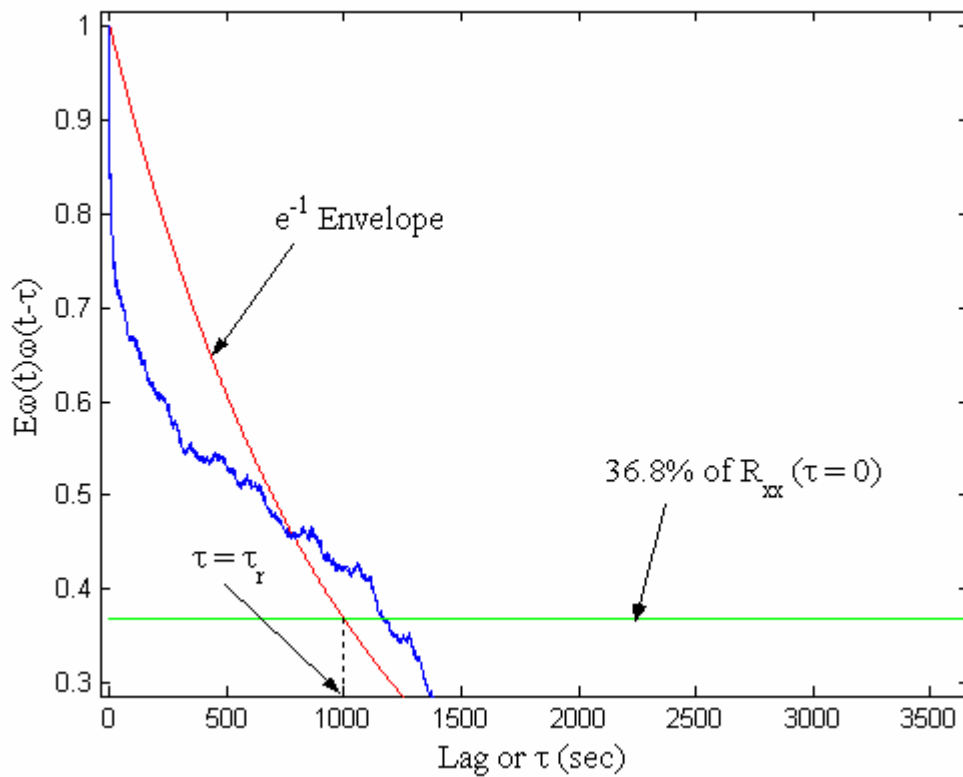


Figure 2.9

AQRS-104 Autocorrelation Comparison of the Filtered Experimental Data

2.7 Accelerometer Model Validation

The same type of data and algorithms used to validate the rate gyros can be used to validate the accelerometer model. Figure 2.10 is static data from a Humphrey accelerometer. The top plot is raw unfiltered data. The bottom plot is the same data filtered through a Butterworth filter.

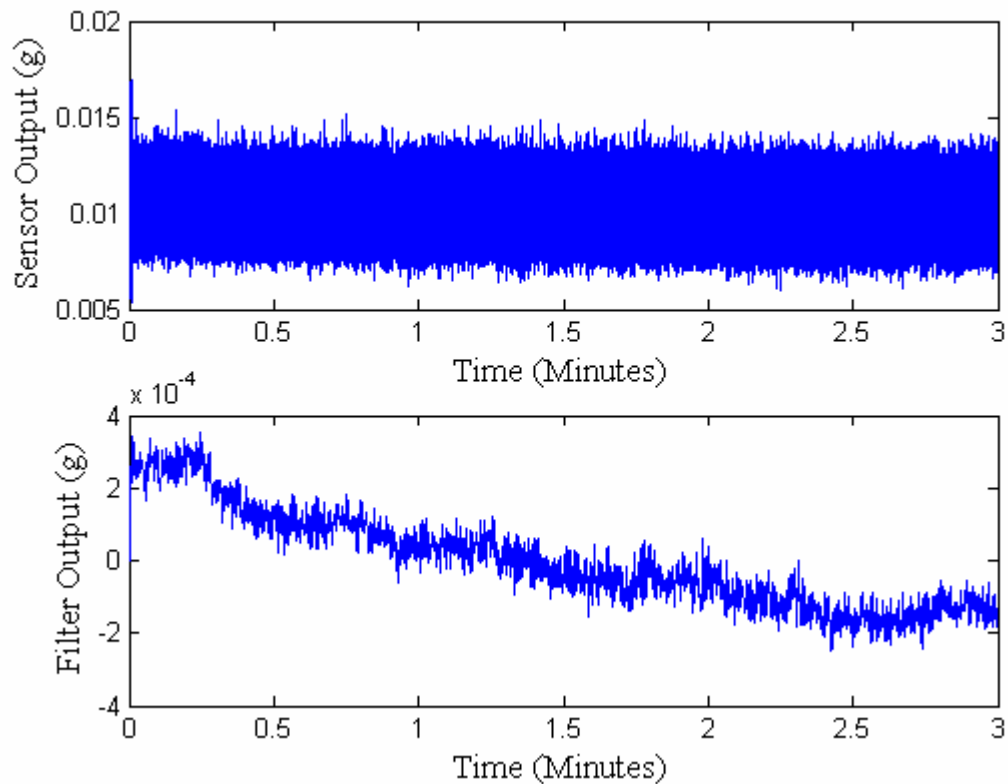


Figure 2.10 Humphrey Accelerometer Actual Data filtered and Unfiltered Data

In Figure 2.11 the autocorrelation plot of the filtered data is shown. From the autocorrelation, the time constant of the moving bias can be estimated to be 700 seconds.

The standard deviation of the moving bias is estimated to be 8.5×10^{-5} g's. Using an Allan variance chart, the wide-band noise is estimated to be $9.5 \times 10^{-6} \text{ g's} / \sqrt{\text{Hz}}$. Figure 2.12 is a comparison of the Allan variance charts using the experimental and simulated data. The simulated data was produced by using the estimated values for the time constant, bias standard deviation and random walk. From the figure, it is clear that the wide-band noise is modeled correctly for a period of time. Unfortunately, the point at which the exponentially correlated errors become dominate is not as defined in the simulated data as it is in the experimental data. This validation is similar to that of the rate gyro model. Even with the discrepancies, the analytical model's accuracy is sufficient enough to describe the dominate errors seen in the actual data.

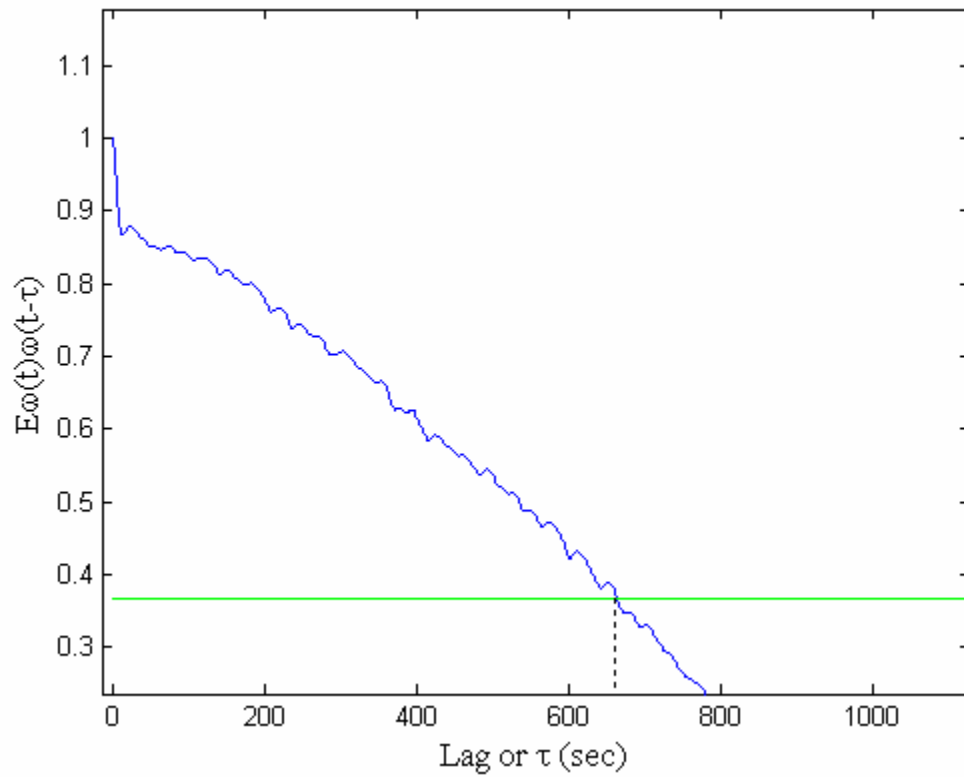


Figure 2.11

Humphrey Accelerometer Autocorrelation of the Filtered Experimental Data

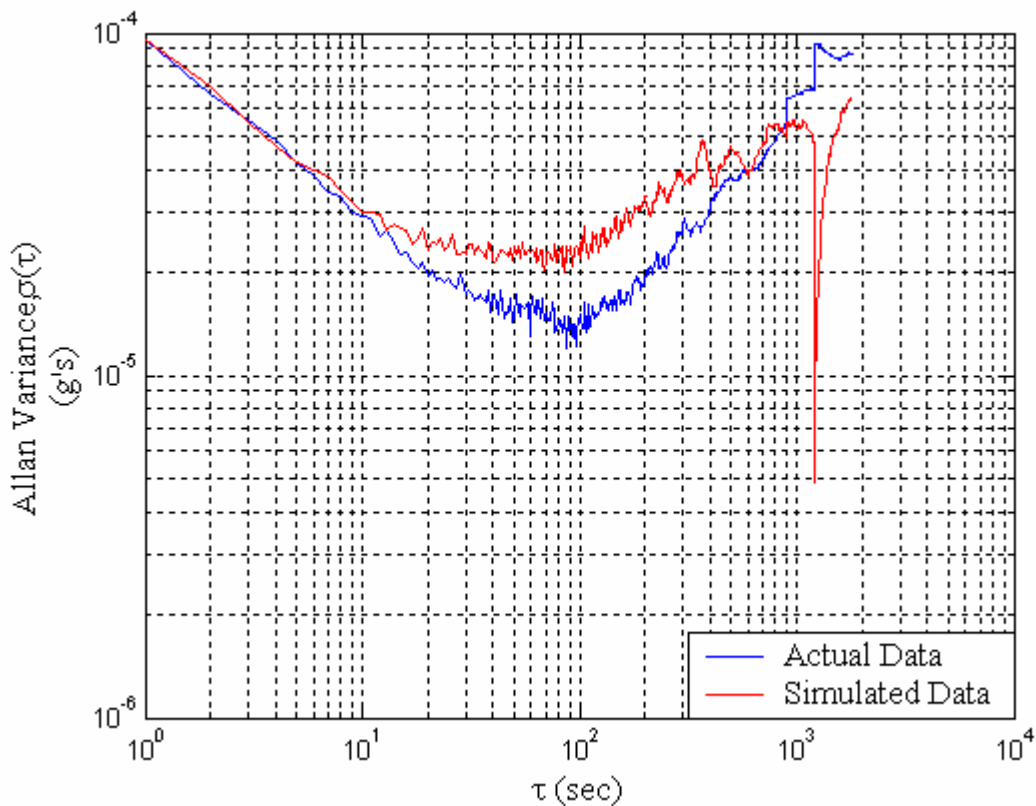


Figure 2.12

Allan Variance Comparison of the Humphrey Accelerometer Experimental and Simulated Data

2.8 Sensor Categorization

Table 2.1 lists three sample accelerometers and their respective sensor model characteristic values. Table 2.3 lists seven sample rate gyros and their respective sensor model characteristic values. The various sensor characteristics were grouped into three categories [Demoz]: consumer, automotive and tactical grade. Table 2.2 and Table 2.4 show the characteristic values for each grade. Representative values from the actual

sensors in Table 2.I and Table 2.III can be compared to the values in Table 2.II and Table 2.IV to categorize a specific sensor.

Table 2.1 Accelerometer Characteristics Used for this Analysis

Accelerometer	Attribute	Units	Specification
LN-200 IMU	White noise	Micro g/ $\sqrt{\text{Hz}}$	50
	Scale Factor Stability	ppm	300
	Bias Variation	micro-g	50
	Rate	$\pm\text{g}$	40
HG-1700 IMU	Random walk	Micro-g/ $\sqrt{\text{Hz}}$	30
	Scale Factor Stability	ppm	300
	Bias Variation	Micro-g	50.00
	Rate	$\pm\text{g}$	50
HG-1900 IMU	Random walk	Micro-g/ $\sqrt{\text{Hz}}$	30
	Scale Factor Stability	ppm	300
	Bias Variation	Micro-g	1
	Rate	$\pm\text{g}$	70

Table 2.2 Classification Characteristics Used to Categorize Accelerometers

Accelerometer	Attribute	Units	Specification
Consumer	Random Walk	$g/\sqrt{\text{Hz}}$.003
	Bias Time Constant	sec	100
	Bias Variation	g	2.4×10^{-3}
Automotive	Random Walk	$g/\sqrt{\text{Hz}}$.001
	Bias Time Constant	sec	100
	Bias Variation	g	1.2×10^{-3}
Tactical	Random walk	$g/\sqrt{\text{Hz}}$.0005
	Bias Time Constant	sec	60
	Bias Variation	g	50×10^{-5}

Table 2.3 Gyro Characteristics Used for this Analysis

Gyro	Attribute	Units	Specification
LN-200 IMU	Random walk	$^{\circ}/\sqrt{\text{hr}}$	0.04 - 0.10
	Scale Factor Stability	ppm	100
	Bias Variation	$^{\circ}/\text{hr}$	0.35
	Rate	\pm°/sec	1000
HR-1700 IMU	Random walk	$^{\circ}/\sqrt{\text{hr}}$	0.125 - 0.300
	Scale Factor Stability	ppm	150
	Bias Variation	$^{\circ}/\text{hr}$	2.00
	Rate	\pm°/sec	1000
HG-1900 IMU	Random walk	$^{\circ}/\sqrt{\text{hr}}$	0.1
	Scale Factor Stability	ppm	150
	Bias Variation	$^{\circ}/\text{hr}$	0.3 - 10.0
	Rate	\pm°/sec	1000
KVH-5000	Random walk	$^{\circ}/\sqrt{\text{hr}}$	0.083
	Scale Factor Stability ($\pm 200^{\circ}/\text{sec}$)	ppm	500

Autogyro Navigator	Scale Factor Stability		
	(±500°/sec)	ppm	1000
	Bias Variation	°/hr	1.00
	Rate	±°/sec	500
Systron-Donner	Random walk	°/√hr	0.33
	Scale Factor Stability	% rms	0.5
	Bias Variation	°/hr	90.00
	Rate	°/sec	100
AQRS-000640-104	Random walk	°/sec/√Hz	≤0.025
	Scale Factor Stability	±%	3
	Bias Variation	°/hr	≤180.00
	Rate	±°/sec	64
AQRS-000640-109	Random walk	°/sec/√Hz	≤0.025
	Scale Factor Stability	±%	5
	Bias Variation	°/hr	≤180.00
	Rate	±°/sec	75

Table 2.4 Classification Characteristics Used to Categorize Rate Gyros

Rate Gyro	Attribute	Units	Specification
Consumer	Random walk	$^{\circ}/\text{sec}/\sqrt{\text{Hz}}$.05
	Bias Time Constant	sec	300
	Bias Variation	$^{\circ}/\text{hr}$	360
Automotive	Random walk	$^{\circ}/\text{sec}/\sqrt{\text{Hz}}$.05
	Bias Time Constant	sec	300
	Bias Variation	$^{\circ}/\text{hr}$	180
Tactical	Random walk	$^{\circ}/\text{sec}/\sqrt{\text{Hz}}$.0017
	Bias Time Constant	sec	100
	Bias Variation	$^{\circ}/\text{hr}$	0.35

2.9 Summary and Conclusions

In this chapter, a simple sensor model was laid out that incorporated a moving bias term, a constant bias term, and a random error term. The biases and random error sources were analyzed statistically. The numerical values for the time constants, means, and variances were obtained by using common statistical methods, Allan Variance charts, Autocorrelation functions, and Monte Carlo Simulations. The statistical parameters of the error sources were used to categorize and characterize the sensors. The Inertial sensors were categorized into four basic grades: navigational, tactical, automotive, and consumer. Several sensor grades were simulated and experimentally validated. The simulated sensors will be used in later chapters to determine resulting levels of performance that can be achieved when combined with GPS. A group of tables was provided which contained the specification for a number of commonly used rate gyros and accelerometers. Additional tables were provided which are used to classify the sensors.

CHAPTER 3

INTEGRATION ERRORS IN A TWO DEGREE OF FREEDOM INERTIAL MEASUREMENT UNIT

3.1 Introduction

In this chapter the errors associated with the numerical integration of a single rate gyro and single accelerometers, to calculate position, velocity and heading in a planar setting, are presented. The error growth of the position, velocity, and heading calculation are depicted with the use of a Monte Carlo Simulation. Both consumer and tactical grade sensor characteristics are compared and experimental data is used to validate the bounds of the Monte Carlo simulations. The Monte Carlo simulations are validated by showing the error growths of rate gyros and accelerometers, which contain moving biases, and comparing these error growths to simulations where the only error source is wide-band noise. Analytical equations for position, velocity and heading errors are derived that plot the error growths depicted by the integration of rate gyros and accelerometers, which contain only one error source, wide-band noise. Finally the effects a gravity field as on the error growths of the position, velocity and heading calculations are shown. The errors resulting from the gravity field are shown by a comparison. The comparison contains the error growths when there is a gravity field in the system and the error growths when there is not a gravity field in the system.

3.2 IMU Integration Errors

The heading of the platform must first be calculated in order to determine the position of a 2 DOF IMU. This is accomplished by numerically integrating the gyroscope yaw rate measurement. The method chosen to do this is the Runge-Kutta Method [Burden]. This method's procedure is laid out below in the state space format. The following equations are the state space matrices used to calculate platform heading.

$$A = [0] \quad B = [1] \quad (3.1)$$

$$f_{heading} = A[\psi] + B[\dot{\psi}] \quad (3.2)$$

A Runge-Kutta order four integration routine is used to propagate the heading state ψ forward to the next time step. The routine is as follows

$$\begin{aligned} \psi_0 &= 0 \\ k_1 &= T_s f_{heading}(\psi_i, \dot{\psi}_i) \\ k_2 &= T_s f_{heading}(\psi_i + k_1/2, \dot{\psi}_i) \\ k_3 &= T_s f_{heading}(\psi_i + k_2/2, \dot{\psi}_i) \\ k_4 &= T_s f_{heading}(\psi_i + k_3, \dot{\psi}_i) \\ \psi_{i+1} &= \psi_i + (k_1 + 2k_2 + 2k_3 + k_4)/6 \end{aligned} \quad (3.3)$$

A yaw angle (ψ) of zero corresponds to due north. Therefore any positive angle change is a rotation in the eastwardly direction. Likewise any negative angle change is a rotation in the westward direction.

After the yaw angle of the platform is calculated, the position and velocity of the platform must be calculated by integrating the accelerometer measurements. The Runge-Kutta method was also used for this calculation. The state space matrices required to calculate position and velocity are given below.

$$A = \begin{bmatrix} 0 & 0 & 1 & 0 \\ 0 & 0 & 0 & 1 \\ 0 & 0 & 0 & 0 \\ 0 & 0 & 0 & 0 \end{bmatrix} \quad B = \begin{bmatrix} 0 \\ 0 \\ \cos(\psi) \\ \sin(\psi) \end{bmatrix} \quad (3.4)$$

$$f_{positon} = A[states] + B[\ddot{x}] \quad (3.5)$$

$$states = \begin{bmatrix} x \\ y \\ \dot{x} \\ \dot{y} \end{bmatrix} \quad (3.6)$$

Again, a Runge-Kutta order four integration routine shown below is used to propagate the position and velocity states forward.

$$\begin{aligned} states_0 &= 0 \\ k_1 &= T_s f_{positon}(states_i, \psi_i, \ddot{x}_i) \\ k_2 &= T_s f_{positon}(states_i + k_1/2, \psi_i, \ddot{x}_i) \\ k_3 &= T_s f_{positon}(states_i + k_2/2, \psi_i, \ddot{x}_i) \\ k_4 &= T_s f_{positon}(states_i + k_3, \psi_i, \ddot{x}_i) \\ states_{i+1} &= states_i + (k_1 + 2k_2 + 2k_3 + k_4)/6 \end{aligned} \quad (3.7)$$

The initialization of the states vector to zero is convenient for this analysis. However, if this were done in practice, the initial longitude and latitude of the vehicle platform would need to be recorded. With the initial longitude and latitude recorded, it would be possible to convert the position calculations into longitude and latitude

Figures 3.1-3.6 are results from a Monte Carlo simulation when the above integration is performed with the constant bias removed from the static sensor's measurements. The results for a tactical grade IMU are presented in Figures 3.1-3.3. The results for a consumer grade IMU are presented in Figures 3.4-3.6

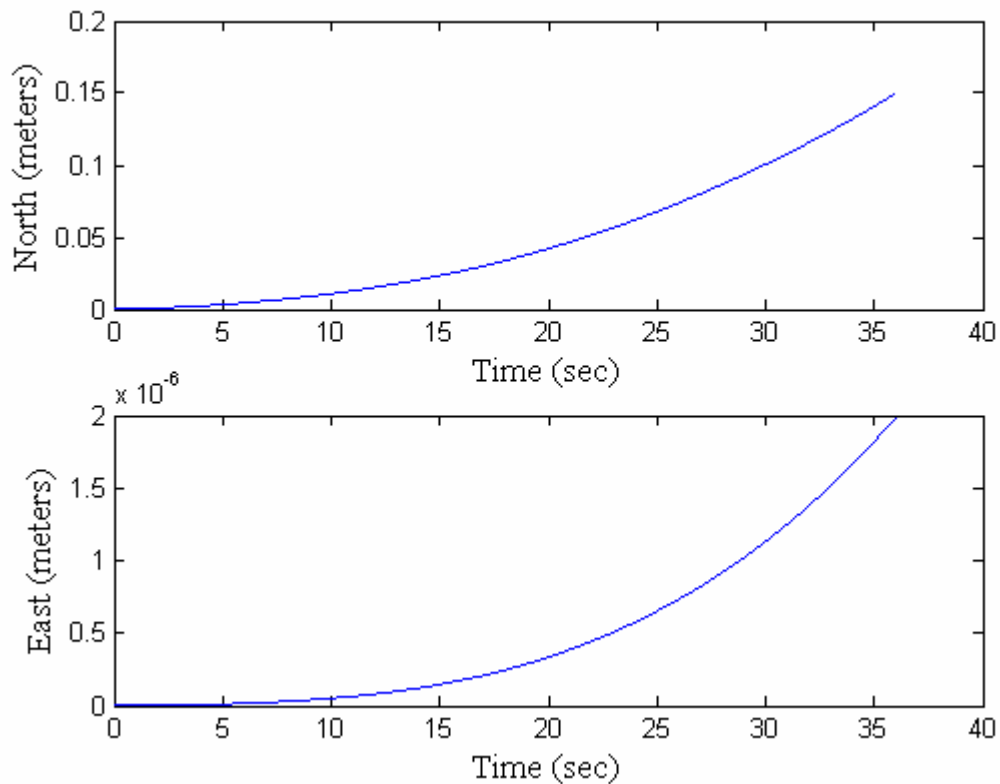


Figure 3.1 Tactical Grade IMU Position Error Bounds (Static)

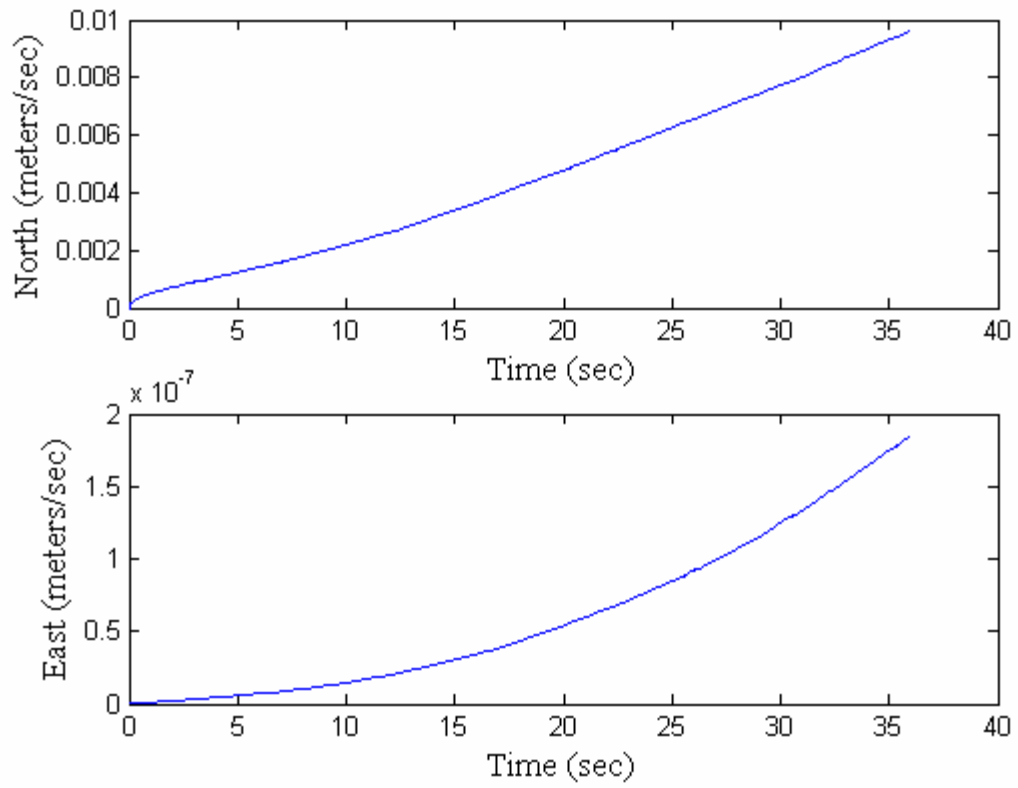


Figure 3.2 Tactical Grade IMU Velocity Error Bounds (Static)

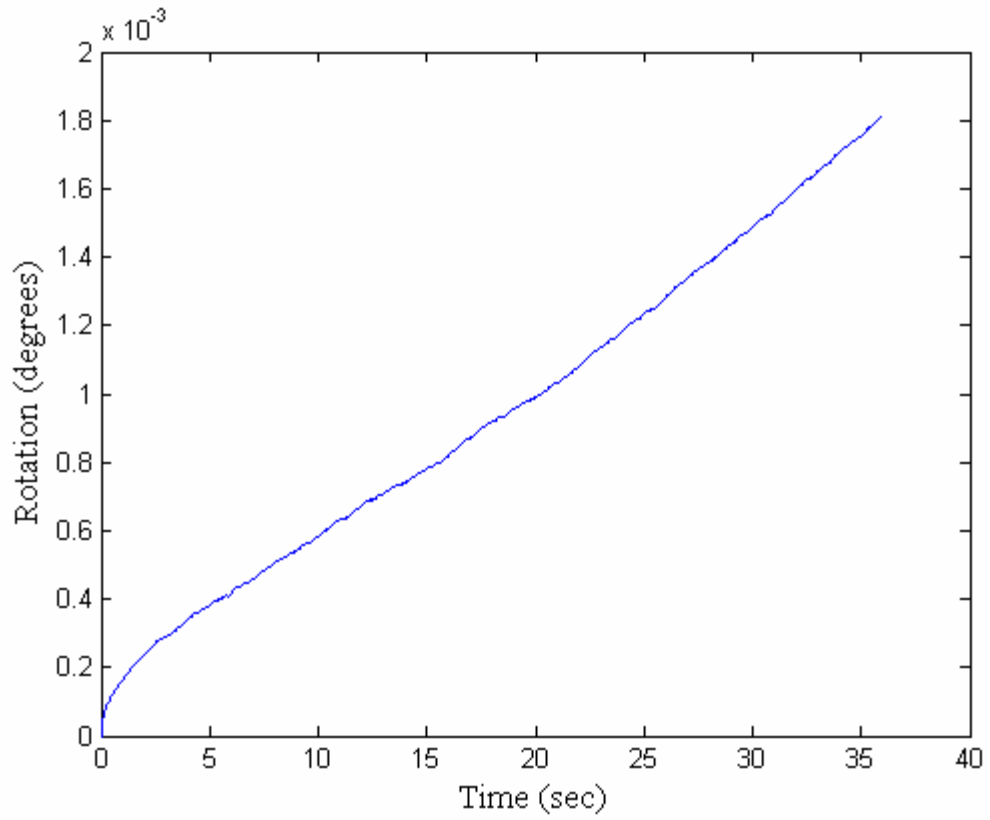


Figure 3.3 Tactical Grade IMU Yaw Angle Error Bounds (Static)

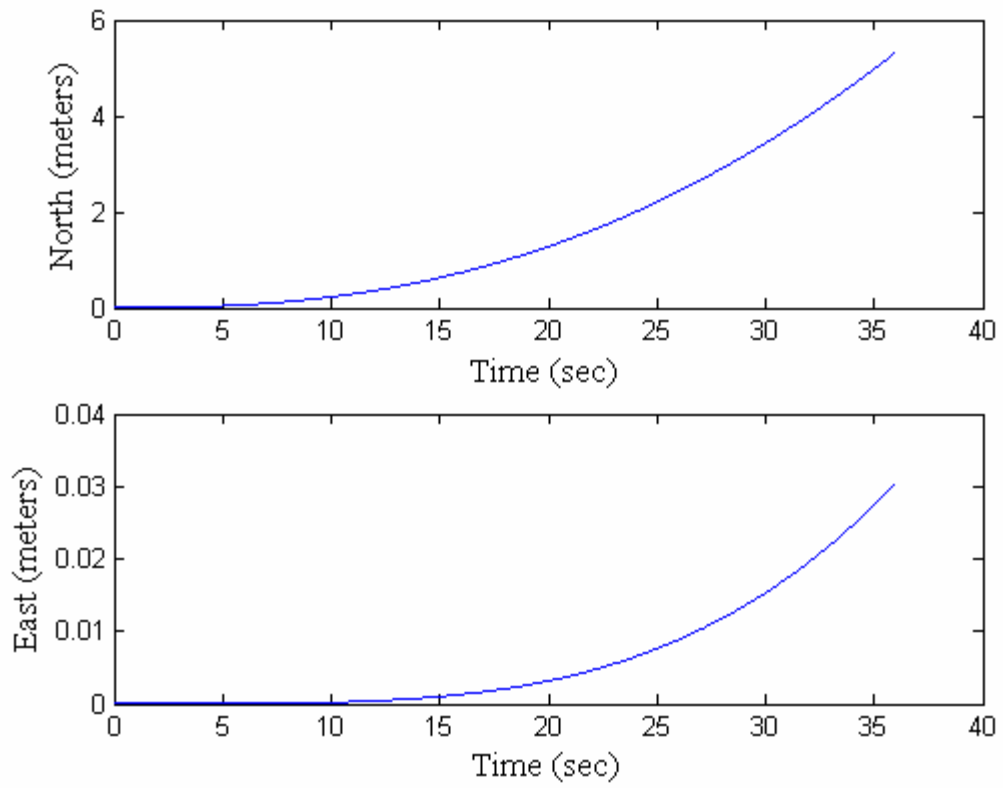


Figure 3.4 Consumer Grade IMU Position Error Bounds (Static)

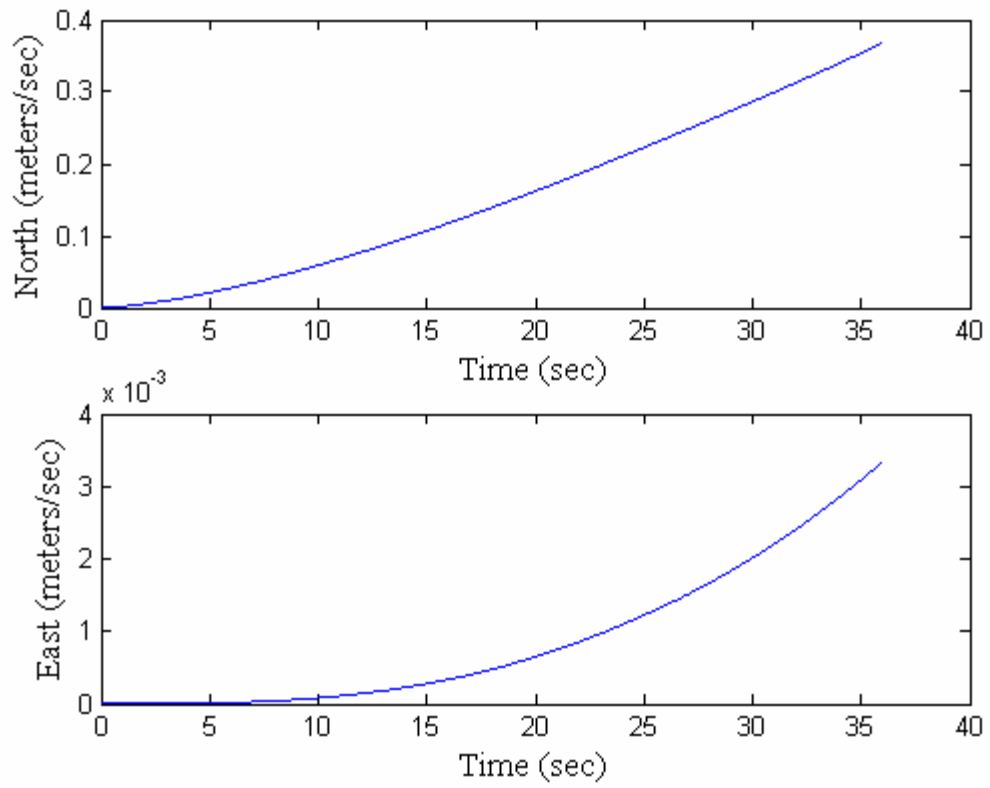


Figure 3.5 Consumer Grade IMU Velocity Error Bounds (Static)

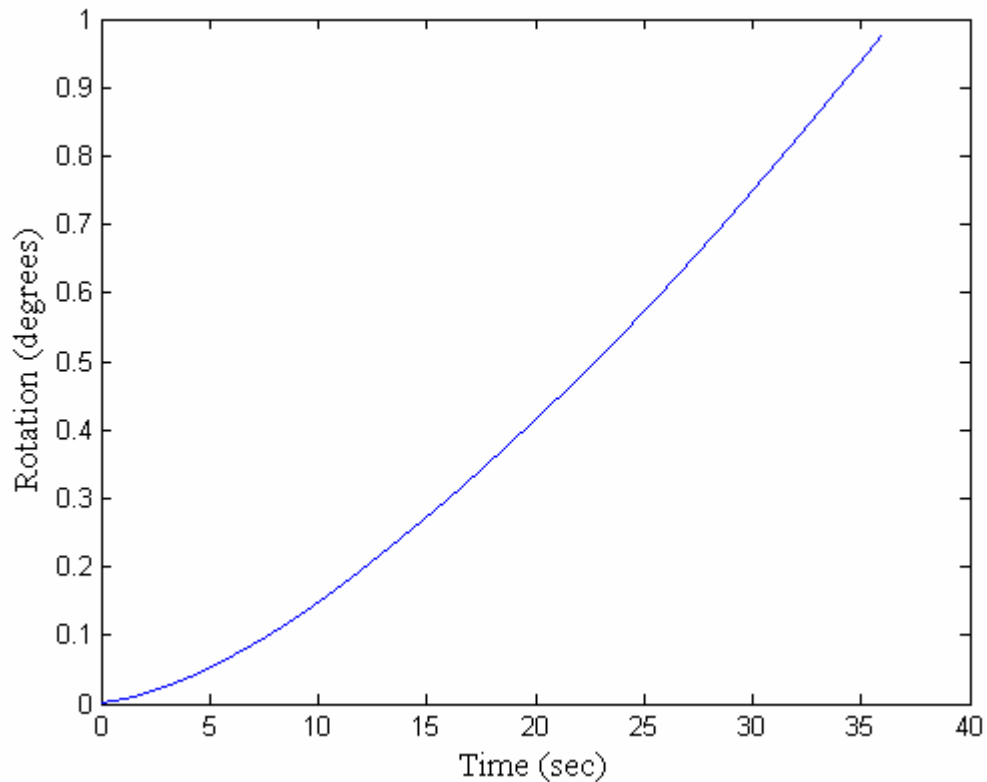


Figure 3.6 Consumer Grade IMU Yaw Angle Error Bounds (Static)

From the figures it is clear that the errors on the calculated position, velocity, and yaw angle do not stay constant. In fact, they appear to grow at an exponential rate. When a consumer grade IMU is used to calculate the north position, the error after a twenty second period has a standard deviation of nearly one meter. An additional ten seconds brings the position calculation standard deviation to nearly four meters. A tactical grade IMU has similar error characteristics; however, the error is much lower in magnitude. After a 20 second period, the standard deviation in the north position calculation is close to 0.05 meters. An additional ten seconds brings the standard deviation to 0.10 meters. The difference in the errors between the tactical and consumer

grade IMU's is significant. There is a 1900% improvement in the northerly position calculation when a tactical grade IMU is used. Although this improvement is great, it is accompanied by significant increase in price. A tactical grade IMU costs in the neighborhood of \$20K where the consumer grade IMU costs less than \$1000.

3.3 Monte Carlo Validation

In this section the Monte Carlo simulations used in the previous section are validated by showing the error growths of rate gyros and accelerometers which contain moving biases and comparing them to Monte Carlo simulations where the only error source is wide-band noise. Figure 3.7 is a plot of the error bounds for the calculated yaw angle of a KVH-5000 rate gyro. Two error bounds are presented, one is derived from the Chapter 2 sensor model with a Monte Carlo simulation, and the other is derived from the equation below. The equation below is the analytical solution for the standard deviation of integrated wide band noise. A full derivation of the below equation can be found in reference [Bevly].

$$\sigma = \sigma_w T_s \sqrt{k} \quad (3.8)$$

$$w \sim N[0, \sigma_w] \quad (3.9)$$

The KVH was chosen for this comparison because it is dominated by wide-band noise. Therefore the results from a Monte Carlo simulations produced from its specifications should match the results from the analytical solution reasonably well. It is clear from Figure 3.7 that after a period of time the error bounds of the Monte Carlo simulation begin to grow faster than the error bounds of the analytical equation. This is caused by the moving bias modeled in the sensor model.

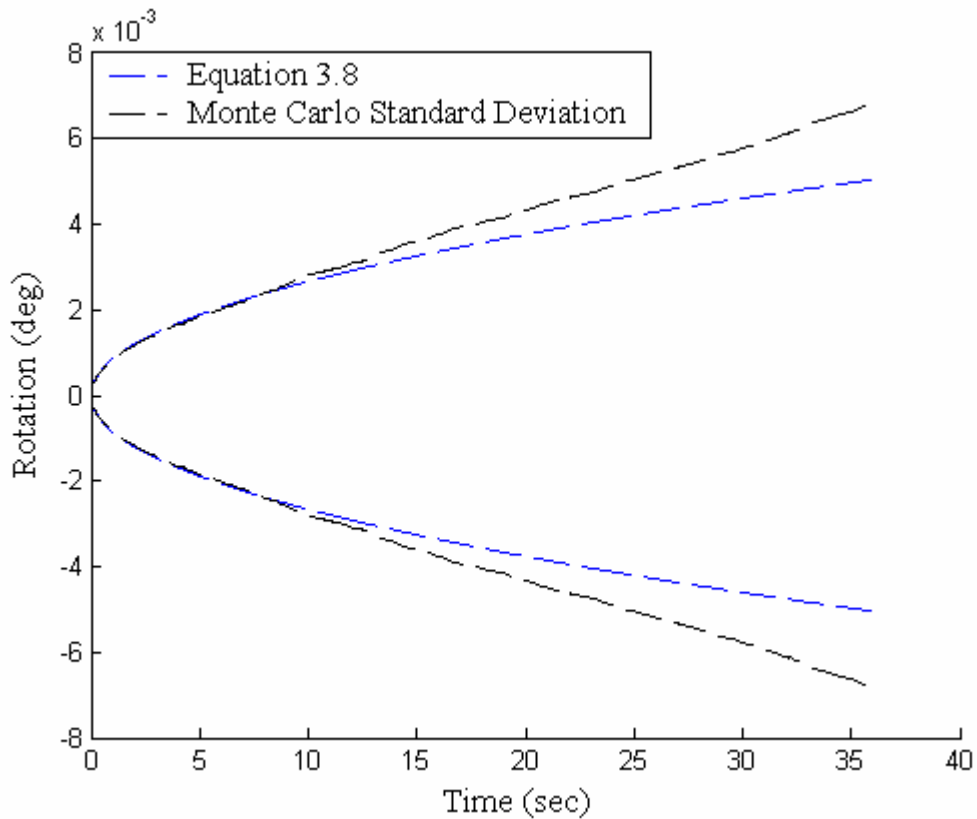


Figure 3.7 KVH Error Bound Comparison I

Figure 3.8 is also a comparison of the error bounds; however, now the moving bias has been removed from the sensor model. From the comparison, it is clear that the

Monte Carlo results match Equation (3.8). Because of this, it is reasonable to assume that the bounds derived from the Monte Carlo simulation with all errors present are valid. To help further this validation, the data from the KVH-5000 rate gyro presented in Chapter 2 will be used as well as data produced by the sensor model. Figure 3.9 is the calculated heading from that experimental data presented in Figure 2.1 and simulated data produced using the simple sensor model. As seen in Figure 3.9, both data sets fall well within the bounds resulting from the Monte Carlo simulations.

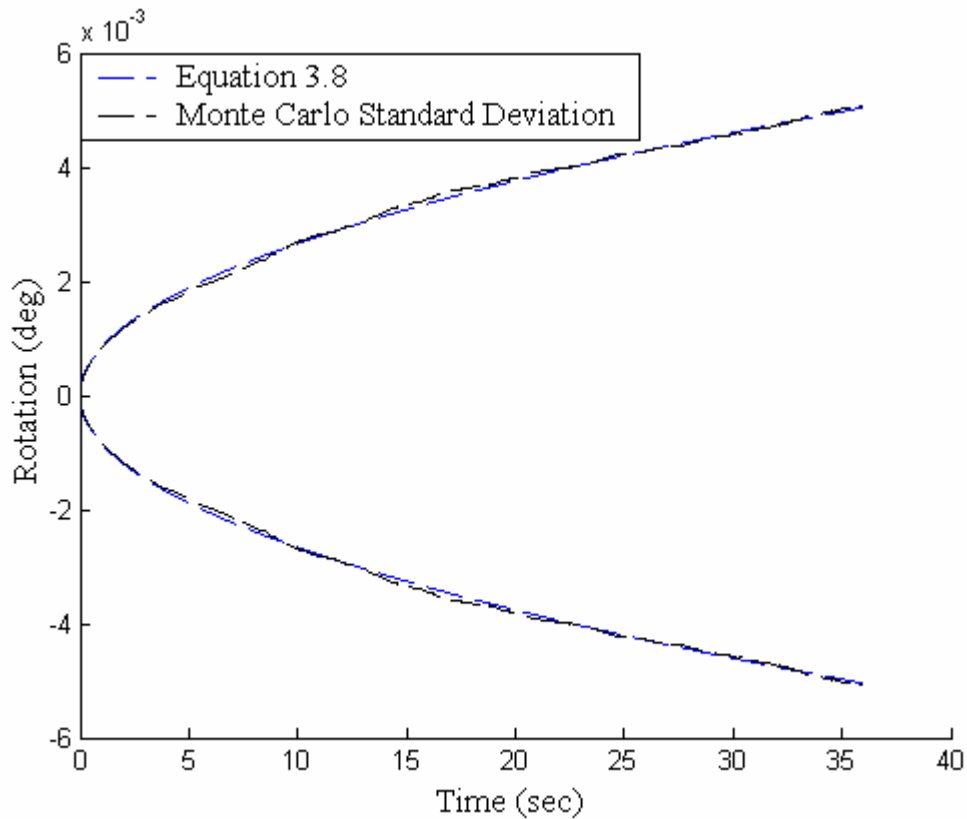


Figure 3.8 KVH Error Bound Comparison II

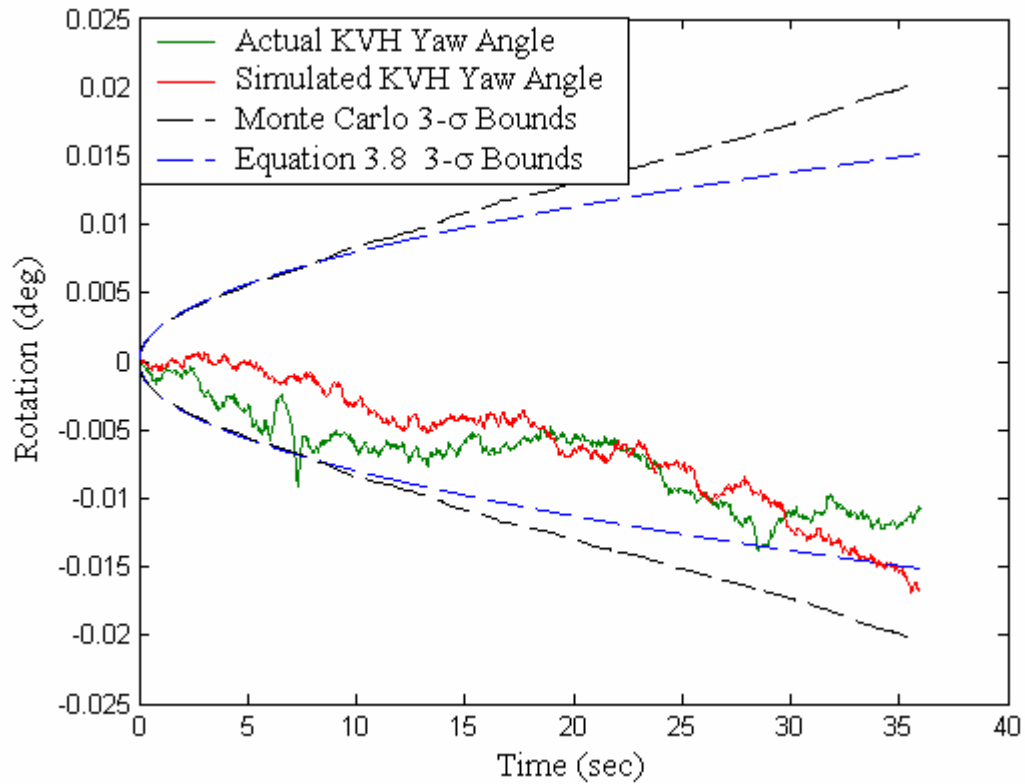


Figure 3.9 KVH Error Bound Comparison III

3.4 Longitudinal Velocity Error Equations

In the above section 3.3 it was shown that the moving bias definitely plays a key role in the heading error growth. To determine if the effects are similar in the position and velocity error growths analytical equations are derived. The derivations are for the analytical error growth of position and velocity errors due only to the integration of the wide band noise in the IMU.

To begin the derivations the bias of the accelerometer is assumed to be negligible. Therefore, the accelerometer measurement becomes

$$a_{\ddot{x}} = \ddot{x} + w_{accel} \quad (3.10)$$

where w_{accel} is uncorrelated wide band noise of the accelerometer.

Integration of the accelerometer times the heading angle to get longitudinal velocity (V_{North}) results in

$$V_{North} + V_{North}^e = \int (\ddot{x} + w_{accel}) \cos(\psi + \psi^e) dt \quad (3.11)$$

Assume the mean acceleration and heading are equal to zero to obtain

$$\begin{aligned} a &= 0 \\ \psi &= 0 \\ V_{North} &= 0 \end{aligned} \quad (3.12)$$

Therefore, the longitudinal velocity error (V_{North}^e) is due to the integration of the accelerometer's wide band noise time heading error.

$$V_{North}^e = \int (w_{accel}) \cos(\psi^e) dt \quad (3.13)$$

An Euler integration of the accelerometer output results in,

$$V_{North_{k+1}}^e = V_{North_k}^e + T_s w_{accel_k} \cos(\psi^e) \approx V_{North_k}^e + T_s w_{accel_k} = \sum_{k=1}^k T_s w_{accel_k} \quad (3.14)$$

Squaring and take the expected value of both equations results in

$$E[V_{North}^e (V_{North}^e)^T] = E\left[\left(\sum_{k=1}^k T_s w_{accel_k}\right) \left(\sum_{k=1}^k T_s w_{accel_k}\right)^T\right] \quad (3.15)$$

Simplify to get the following

$$E[V_{North}^e (V_{North}^e)^T] = T_s^2 \sum_{k=1}^k E[w_{accel_k} (w_{accel_k})^T] \quad (3.16)$$

Substitute in the covariance of the accelerometer wide band noise to obtain

$$E\left[V_{North}^e \left(V_{North}^e\right)^T\right] = T_s^2 \sigma_{w_{accel}}^2 k \quad T_s k = t \quad (3.17)$$

The above equations yield the following approximation for the longitudinal velocity error growth due to the integration of the yaw gyroscopes and accelerometers noises.

$$E\left[V_{North}^e \left(V_{North}^e\right)^T\right] = T_s t \sigma_{w_{accel}}^2 \quad (3.18)$$

Simplify to solve for the standard deviation of the longitudinal velocity.

$$\sigma_{V_{North}} = \sigma_{w_{accel}} \sqrt{T_s t} \quad (3.19)$$

3.5 Longitudinal Position Error Equations

The integration of the longitudinal velocity results in the longitudinal position.

$$P_{North} + P_{North}^e = \int \left(V_{North} + V_{North}^e \right) dt \quad (3.20)$$

Assume the mean longitudinal velocity and position are zero.

$$\begin{aligned} P_{North} &= 0 \\ V_{North} &= 0 \end{aligned} \quad (3.21)$$

Therefore, the longitudinal position error (P_{North}^e) is due to the integration of the longitudinal velocity error (V_{North}^e).

$$P_{North}^e = \int V_{North}^e dt \quad (3.22)$$

Again, an Euler integration method is used and results in

$$P_{North_{k+1}}^e = P_{North_k}^e + T_s V_{North_k}^e = \sum_{k=1}^k T_s V_{North_k}^e \quad (3.23)$$

Squaring and take the expected value of both equations results in,

$$E\left[P_{North}^e \left(P_{North}^e\right)^T\right] = E\left[\left(\sum_{k=1}^k T_s V_{North_k}^e\right) \left(\sum_{k=1}^k T_s V_{North_k}^e\right)^T\right] \quad (3.24)$$

Simplify to get the following.

$$E\left[P_{North}^e \left(P_{North}^e\right)^T\right] = T_s^2 \sum_{k=1}^k E\left[V_{North_k}^e \left(V_{North_k}^e\right)^T\right] = T_s^2 \sum_{k=1}^k \sigma_{V_{North}}^2 k \quad (3.25)$$

From the above section 3.4 the covariance of the longitudinal velocity was found to be,

$$\sigma_{V_{North}}^2 = T_s^2 \sigma_{w_{accel}}^2 k \quad (3.26)$$

Therefore, substituting in this for the longitudinal velocity covariance results in the following.

$$E\left[P_{North}^e \left(P_{North}^e\right)^T\right] = T_s^4 \sigma_{w_{accel}}^2 \sum_{k=1}^k k^2 = T_s^4 \sigma_{w_{accel}}^2 \left(\frac{1}{3}k^3 + \frac{1}{2}k^2 + \frac{1}{6}k\right) \quad (3.27)$$

The above equations result in the following approximation for the longitudinal position error growth due to the integration of the longitudinal velocity error:

$$E\left[P_{North}^e \left(P_{North}^e\right)^T\right] \approx \frac{1}{3}k^3 T_s^4 \sigma_{w_{accel}}^2 = \frac{1}{3}t^3 T_s \sigma_{w_{accel}}^2 \quad (3.28)$$

Simplify to solve for the standard deviation of the Northerly Position

$$\sigma_{P_{North}} = \sigma_{w_{accel}} \sqrt{\frac{1}{3} T_s t^3} \quad (3.29)$$

3.6 Lateral Velocity Error Equations

As in the longitudinal case the bias of the accelerometer will be assumed to be negligible in the accelerometer measurement. Because of this the following equation is derived:

$$a_{\ddot{x}} = \ddot{x} + w_{accel} \quad (3.30)$$

where w_{accel} is uncorrelated wide band noise of the accelerometer. Integration of the accelerometer times the heading angle to get lateral velocity (V_{East}) yeilds

$$V_{East} + V_{East}^e = \int (\ddot{x} + w_{accel}) \sin(\psi + \psi^e) \quad (3.31)$$

Assume the mean acceleration and heading are equal to zero, i.e

$$\begin{aligned} a &= 0 \\ \psi &= 0 \\ V_{North} &= 0 \end{aligned} \quad (3.32)$$

Then, the lateral velocity error (V_{East}^e) is due to the integration of the accelerometer's wide band noise time heading error.

$$V_{East}^e = \int (w_{accel}) \sin(\psi^e) \quad (3.33)$$

An Euler integration of the accelerometer output results in

$$V_{East_{k+1}}^e = V_{East_k}^e + T_s w_{accel_k} \sin(\psi^e) \approx V_{East_k}^e + T_s w_{accel_k} \psi_k^e = \sum_{k=1}^k T_s w_{accel_k} \psi_k^e \quad (3.34)$$

Squaring and take the expected value of both equations results in,

$$E \left[V_{East}^e (V_{East}^e)^T \right] = E \left[\left(\sum_{k=1}^k T_s w_{accel_k} \psi_k^e \right) \left(\sum_{k=1}^k T_s w_{accel_k} \psi_k^e \right)^T \right] \quad (3.35)$$

Knowing that the expected value of the square of the accelerometer noise is simply the covariance of the accelerometer wide-band noise ($\sigma_{w_{accel}}^2$) and that the gyroscope wide-band noise is uncorrelated to the accelerometer wide-band noise the lateral variance can be simplified to the following.

$$E\left[V_{East}^e (V_{East}^e)^T\right] = T_s^2 \sum_{k=1}^k E\left[w_{accel_k} (w_{accel_k})^T\right] E\left[\psi_k^e (\psi_k^e)^T\right] \quad (3.36)$$

$$E\left[V_{East}^e (V_{East}^e)^T\right] = T_s^2 \sum_{k=1}^k \sigma_{w_{accel}}^2 E\left[\psi_k^e (\psi_k^e)^T\right] \quad (3.37)$$

From reference [Bevly] and the above section 3.5:

$$E\left[\psi_k^e (\psi_k^e)^T\right] = \sigma_g^2 = T_s^2 k \sigma_{w_{gyro}}^2 \quad (3.38)$$

Therefore,

$$E\left[V_{East}^e (V_{East}^e)^T\right] = T_s^4 \sum_{k=1}^k k \sigma_{w_{accel}}^2 \sigma_{w_{gyro}}^2 = T_s^4 \sigma_{w_{accel}}^2 \sigma_{w_{gyro}}^2 \sum_{k=1}^k k = T_s^4 \sigma_{w_{accel}}^2 \sigma_{w_{gyro}}^2 \frac{1}{2} (k^2 + k) \quad (3.39)$$

$$\approx \frac{1}{2} T_s^4 \sigma_{w_{accel}}^2 \sigma_{w_{gyro}}^2 k^2 \quad T_s k = t \quad (3.40)$$

The above equations result in the following approximation for the lateral velocity error growth due to the integration of the yaw gyroscopes and accelerometers noises:

$$E\left[V_{East}^e (V_{East}^e)^T\right] = \frac{1}{2} T_s^2 t^2 \sigma_{w_{accel}}^2 \sigma_{w_{gyro}}^2 \quad (3.41)$$

Simplify to solve for the standard deviation of the lateral velocity,

$$\sigma_{V_{East}} = \sigma_{w_{accel}} \sigma_{w_{gyro}} T_s t \sqrt{\frac{1}{2}} \quad (3.42)$$

3.7 Lateral Position Error Equations

The integration of the lateral velocity results in the lateral position.

$$P_{East} + P_{East}^e = \int (V_{East} + V_{East}^e) dt \quad (3.43)$$

Assume the mean lateral velocity and position are zero,

$$\begin{aligned} P_{East} &= 0 \\ V_{East} &= 0 \end{aligned} \quad (3.44)$$

So that, the longitudinal position error (P_{East}^e) is due to the integration of the longitudinal velocity error (V_{East}^e), i.e.

$$P_{East}^e = \int V_{East}^e dt \quad (3.45)$$

Again, an Euler integration method is used and results in,

$$P_{East_{k+1}}^e = P_{East_k}^e + T_s V_{East_k}^e = \sum_{k=1}^k T_s V_{East_k}^e \quad (3.46)$$

Squaring and take the expected value of both equations results in,

$$E \left[P_{East}^e (P_{East}^e)^T \right] = E \left[\left(\sum_{k=1}^k T_s V_{East_k}^e \right) \left(\sum_{k=1}^k T_s V_{East_k}^e \right)^T \right] \quad (3.47)$$

Simplify the position variance to get the following

$$E \left[P_{East}^e (P_{East}^e)^T \right] = T_s^2 \sum_{k=1}^k E \left[V_{East_k}^e (V_{East_k}^e)^T \right] = T_s^2 \sum_{k=1}^k \sigma_{East_k}^2 k \quad (3.48)$$

From the above section the covariance of the longitudinal velocity was found to be,

$$\sigma_{V_{East}}^2 \approx T_s^4 \sigma_{w_{accel}}^2 \sigma_{w_{gyro}}^2 \frac{1}{2} k^2 \quad (3.49)$$

Therefore substituting in this for the longitudinal velocity covariance results in,

$$E \left[P_{East}^e (P_{East}^e)^T \right] = \frac{1}{2} T_s^6 \sigma_{w_{accel}}^2 \sigma_{w_{gyro}}^2 \sum_{k=1}^k k^3 = \frac{1}{2} T_s^6 \sigma_{w_{accel}}^2 \sigma_{w_{gyro}}^2 \left(\frac{1}{4} k^4 + \frac{1}{2} k^3 + \frac{1}{4} k^2 \right) \quad (3.50)$$

The above equations result in the following approximation for the longitudinal position error growth due to the integration of the longitudinal velocity error:

$$E\left[P_{East}^e (P_{East}^e)^T\right] \approx \frac{1}{8} k^4 T_s^6 \sigma_{w_{accel}}^2 \sigma_{w_{gyro}}^2 = \frac{1}{8} t^4 T_s^2 \sigma_{w_{accel}}^2 \sigma_{w_{gyro}}^2 \quad (3.51)$$

Simplify to solve for the standard deviation of the Northerly Position

$$\sigma_{P_{East}} = \sigma_{w_{accel}} \sigma_{w_{gyro}} T_s t^2 \sqrt{\frac{1}{8}} \quad (3.52)$$

3.8 Bias Contribution in the IMU Integration Error

The equations for the position and velocity errors provided in sections 3.4 -3.7 make it possible to evaluate the effect a moving bias has on the error growth. Figures 3.10 and 3.11 are a comparison of these analytical equations and the position and velocity error growths from a Monte Carlo simulation. The Monte Carlo simulation was done with the simple model in chapter 2 using Tactical Grade IMU characteristics.

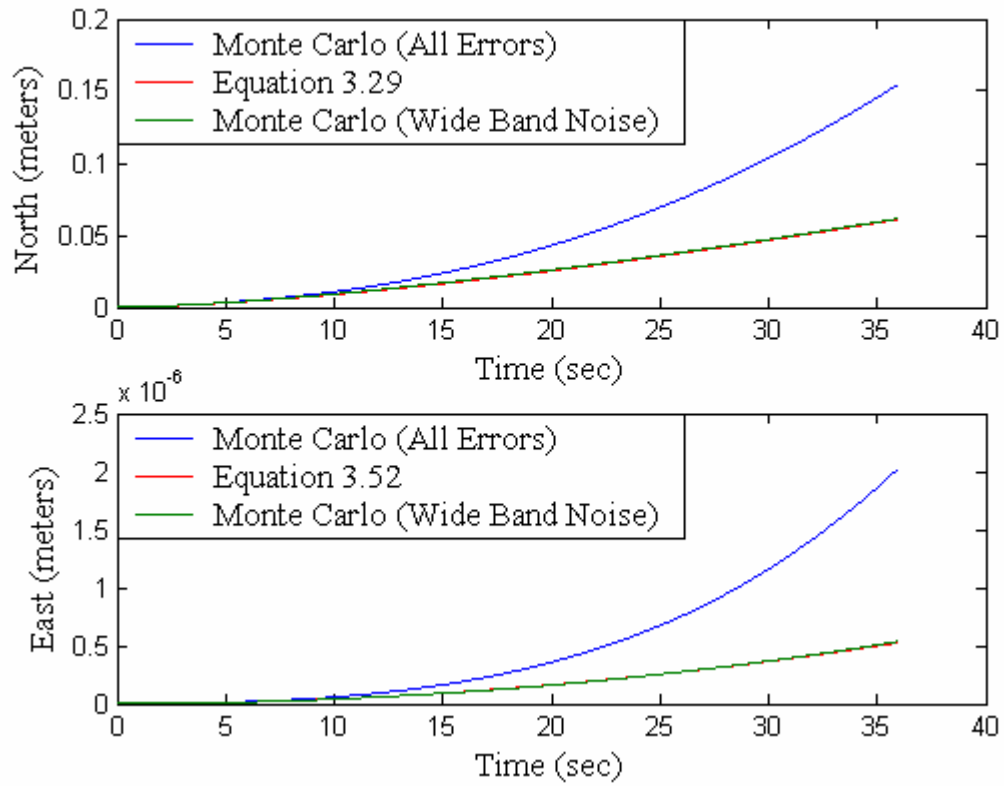


Figure 3.10 Comparison of a Tactical Grade IMU Position Error Bounds (Static)

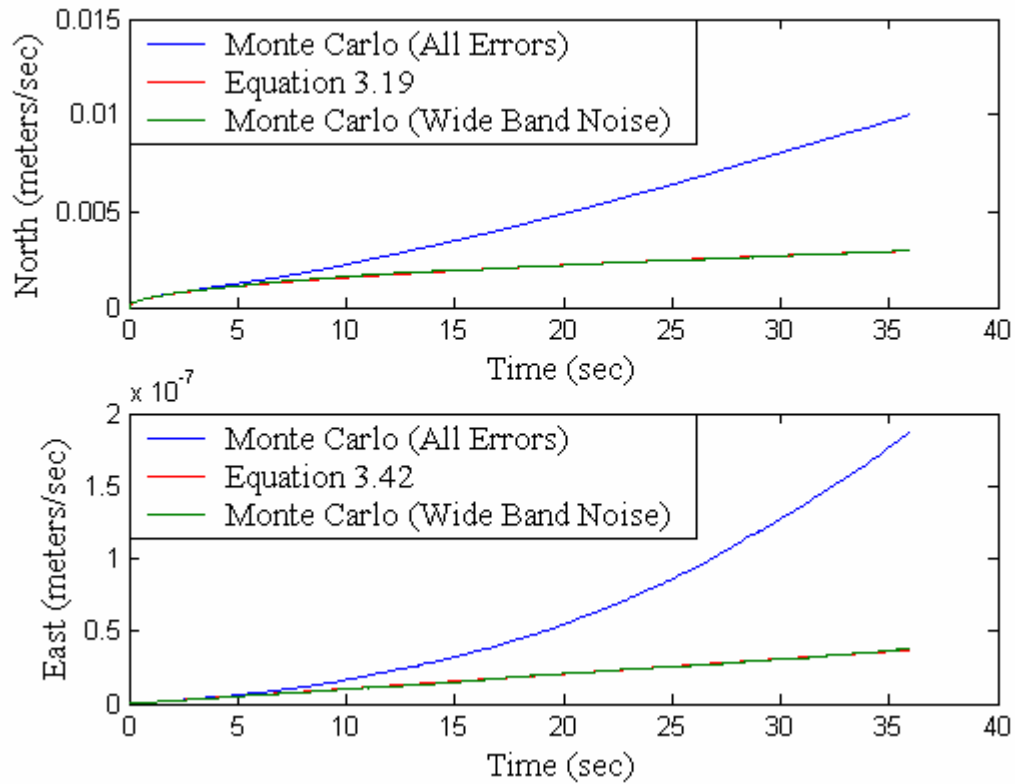


Figure 3.11 Comparison of a Tactical Grade IMU Velocity Error Bounds (Static)

The error growth rates in the curves of the Monte Carlo simulations, which contain both the wide band noise and bias errors, are much faster than the growth rates of the curves which only contain the wide band noise error source. This is confirmation that the moving bias, even in the best of sensors, plays a key roll in error growth over time. Figures 3.12 and 3.13 contain curves of the difference between the error bound equations derived in sections 3.4-3.7 above and the error bounds which resulted from the Monte Carlo simulations, which contain all of the error sources.

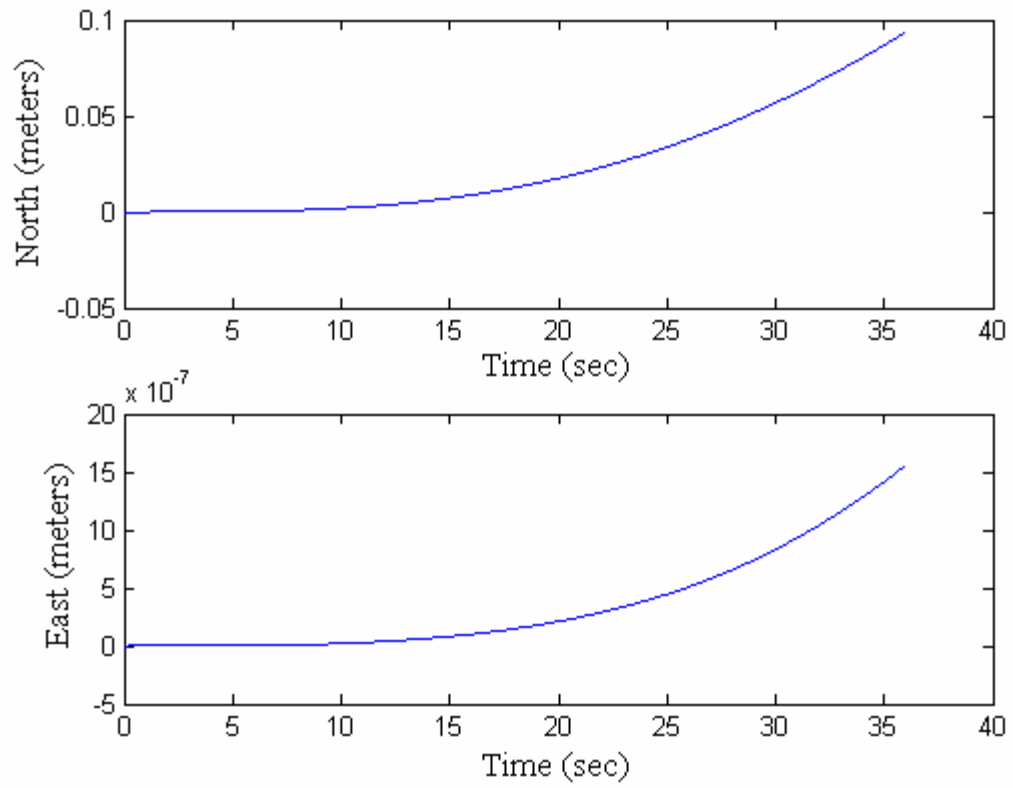


Figure 3.12 Effect of Tactical Grade IMU Biases on Position Error (Static)

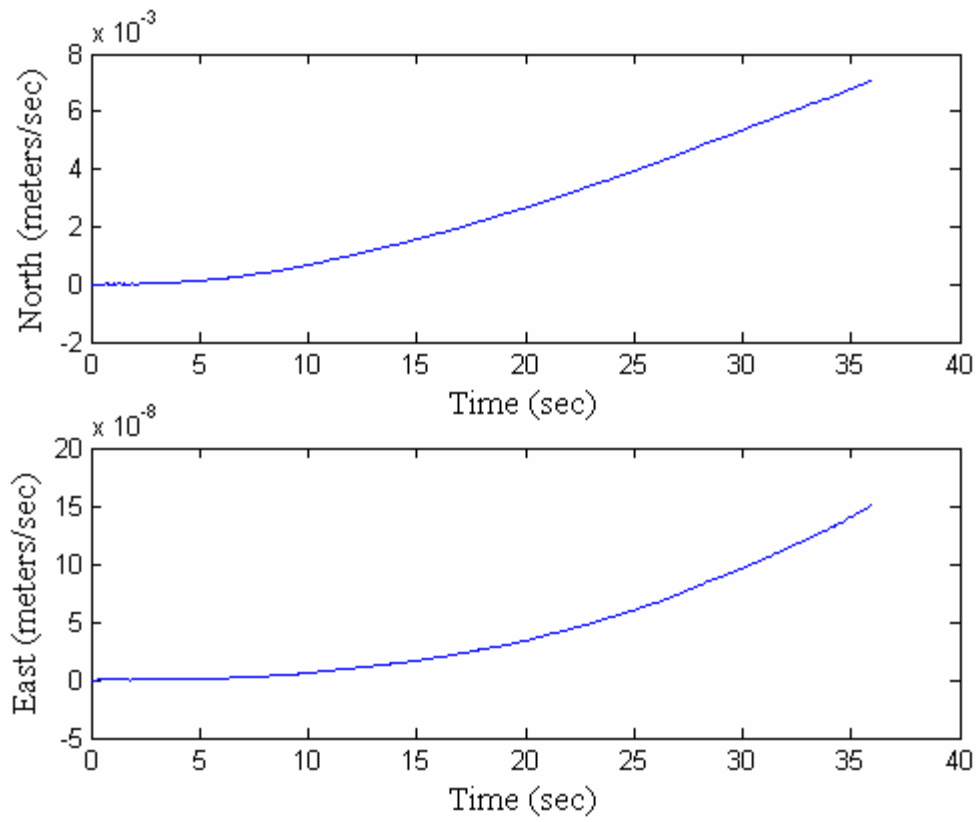


Figure 3.13 Effect of Tactical Grade IMU Biases on Velocity Error (Static)

3.9 Gravitational Effects

The navigation scenario laid out in section 3.1 is one which involves planar motion in the East-North coordinates. In some cases it is necessary to measure the distance traveled in the North-Up coordinates. When it is necessary to navigate up the accelerometer is affected by the gravitational field of the earth. This introduces an additional error in the upward acceleration measurement because of errors in the pitch angle ϑ calculation. Below are the state space matrices modified to account for the gravitational effects on the accelerometer.

The state space gravity input matrix is:

$$G = \begin{bmatrix} 0 \\ 0 \\ 0 \\ \sin(\vartheta) \end{bmatrix} \quad (3.53)$$

Where,

$$g = 9.80665 \frac{m}{s^2} \quad (3.54)$$

The position calculation then becomes

$$f_{positon} = A[states] + B[\ddot{x}] - G[g] \quad (3.55)$$

Figures 3.14 and 3.15 are the position and velocity bounds when tactical grade IMU characteristics are used. Figures 3.16 and 3.17 are the position and velocity bounds when consumer grade IMU characteristics are used

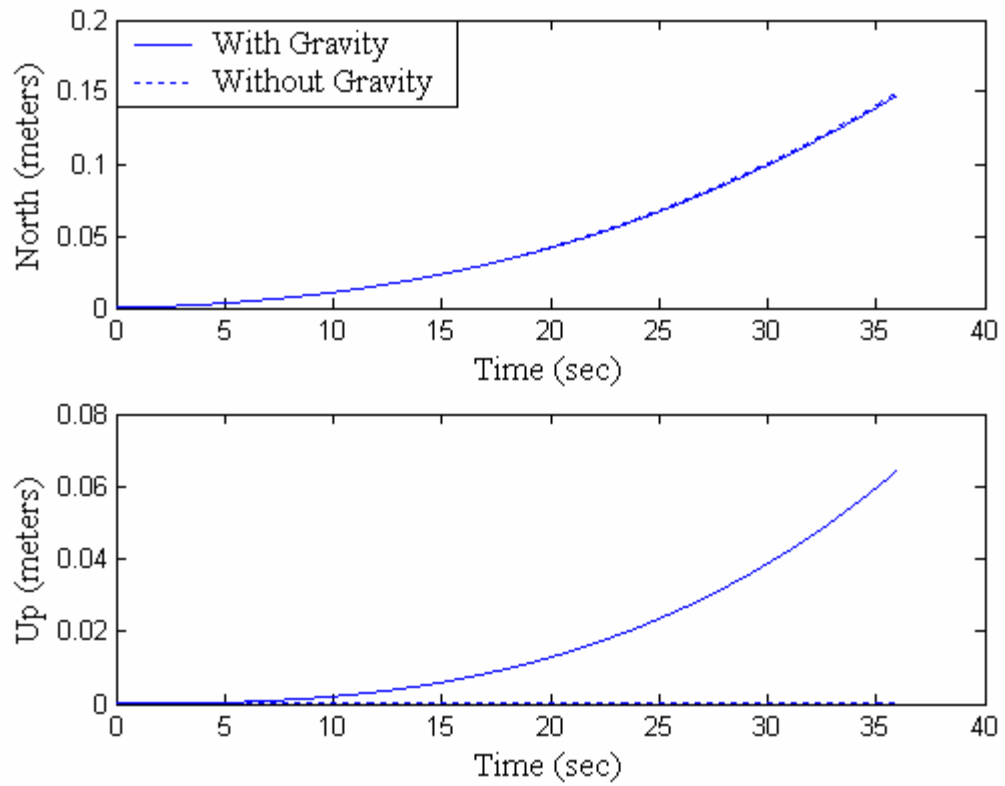


Figure 3.14 Tactical Grade IMU Position Error Bounds with Gravity Field

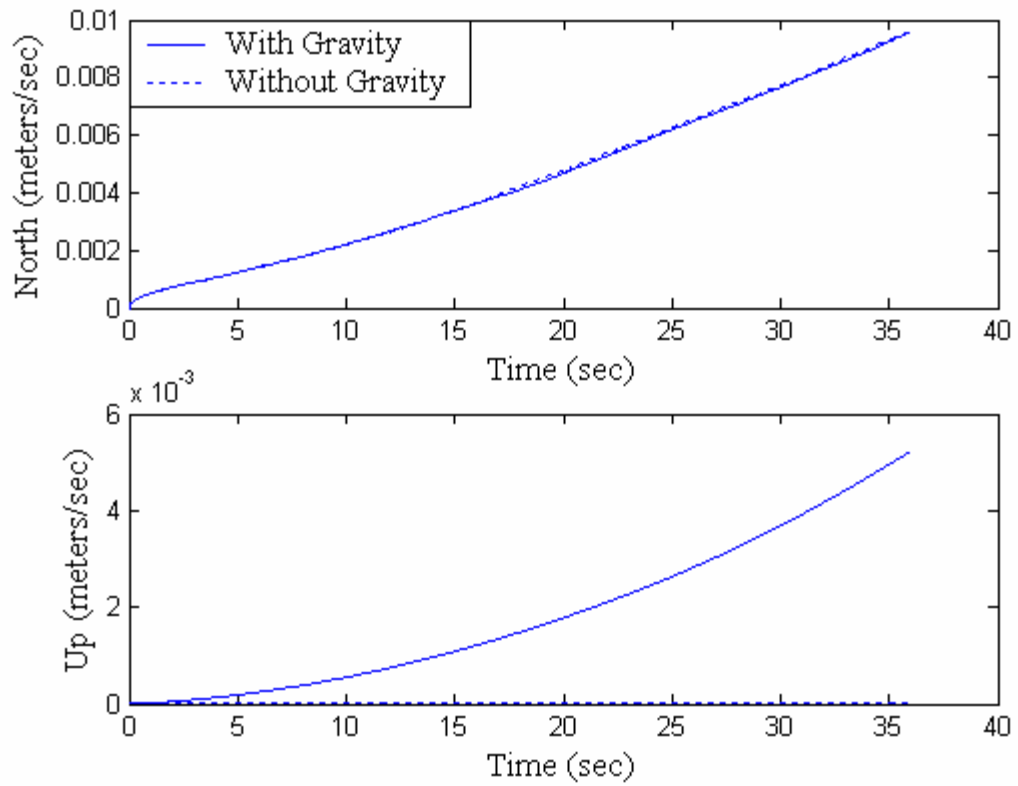


Figure 3.15 Tactical Grade IMU Velocity Error Bounds with Gravity Field

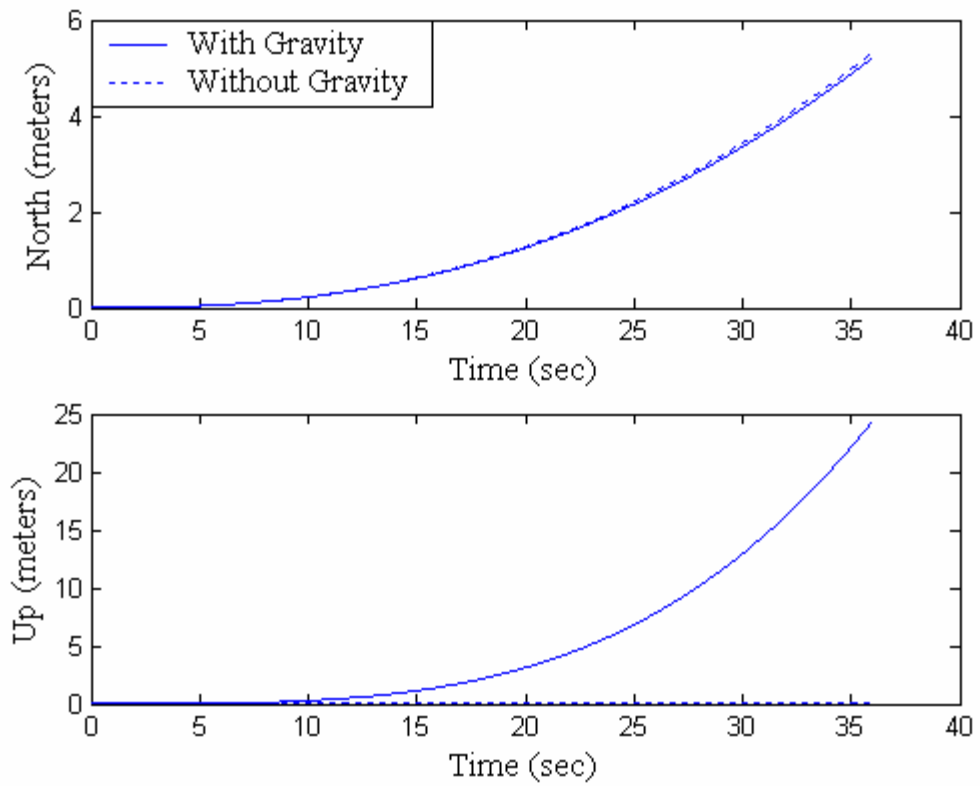


Figure 3.16 Consumer Grade IMU Position Error Bounds with Gravity Field

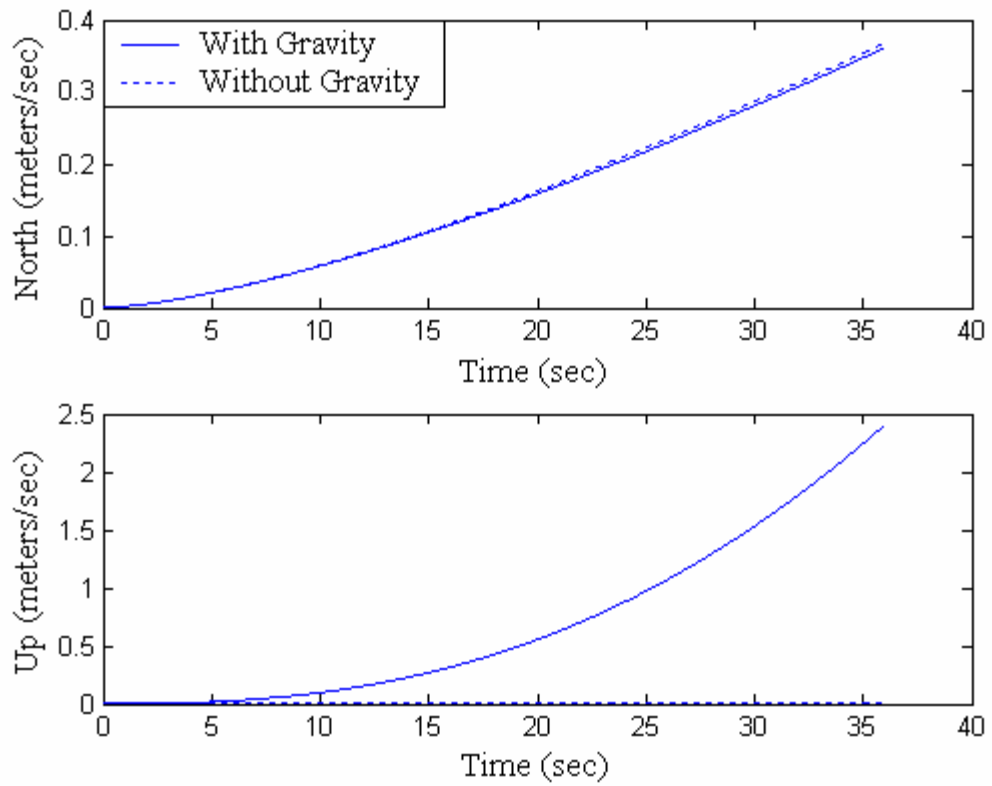


Figure 3.17 Consumer Grade IMU Velocity Error Bounds with Gravity Field

3.10 Summary and Conclusions

In this chapter the errors associated with the integration of a single rate gyro and single accelerometers to calculate position, velocity and heading in a planar setting were discussed. The error growths of the position, velocity, and heading calculation were depicted with the use of a Monte Carlo Simulation. Both consumer and tactical grade sensor characteristics were compared and experimental data was used to validate the bounds of the Monte Carlo simulations. The Monte Carlo simulations were validated by showing the error growths of rate gyros and accelerometers which contain moving biases, and comparing them to simulations where the only error source was wide-band noise. Analytical equations for position, velocity and heading errors were derived which plot the error growths depicted by the integration of rate gyros and accelerometers, which contain only one error source, wide-band noise. Finally, a gravity field was introduced. The error growths of the position and velocity calculations were compared with a gravity field and without.

CHAPTER 4

INTEGRATION ERROR CORRECTIONS FOR A TWO DEGREE OF FREEDOM INERTIAL MEASUREMENT UNIT

4.1 Introduction

A Kalman Filter will be implemented to combine the GPS position, velocity and heading measurements with the inertial sensor measurements. The Kalman filter will incorporate the sensor model presented in Chapter 2. The coupling of the GPS measurements and the sensor model to calculate the position, velocity and heading from the combined GPS and IMU measurements will result in new error bounds for position, velocity and heading. The Kalman Filter will also provide an estimation of the biases associated with each sensor. Experimental data will be used to validate the bias and error bound estimations. This will be useful when designing controllers that need a better estimation of position, velocity and heading than a normally received from an integrated IMU measurement.

4.2 Heading Error Reduction with a Two State Kalman Filter

The position, velocity and heading calculations from an integrated IMU contain several errors, as shown in the previous chapters. The goal of this chapter is to reduce

these errors with the aid of the Global Positioning System. GPS returns a calculated position, velocity and heading that is very precise. However, in order to preserve the precision of GPS, the messages are typically restricted to an output frequency of 1-10 Hz. This is not a very desirable output rate when precise and high update rate navigation is required. To increase the output rate, the GPS and an IMU can be coupled together with a Kalman filter.

A Kalman filter is a state estimator that uses the knowledge of the input error sources to assist in estimating the true state through time. A Kalman filter is a good coupling tool to use in the above scenarios due to the fact that the GPS measurements are unbiased, but are received at a very low frequency, and the IMU measurements are relatively imprecise and can be received at relatively high frequencies. For a more detailed description of a Kalman filter refer to Appendix C.

Below is the first state space navigation model that is commonly implemented in a Kalman filter to estimate heading. This two state model allows the Kalman filter to estimate the heading of the platform and approximates the bias in the rate gyro measurement as a constant. Note that the actual variance on the bias is not zero. If it were zero the bias state would be modeled as a constant. Since there is variance in place, the bias state is actually modeled as a random walk. This is to keep the Kalman filter from “going to sleep”. The Kalman filter is considered to be “asleep” when the gains are unchangeable. In either case, the bias estimate will remain as a constant when no GPS measurement is available.

2-State Kalman filter state space matrices:

$$x = \begin{bmatrix} \theta \\ bias_{const} \end{bmatrix} \quad (4.1)$$

$$A_{kal} = \begin{bmatrix} 0 & -1 \\ 0 & 0 \end{bmatrix} \quad (4.2)$$

$$B_{kal} = \begin{bmatrix} 1 \\ 0 \end{bmatrix} \quad (4.3)$$

$$C_{kal_{GPS_{on}}} = [1 \ 0] \quad (4.4)$$

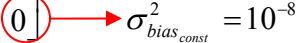
$$C_{kal_{GPS_{off}}} = [0 \ 0] \quad (4.5)$$

$$D_{kal} = [0] \quad (4.6)$$

The following noise covariance matrices were used to calculate the Kalman filter gains.

$$B_w = \begin{bmatrix} 1 & 0 \\ 0 & 1 \end{bmatrix} \quad (4.7)$$

$$Q_w = \begin{bmatrix} \sigma_{noise}^2 / \sqrt{f_s} & 0 \\ 0 & 0 \end{bmatrix} \quad (4.8)$$



$$R = [\sigma_{GPS}^2] \quad (4.9)$$

Below is the second state space navigation model that is commonly implemented in a Kalman filter to estimate heading. This two state model allows the Kalman filter to estimate the heading of the platform and approximates the bias in the rate gyro measurement as a first order Markov process. Note that the bias estimate will tend to zero when there is no GPS measurement available. This is because the model assumes

the Markov process is zero mean. Therefore, the best estimate is that the bias is zero over all time if no other information is available.

2-State Kalman filter state space matrices:

$$x = \begin{bmatrix} \mathcal{G} \\ bias_{walking} \end{bmatrix} \quad (4.10)$$

$$A_{kal} = \begin{bmatrix} 0 & -1 \\ 0 & -\frac{1}{\tau} \end{bmatrix} \quad (4.11)$$

$$B_{kal} = \begin{bmatrix} 1 \\ 0 \end{bmatrix} \quad (4.12)$$

$$C_{kal_{GPS_{on}}} = [1 \ 0] \quad (4.13)$$

$$C_{kal_{GPS_{off}}} = [0 \ 0] \quad (4.14)$$

$$D_{kal} = [0] \quad (4.15)$$

The following noise covariance matrices were used to calculate the Kalman filter gains.

$$B_w = \begin{bmatrix} 1 & 0 \\ 0 & 1 \end{bmatrix} \quad (4.16)$$

$$Q_w = \begin{bmatrix} \frac{\sigma_{noise}^2}{\sqrt{f_s}} & 0 \\ 0 & \frac{2f_s\sigma_{bias}^2}{\tau} \end{bmatrix} \quad (4.17)$$

$$R = [\sigma_{GPS}^2] \quad (4.18)$$

The selection of each of these models is important before setting up a Kalman filter. However, the effects are only seen during GPS outages and will be discussed in the following section.

The following figures are a comparison of the error bounds when the 2-State Kalman Filter is used versus when the rate gyro is integrated using Rugge-Kutta order four. Figure 4.1 is a plot of the results from a consumer grade rate gyro. Figure 4.2 is a plot of the results from a Tactical grade rate gyro.

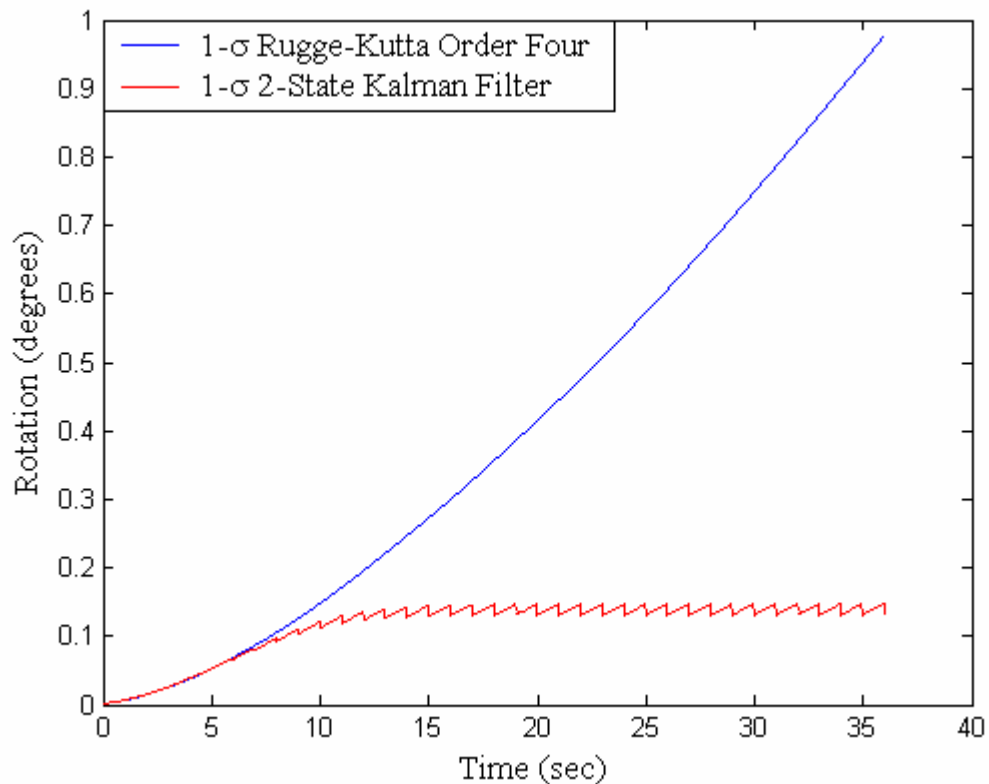


Figure 4.1

Consumer Grade Heading Error Comparison between the 2 state Kalman Filter Model and Rugge-Kutta Order Four.

As seen in Figure 4.1, coupling the rate gyro with GPS bounds the error. For a consumer grade rate gyro, the Kalman filter reaches steady state around 15 seconds.

Once the Kalman filter has reached steady state, the heading error is bound between 0.1 degrees and 0.2 degrees.

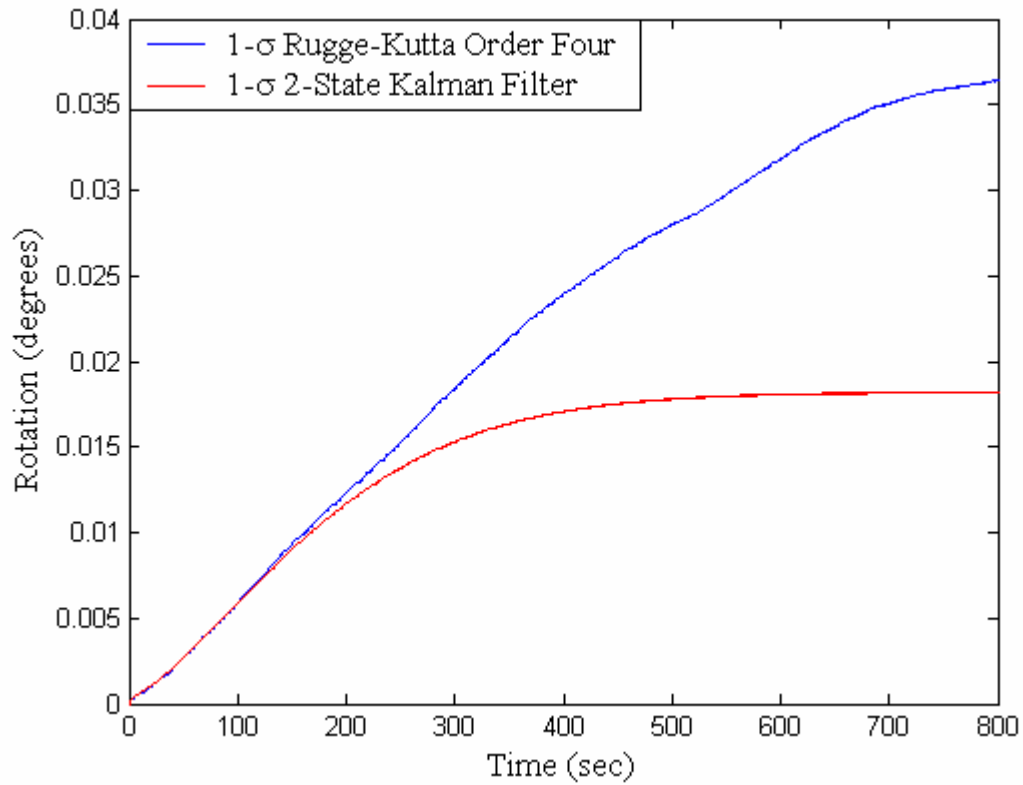


Figure 4.2

Tactical Grade Heading Error Comparison between the 2 state Kalman Filter Model and Rugge-Kutta Order Four.

For a tactical grade rate gyro, the Kalman filter takes much longer, approximately 700 seconds, to reach steady state. However, once the Kalman filter reaches steady state, the heading error is bound between .015 degrees and .02 degrees.

4.3 Heading Errors during a GPS Outage

Since it has been shown that the errors of an inertial sensor can be bound by coupling them with GPS, the effects of a GPS outage are now investigated. The first case illustrates what happens during a GPS outage while modeling the bias as a first order Markov process using a consumer grade sensor. Figure 4.3 shows the heading and bias states of the Kalman filter. GPS is denied to the Kalman filter at $t = 180$ seconds, this is known as a GPS outage. As seen in Figure 4.3, once the outage begins, the bias state converges to zero. This is expected since the bias is being modeled as a first order Markov process which has a zero mean.

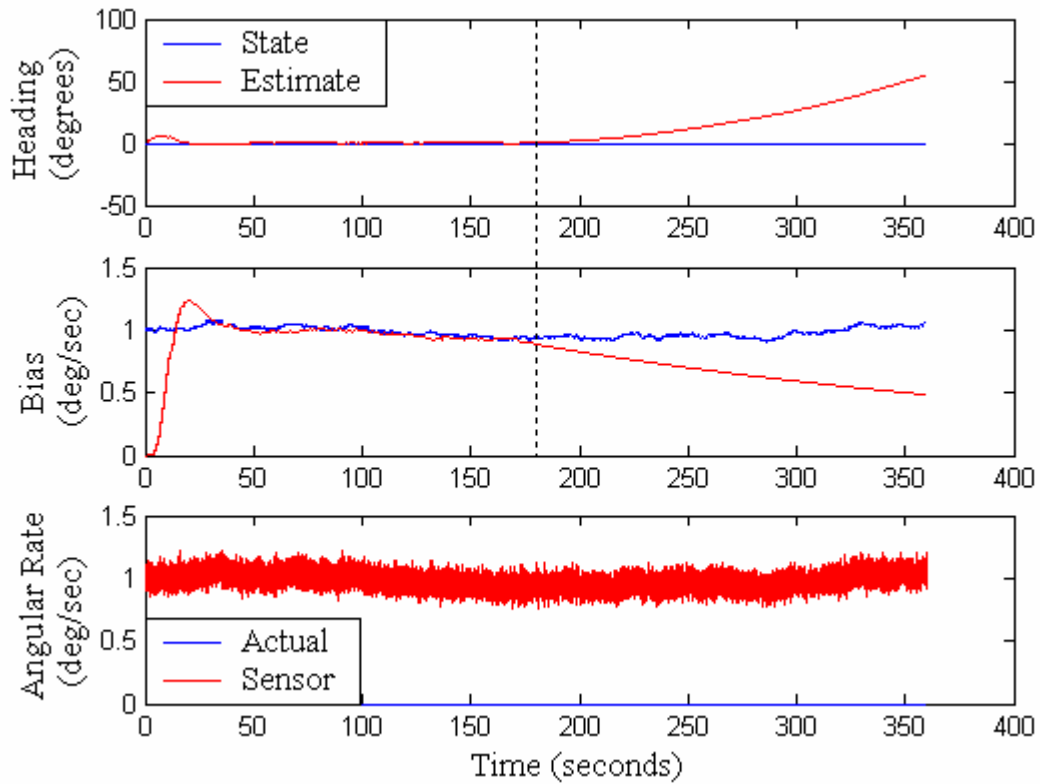


Figure 4.3

State Estimates for a Two State Kalman Filter with the Second State Modeled as a 1st Order Markov Process

The second case is a GPS outage with the bias modeled as a constant (random walk). Figure 4.4 shows the heading and bias states of the Kalman filter. Again a GPS outage was simulated at 180 seconds. As seen in the figure, the bias state remains constant after the GPS outage. This is expected since the bias is modeled as a constant.

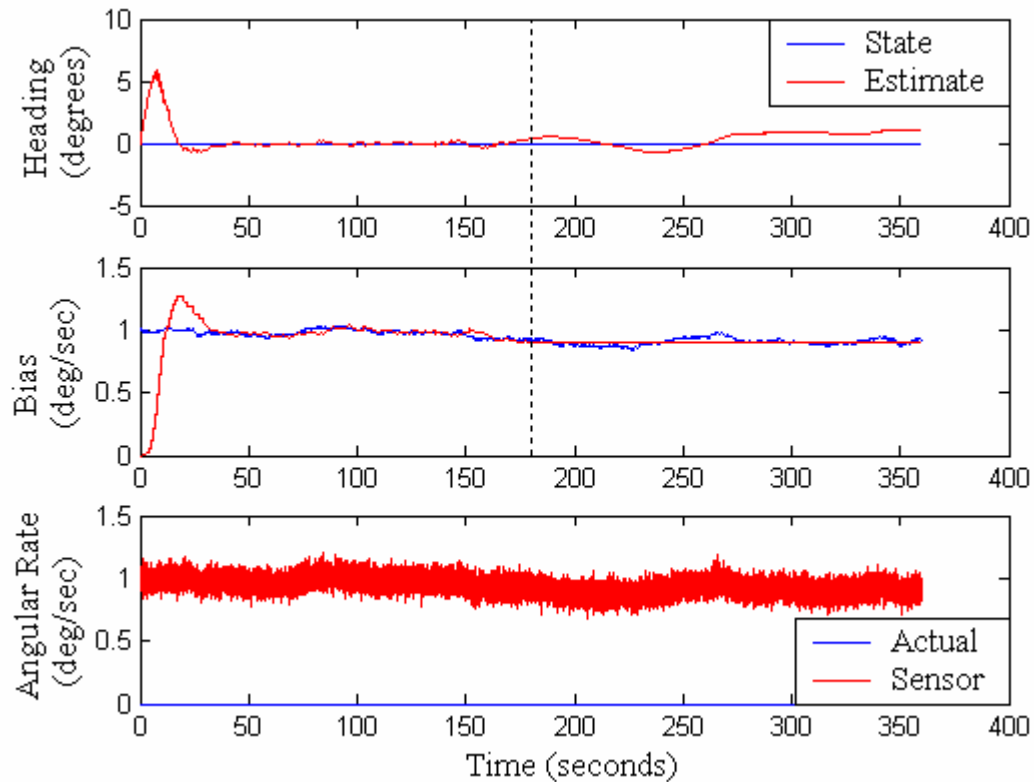


Figure 4.4

State Estimates for a Two State Kalman Filter with the Second State Modeled as a Random Walk

Two Monte Carlo simulations were performed with a consumer grade gyro to determine which bias model (constant or Markov) performs better. The first Monte Carlo simulation assumes a moving bias dominates the sensor measurement. This simulation used a constant bias of zero. The second Monte Carlo simulation assumes a constant bias of 1 deg/sec dominates the sensor measurement.

As seen in Figure 4.5, the error bounds on the heading estimate grow much faster when the bias was modeled as a constant. The difference between the error bound

estimated by the Kalman filter and the error bound calculated when the bias was modeled as a Markov process can most likely be contributed to the number of iteration used in the Monte Carlo simulation. Sixty iterations were used for this simulation because of computer memory constraints.

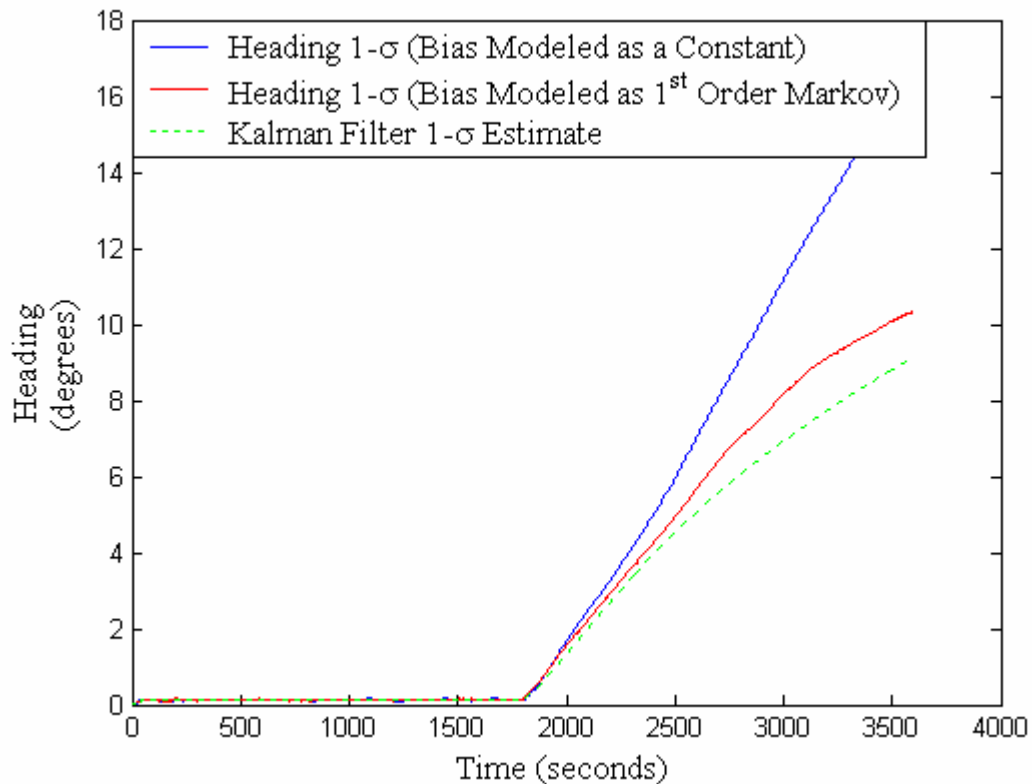


Figure 4.5

Error Bound Comparison between the Two State Kalman Filter Models when the Dominate Bias is not Constant

As seen in Figure 4.6 the error bounds on the heading estimate grows much faster when the bias is modeled as a Markov process. The difference between the error bound

estimated by the Kalman filter and the error bound calculated when the bias was modeled as a constant is again most likely contributed to the number of iteration used in the Monte Carlo simulation. Sixty iterations were used because of computer memory constraints.

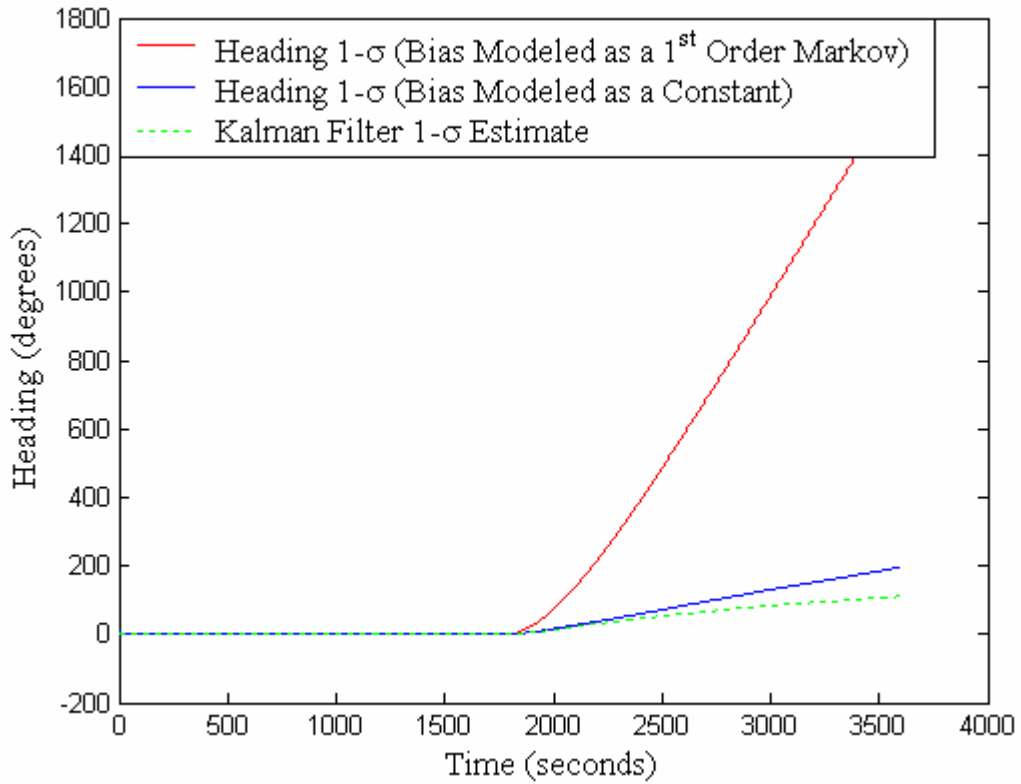


Figure 4.6

Error Bound Comparison between the Two State Kalman Filter Models when the Dominate Bias is a Constant

4.4 Heading Error Reduction with a Three State Kalman Filter

Accurately modeling a sensor bias with a two state Kalman filter is difficult because the bias can contain both constant and moving components. To improve the heading estimate of a Kalman filter, the following three state model was created. With this model, it is possible to estimate both the moving and constant biases of an inertial sensor, instead of estimating only one or the other with the two state Kalman filter. Note that during a GPS outage the constant bias estimate will remain constant, and the moving bias estimate will tend to zero.

3-State Kalman Filter state space matrices:

$$x = \begin{bmatrix} \mathcal{H} \\ bias_{walking} \\ bias_{constant} \end{bmatrix} \quad (4.19)$$

$$A_{kal} = \begin{bmatrix} 0 & -1 & -1 \\ 0 & -\frac{1}{\tau} & 0 \\ 0 & 0 & 0 \end{bmatrix} \quad (4.20)$$

$$B_{kal} = \begin{bmatrix} 1 \\ 0 \\ 0 \end{bmatrix} \quad (4.21)$$

$$C_{kal_{GPS_{on}}} = [1 \ 0 \ 0] \quad (4.22)$$


$$C_{kal_{GPS_{off}}} = [0 \ 0 \ 0] \quad (4.23)$$

$$D_{kal} = [0] \quad (4.24)$$

The following noise covariance matrices were used to calculate the Kalman filter gains.

$$B_w = \begin{bmatrix} 1 & 0 & 0 \\ 0 & 1 & 0 \\ 0 & 0 & 1 \end{bmatrix} \quad (4.25)$$

$$Q_w = \begin{bmatrix} \frac{\sigma_{noise}^2}{\sqrt{f_s}} & 0 & 0 \\ 0 & \frac{2f_s \sigma_{bias_{moving}}^2}{\tau} & 0 \\ 0 & 0 & 0 \end{bmatrix} \quad (4.26)$$



$$R = [\sigma_{GPS}^2] \quad (4.27)$$

This three state model allows the Kalman Filter to estimate the heading of the platform as well as the moving bias and constant bias of the rate gyro. The following figures are a comparison of the error bounds when a 3-State Kalman Filter is used, a 2 state Kalman Filter is used and a Runge-Kutta order four integration scheme is used. Figure 4.7 is a plot of the results from a consumer grade rate gyro. As seen in the figure, when the inertial sensor is integrated the error bounds continue to grow through time. When the two state Kalman filter is implemented, the error bounds grow and are eventually bound between a thresholds. The three state Kalman filter is also able to bound the errors to the same threshold but not before a time of extreme uncertainty. This is due to the initialization of the Kalman filter covariance matrix.

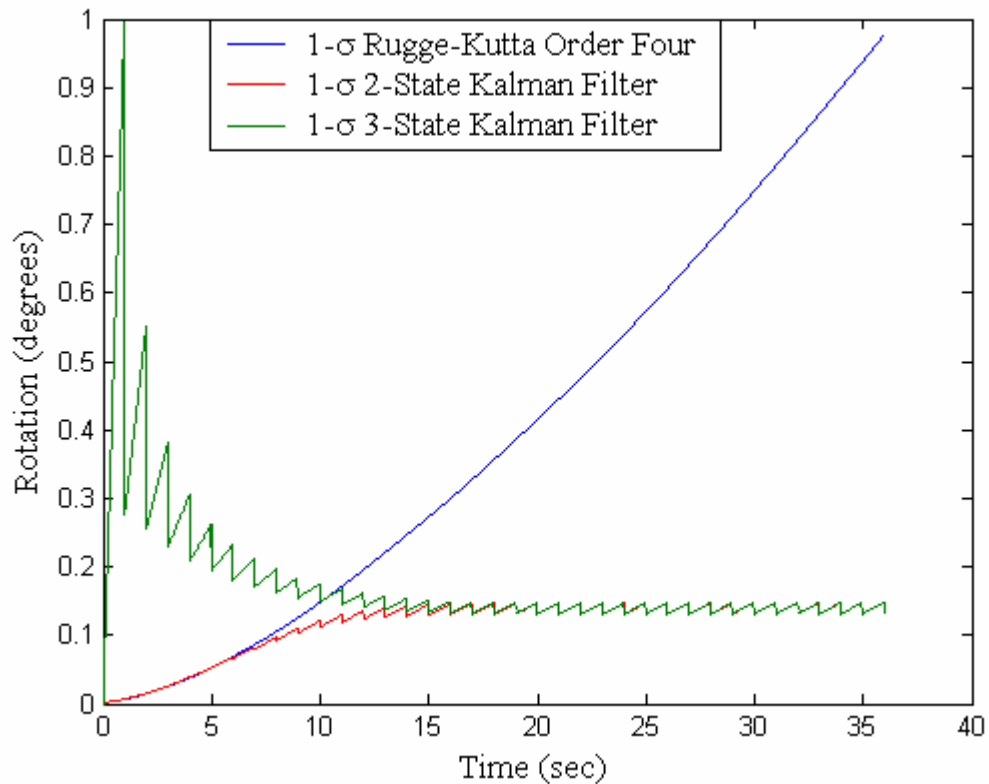


Figure 4.7

Consumer Grade Heading Error Comparison between the 3 State Kalman Filter Model, the 2 State Kalman Filter Model and A Rugge-Kutta Order Four Integration Method.

4.5 Kalman Filter Comparison

To show the utility of the three state Kalman filter, the experimental data taken from the Systron-Donner AQRS-104 presented in Figure 2.3 will be filtered with each of the two state Kalman filter models and then the three state Kalman filter. During the filtering process, a GPS outage was created after 30 minutes. Figure 4.8 is a plot of the heading and bias states estimated by the Kalman filter when the two state Kalman filter

that models the bias as a constant (random walk) is used. As seen in the figure the bias remains constant after the GPS outage begins. The important thing to notice is at what value the bias remains. Because the actual bias is not constant but rather moving about some mean value that is not zero when the outage begins, the Kalman filter holds the bias state at its last estimated value. Since the value is not exactly equal to the actual bias, there is an error introduced into the heading estimate.

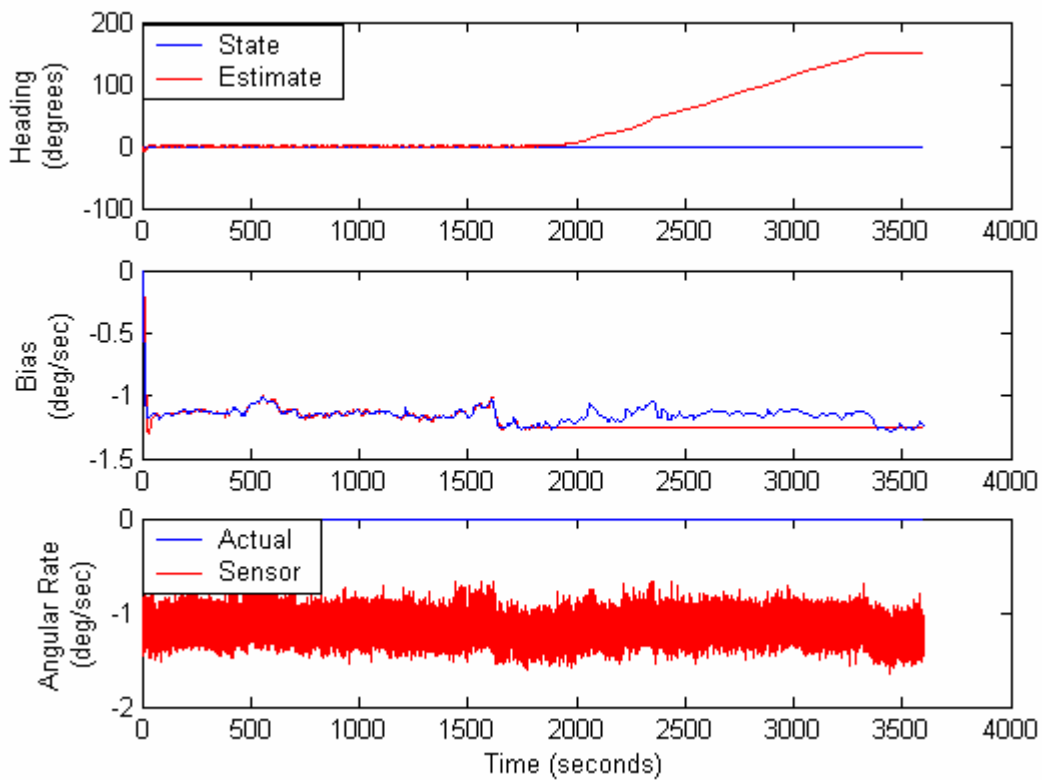


Figure 4.8

Systron-Donner State Estimates for a Two State Kalman Filter with the Second State Modeled as a Random Walk

The sensor data is now filtered by using the two state Kalman filter model that models the bias as a first order Markov process. Figure 4.9 is a plot of the heading and bias states estimated by the Kalman filter. As seen in the figure, the bias estimate begins to converge to zero after the GPS outage begins. Because the bias estimate converges to zero and the actual bias is walking about a mean value less than zero degrees per second, the heading estimate will contain large errors after the GPS outage begins.

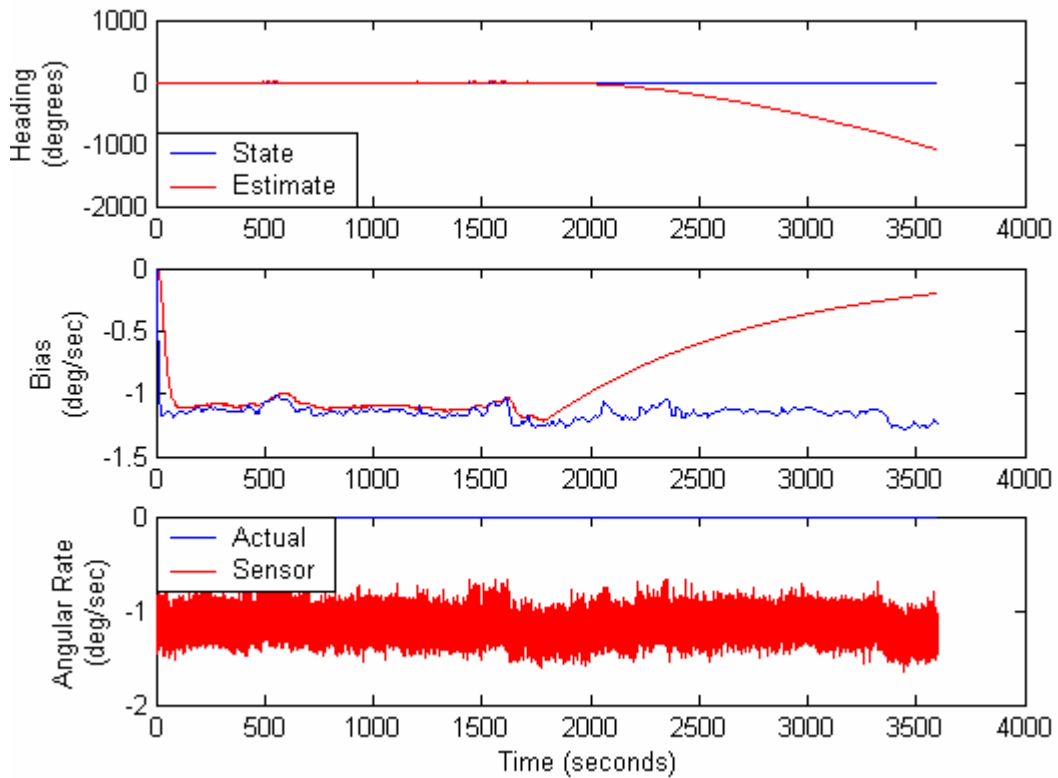


Figure 4.9

Systron-Donner State Estimates for a Two State Kalman Filter with the Second State Modeled as a 1st Order Markov Process.

This actual sensor is dominated by a bias that contains more than one component, and the components are of similar magnitudes. The bias has a definite mean value that is not equal to zero, but this mean value has stability issues. Because of drift issues, the bias is not always at that mean value. This occurs frequently in consumer grade sensors. To show the utility of the three state Kalman filter model, the experimental data taken from the Systron-Donner rate gyro is filtered using the three state Kalman filter. Again a GPS outage was created after 30 minutes. Figure 4.10 are the Kalman filter states shown versus time while the three states model was used. As seen in the figure, the filter is able to correctly estimate the heading, moving bias and constant bias while GPS is in place. When the GPS outage occurs, the moving bias estimate converges to zero, and the constant bias estimate remains constant. With the bias states behaving according to their statistical values, the error in the heading estimate is minimized.

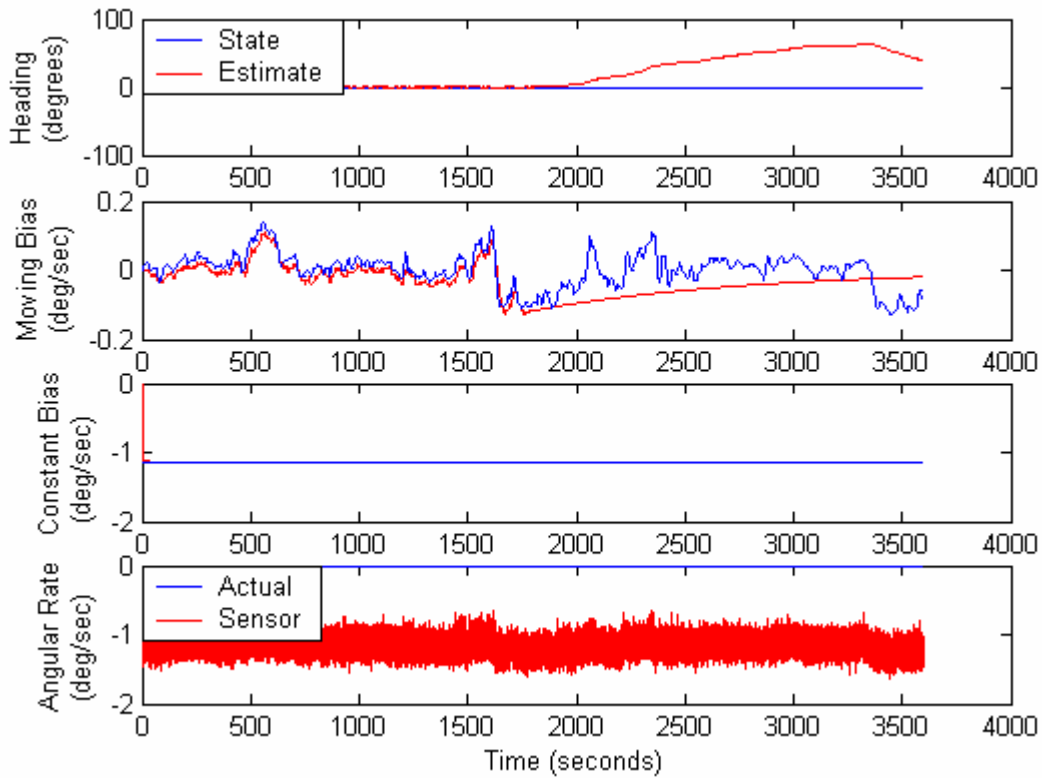


Figure 4.10

Sysron-Donner State Estimates for a Three State Kalman Filter with the Second State Modeled as a 1st Order Markov Process and the Third State Modeled as a Random Walk.

4.6 Position Estimation with a Six State Kalman Filter

Like the heading calculation, the position calculation can also be improved by using a Kalman filter. However, because the inertial sensor measurement is acceleration, the Kalman filter must double integrate to estimate the position. The following is a six state Kalman filter which estimates the accelerometer moving bias and constant bias, as well as the velocity and position of the platform.

The six state Kalman filter model includes the following states:

$$x = \begin{bmatrix} velocity_x \\ velocity_y \\ position_x \\ position_y \\ bias_{walking} \\ bias_{constant} \end{bmatrix} \quad (4.28)$$

where the state space matrices are,

$$A_{kal} = \begin{bmatrix} 0 & 0 & 0 & 0 & -g \cos(\vartheta) & -g \cos(\vartheta) \\ 0 & 0 & 0 & 0 & -g \sin(\vartheta) & -g \sin(\vartheta) \\ 1 & 0 & 0 & 0 & 0 & 0 \\ 0 & 1 & 0 & 0 & 0 & 0 \\ 0 & 0 & 0 & 0 & -1/\tau & 0 \\ 0 & 0 & 0 & 0 & 0 & 0 \end{bmatrix} \quad (4.29)$$

$$B_{kal} = \begin{bmatrix} g \cos(\vartheta) \\ g \sin(\vartheta) \\ 0 \\ 0 \\ 0 \\ 0 \end{bmatrix} \quad (4.30)$$

$$C_{kal_{GPS_{on}}} = \begin{bmatrix} 1 & 0 & 0 & 0 & 0 & 0 \\ 0 & 1 & 0 & 0 & 0 & 0 \\ 0 & 0 & 1 & 0 & 0 & 0 \\ 0 & 0 & 0 & 1 & 0 & 0 \end{bmatrix} \quad (4.31)$$

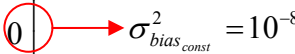
$$C_{kal_{GPS_{off}}} = \begin{bmatrix} 0 & 0 & 0 & 0 & 0 & 0 \\ 0 & 0 & 0 & 0 & 0 & 0 \\ 0 & 0 & 0 & 0 & 0 & 0 \\ 0 & 0 & 0 & 0 & 0 & 0 \end{bmatrix} \quad (4.32)$$

$$D_{kal} = \begin{bmatrix} 0 \\ 0 \\ 0 \\ 0 \end{bmatrix} \quad (4.33)$$

The noise covariance matrices for the system are defined as:

$$B_w = \begin{bmatrix} g \cos(\vartheta) & 0 & 0 \\ g \sin(\vartheta) & 0 & 0 \\ 0 & 0 & 0 \\ 0 & 0 & 0 \\ 0 & 1 & 0 \\ 0 & 0 & 1 \end{bmatrix} \quad (4.34)$$

$$Q_w = \begin{bmatrix} \frac{\sigma_{noise}^2}{\sqrt{f_s}} & 0 & 0 \\ 0 & \frac{2f_s \sigma_{bias_{moving}}^2}{\tau} & 0 \\ 0 & 0 & 0 \end{bmatrix} \quad (4.35)$$



$$R = \begin{bmatrix} \sigma_{GPS}^2 & 0 & 0 & 0 \\ 0 & \sigma_{GPS}^2 & 0 & 0 \\ 0 & 0 & \sigma_{GPS}^2 & 0 \\ 0 & 0 & 0 & \sigma_{GPS}^2 \end{bmatrix} \quad (4.36)$$

The utility of this six state model is similar to the three state model presented in section 4.4. This six state Kalman filter model is able to estimate two components in a bias. These components include a constant offset or mean that is not zero as well as a moving component.

4.7 Summary and Conclusion

A Kalman Filter was implemented which combined the GPS position, velocity and heading measurements with the inertial sensor measurements. The Kalman filter incorporated the sensor model presented in Chapter 2. It was shown that the coupling of the GPS measurements and the sensor model to calculate the position, velocity and heading from the combined GPS and IMU measurements resulted in new error bounds for position, velocity and heading. It was shown that the steady state error bounds were the same for both the two state Kalman filter and the three state Kalman filter when used to estimate heading. The two state Kalman filter provided an estimation of the rate gyros biases. However, the bias had to be either modeled as a random walk or a first order Markov process. Monte Carlo simulations were used to demonstrate the difficulty in choosing the model type. The three state Kalman filter provided an estimation of the rate gyros bias and was able to estimate both a constant component as well as a moving component of the actual sensor bias. Experimental data was used to validate the bias estimations in the three state Kalman filter. A five state model was laid out which estimates two bias components in an accelerometer. These components include a constant part and a moving part.

CHAPTER 5

INTEGRATION ERRORS IN A SIX DEGREE OF FREEDOM INERTIAL MEASUREMENT UNIT

5.1 Introduction

In this chapter the errors associated with the integration of three rate gyros and three accelerometers to calculate position, velocity and heading in a 3 dimensional setting are discussed. First, the model used to simulate the inertial measurement unit (IMU) will be laid out along with the integration method. The error growth of the position, velocity and heading calculation is then depicted using Monte Carlo simulations. Additionally, both a consumer grade and tactical grade inertial measurement unit will be compared with and without a gravity field in place.

5.2 Six Degree of Freedom Inertial Measurement Unit Model

In Chapter 2, a simple model for a rate gyro and an accelerometer were presented. This chapter will utilize these models to simulate an inertial measurement unit with six degrees of freedom. The degrees of freedom include three translational degrees of freedom (vertical, lateral, and longitudinal) and three rotational degrees of freedom (roll, pitch, and yaw). The following figures are a pictorial representation of these degrees of freedom.

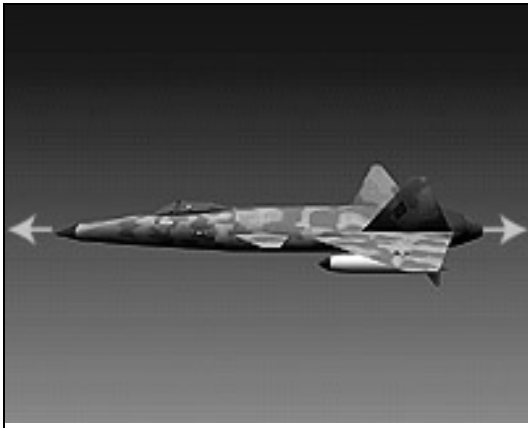


Figure 5.1a_Longitudinal (X)
(Motion Forward and Backward)

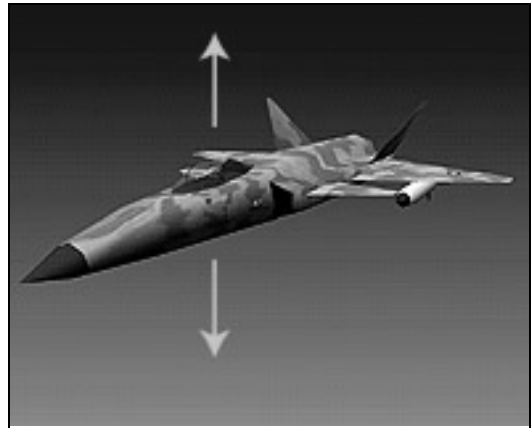


Figure 5.1b Vertical (Y)
(Motion Upward and Downward)

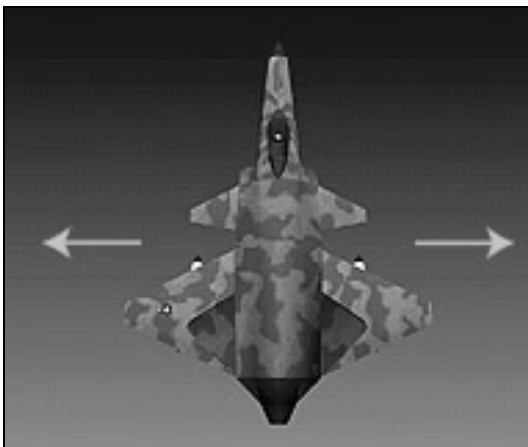


Figure 5.1c Lateral (Z)
(Motion Left and Right)

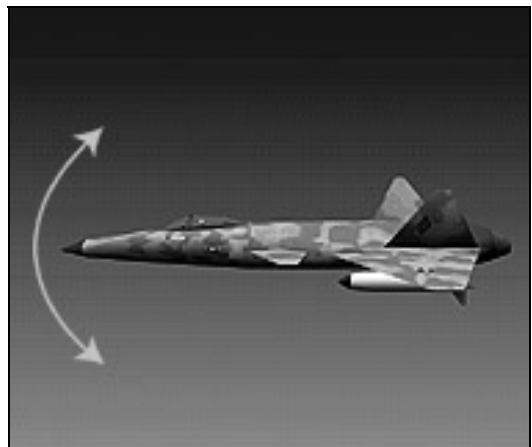


Figure 5.1d Pitch (θ)
(Nose Pitches Up or Down)

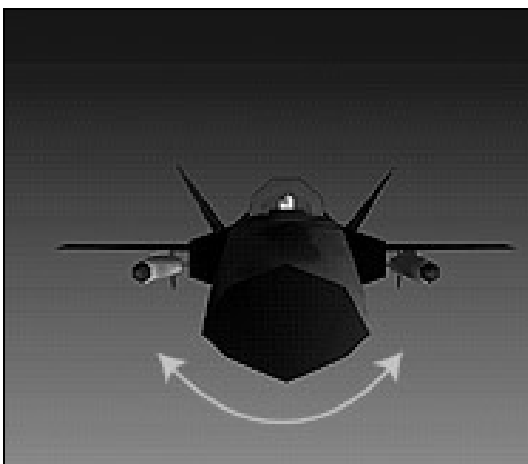


Figure 5.1e Roll (ϕ)
(Wings Roll Up or Down)

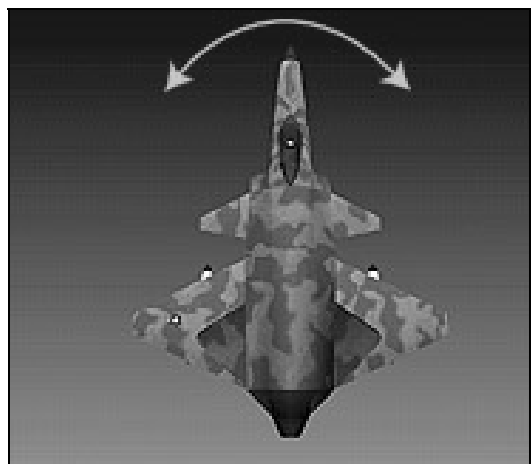


Figure 5.1e Yaw (ψ)
(Nose Moves from Side to Side)

Figure 5.1 Definition of the Six Degrees of Freedom

The vertical, lateral, and longitudinal accelerations will be modeled with three simple accelerometer models as was used in Chapter 2. The roll, pitch and yaw rates will also be modeled with the three simple rate gyro models from Chapter 2. These rate gyro triad model equations and accelerometer triad model equations for the entire simple six degree of freedom inertial measurement unit are shown below.

$$g_{\phi} = r_{\phi} + c_{\phi} + b_{\phi} + w_{gyro_{\phi}} \quad (5.1)$$

$$g_{\theta} = r_{\theta} + c_{\theta} + b_{\theta} + w_{gyro_{\theta}} \quad (5.2)$$

$$g_{\psi} = r_{\psi} + c_{\psi} + b_{\psi} + w_{gyro_{\psi}} \quad (5.3)$$

$$a_{\ddot{x}} = \ddot{x} + c_{\ddot{x}} + b_{\ddot{x}} + w_{accel_{\ddot{x}}} \quad (5.4)$$

$$a_{\ddot{y}} = \ddot{y} + c_{\ddot{y}} + b_{\ddot{y}} + w_{accel_{\ddot{y}}} \quad (5.5)$$

$$a_{\ddot{z}} = \ddot{z} + c_{\ddot{z}} + b_{\ddot{z}} + w_{accel_{\ddot{z}}} \quad (5.6)$$

The above equations contain the actual gyro measurements for roll rate (g_{ϕ}), pitch rate (g_{θ}), and yaw rate (g_{ψ}) as well as the actual roll rate (r_{ϕ}), the actual pitch rate (r_{θ}) and the actual yaw rate (r_{ψ}). Each rate gyro contains a constant bias term c and a moving bias term b . The moving bias in each rate gyro is modeled as a first order Markov process with the following variances.

$$E[b_{\phi}^2] = \sigma_{gyro_{bias_{\phi}}}^2 \quad (5.7)$$

$$E[b_g^2] = \sigma_{gyro\ bias_g}^2 \quad (5.8)$$

$$E[b_\psi^2] = \sigma_{gyro\ bias_\psi}^2 \quad (5.9)$$

Each rate gyro also contains a wide band noise term w_{gyro} . The variances and means of the wide band noise term for each of the rate gyros are defined as follows.

$$E[w_{gyro\ \phi}^2] = \frac{\sigma_{gyro\ \phi}^2}{f_s} \quad (5.10)$$

$$E[w_{gyro\ \phi}] = 0 \quad (5.11)$$

$$E[w_{gyro\ g}^2] = \frac{\sigma_{gyro\ g}^2}{f_s} \quad (5.12)$$

$$E[w_{gyro\ g}] = 0 \quad (5.13)$$

$$E[w_{gyro\ \psi}^2] = \frac{\sigma_{gyro\ \psi}^2}{f_s} \quad (5.14)$$

$$E[w_{gyro\ \psi}] = 0 \quad (5.15)$$

The above equations contain the longitudinal acceleration measurement ($a_{\ddot{x}}$), the vertical acceleration measurement ($a_{\ddot{y}}$), and the lateral acceleration measurement ($a_{\ddot{z}}$). They also contain the actual longitudinal acceleration (\ddot{x}), the actual vertical acceleration (\ddot{y}) and the actual lateral acceleration (\ddot{z}). Each accelerometer contains a constant bias

term c and a moving bias term b . The moving bias in each accelerometer is modeled as a first order Markov process with the following variances.

$$E[b_{\ddot{x}}^2] = \sigma_{accel_{bias\ddot{x}}}^2 \quad (5.16)$$

$$E[b_{\ddot{y}}^2] = \sigma_{accel_{bias\ddot{y}}}^2 \quad (5.17)$$

$$E[b_{\ddot{z}}^2] = \sigma_{accel_{bias\ddot{z}}}^2 \quad (5.18)$$

Each accelerometer also contains a wide band noise term w_{accel} . The variances and means of the wide band noise term for each of the accelerometers are defined as follows.

$$E[w_{accel\ddot{x}}^2] = \frac{\sigma_{accel\ddot{x}}^2}{f_s} \quad (5.19)$$

$$E[w_{accel\ddot{x}}] = 0 \quad (5.20)$$

$$E[w_{accel\ddot{y}}^2] = \frac{\sigma_{accel\ddot{y}}^2}{f_s} \quad (5.21)$$

$$E[w_{accel\ddot{y}}] = 0 \quad (5.22)$$

$$E[w_{accel\ddot{z}}^2] = \frac{\sigma_{accel\ddot{z}}^2}{f_s} \quad (5.23)$$

$$E[w_{accel\ddot{z}}] = 0 \quad (5.24)$$

5.3 Six Degree of Freedom Inertial Measurement Unit Integration

To determine the position of a six degree of freedom IMU the roll, pitch, and yaw of the platform must first be calculated. This is accomplished by numerical integrating the rate gyro measurement. The method chosen to do this is the Runge-Kutta order four integration routine. This method is laid out below for a State Space format

The state space matrices for calculating heading of a six DoF IMU are:

$$A = \begin{bmatrix} 0 & 0 & 0 \\ 0 & 0 & 0 \\ 0 & 0 & 0 \end{bmatrix} \quad (5.25)$$

$$B = \begin{bmatrix} 1 & 0 & 0 \\ 0 & 1 & 0 \\ 0 & 0 & 1 \end{bmatrix} \quad (5.26)$$

$$f_{heading} = A \begin{bmatrix} \phi \\ \mathcal{G} \\ \psi \end{bmatrix} + B \begin{bmatrix} \dot{\phi} \\ \dot{\mathcal{G}} \\ \dot{\psi} \end{bmatrix} \quad (5.27)$$

The Runge-Kutta order four procedure for integrating the above state space equations is defined in the following equations.

$$[\phi_{i+1} \quad \mathcal{G}_{i+1} \quad \psi_{i+1}]^T = [\phi_i \quad \mathcal{G}_i \quad \psi_i]^T + (k_1 + 2k_2 + 2k_3 + k_4)/6 \quad (5.28)$$

where

$$\begin{aligned}
k_1 &= T_s f_{heading} \left([\phi_i \ \mathcal{G}_i \ \psi_i]^T, [\dot{\phi}_i \ \dot{\mathcal{G}}_i \ \dot{\psi}_i]^T \right) \\
k_2 &= T_s f_{heading} \left([\phi_i \ \mathcal{G}_i \ \psi_i]^T + k_1/2, [\dot{\phi}_i \ \dot{\mathcal{G}}_i \ \dot{\psi}_i]^T \right) \\
k_3 &= T_s f_{heading} \left([\phi_i \ \mathcal{G}_i \ \psi_i]^T + k_2/2, [\dot{\phi}_i \ \dot{\mathcal{G}}_i \ \dot{\psi}_i]^T \right) \\
k_4 &= T_s f_{heading} \left([\phi_i \ \mathcal{G}_i \ \psi_i]^T + k_3, [\dot{\phi}_i \ \dot{\mathcal{G}}_i \ \dot{\psi}_i]^T \right)
\end{aligned} \tag{5.29}$$

The initial conditions in this thesis were always set to zero such that:

$$\begin{bmatrix} \phi_0 \\ \mathcal{G}_0 \\ \psi_0 \end{bmatrix} = \begin{bmatrix} 0 \\ 0 \\ 0 \end{bmatrix} \tag{5.30}$$

The initialization of the roll angle (ϕ), pitch angle (\mathcal{G}), and yaw angle (ψ) all to zero corresponds to an alignment where the x-axis is pointing due North, the y-axis is pointing straight Up, and the z-axis is pointing due East.

After the roll, pitch, and yaw angles of the platform are calculated, the position and velocity of the platform must be calculated by integrating the accelerometer measurements. The Runge-Kutta method was also used in a state space format:

The state space matrices for calculating position of a six DoF IMU are:

$$A = \begin{bmatrix} 0 & 0 & 0 & 0 & 0 & 0 \\ 0 & 0 & 0 & 0 & 0 & 0 \\ 0 & 0 & 0 & 0 & 0 & 0 \\ 1 & 0 & 0 & 0 & 0 & 0 \\ 0 & 1 & 0 & 0 & 0 & 0 \\ 0 & 0 & 1 & 0 & 0 & 0 \end{bmatrix} \tag{5.31}$$

$$B = \begin{bmatrix} [R_{ENU}] \\ 0 & 0 & 0 \\ 0 & 0 & 0 \\ 0 & 0 & 0 \end{bmatrix} \quad (5.32)$$

Where R_{ENU} is a transformation matrix from the x-y-z body frame to the ENU coordinate frame as defined below.

$$[R_{ENU}] = R_x^{-1} R_y^{-1} R_z^{-1} \quad (5.33)$$

The individual body coordinate transformation matrices (R_x, R_y, R_z) are:

$$R_x = \begin{bmatrix} 1 & 0 & 0 \\ 0 & \cos(\phi) & \sin(\phi) \\ 0 & -\sin(\phi) & \cos(\phi) \end{bmatrix} \quad (5.34)$$

$$R_y = \begin{bmatrix} \cos(\psi) & 0 & -\sin(\psi) \\ 0 & 1 & 0 \\ \sin(\psi) & 0 & \cos(\psi) \end{bmatrix} \quad (5.35)$$

$$R_z = \begin{bmatrix} \cos(\vartheta) & \sin(\vartheta) & 0 \\ -\sin(\vartheta) & \cos(\vartheta) & 0 \\ 0 & 0 & 1 \end{bmatrix} \quad (5.36)$$

The state vector derivative ($f_{position}$) can then be defined as shown below.

$$f_{position} = A \begin{bmatrix} \dot{x} \\ \dot{y} \\ \dot{z} \\ x \\ y \\ z \end{bmatrix} + B \begin{bmatrix} \ddot{x} \\ \ddot{y} \\ \ddot{z} \\ 0 \\ 0 \\ 0 \end{bmatrix} + G \begin{bmatrix} 0 \\ -1 \\ 0 \\ 0 \\ 0 \\ 0 \end{bmatrix} \quad (5.37)$$

Where G is the gravity field ($9.81 m/s^2$)

The Runge-Kutta order four procedure for integrating the above state space equations is shown below.

$$\begin{bmatrix} \dot{x}_{i+1} \\ \dot{y}_{i+1} \\ \dot{z}_{i+1} \\ x_{i+1} \\ y_{i+1} \\ z_{i+1} \end{bmatrix} = \begin{bmatrix} \dot{x}_i \\ \dot{y}_i \\ \dot{z}_i \\ x_i \\ y_i \\ z_i \end{bmatrix} + (k_1 + 2k_2 + 2k_3 + k_4)/6 \quad (5.38)$$

where:

$$\begin{aligned} k_1 &= T_s f_{\text{positon}} \left([\dot{x}_i \ \dot{y}_i \ \dot{z}_i \ x_i \ y_i \ z_i]^T, [\phi_i \ \vartheta_i \ \psi_i]^T, [\ddot{x}_i \ \ddot{y}_i \ \ddot{z}_i]^T \right) \\ k_2 &= T_s f_{\text{positon}} \left([\dot{x}_i \ \dot{y}_i \ \dot{z}_i \ x_i \ y_i \ z_i]^T + k_1/2, [\phi_i \ \vartheta_i \ \psi_i]^T, [\ddot{x}_i \ \ddot{y}_i \ \ddot{z}_i]^T \right) \\ k_3 &= T_s f_{\text{positon}} \left([\dot{x}_i \ \dot{y}_i \ \dot{z}_i \ x_i \ y_i \ z_i]^T + k_2/2, [\phi_i \ \vartheta_i \ \psi_i]^T, [\ddot{x}_i \ \ddot{y}_i \ \ddot{z}_i]^T \right) \\ k_4 &= T_s f_{\text{positon}} \left([\dot{x}_i \ \dot{y}_i \ \dot{z}_i \ x_i \ y_i \ z_i]^T + k_3, [\phi_i \ \vartheta_i \ \psi_i]^T, [\ddot{x}_i \ \ddot{y}_i \ \ddot{z}_i]^T \right) \end{aligned} \quad (5.39)$$

Again the initial conditions for the system are set to zero.

$$\begin{bmatrix} \dot{x}_0 \\ \dot{y}_0 \\ \dot{z}_0 \\ x_0 \\ y_0 \\ z_0 \end{bmatrix} = \begin{bmatrix} 0 \\ 0 \\ 0 \\ 0 \\ 0 \\ 0 \end{bmatrix} \quad (5.40)$$

The initialization of the states vector to zero is convenient for this analysis. However, if this were done in practice, the initial longitude, latitude and altitude of the vehicle platform would need to be recorded in order to properly propagate the vehicle motion.

In the next sections, a six degree of freedom inertial measurement unit is simulated to study how the heading, velocity, and position errors grow over time. A tactical and consumer grade IMU is used. The simulation used the model provided in Equations (5.1-5.6), which include a Markov bias, wide band noise and a constant bias. The constant bias term was removed in order to focus on the errors generated from the combination of a Markov bias and wide band noise. The simulations were run with a gravity field in place and with it removed. This was done to emphasize the effect gravity has on the navigation capabilities of an IMU.

5.4 Six Degree of Freedom IMU Integration Heading Errors

Figure 5.2 is a plot of the roll, pitch, and yaw angle errors produced when a tactical grade IMU is integrated. The angles shown are between the body frame and the ENU coordinate frame. The Monte Carlo simulation was run with a gravity field and without a gravity field. As seen in the plot the introduction of gravity does not effect the heading calculations for a tactical grade IMU. This is due to the fact that the gravity field is only seen by the accelerometers. Since the heading calculation only uses the measurements from the three rate gyros the introduction of a gravity field will never affect there error growths.

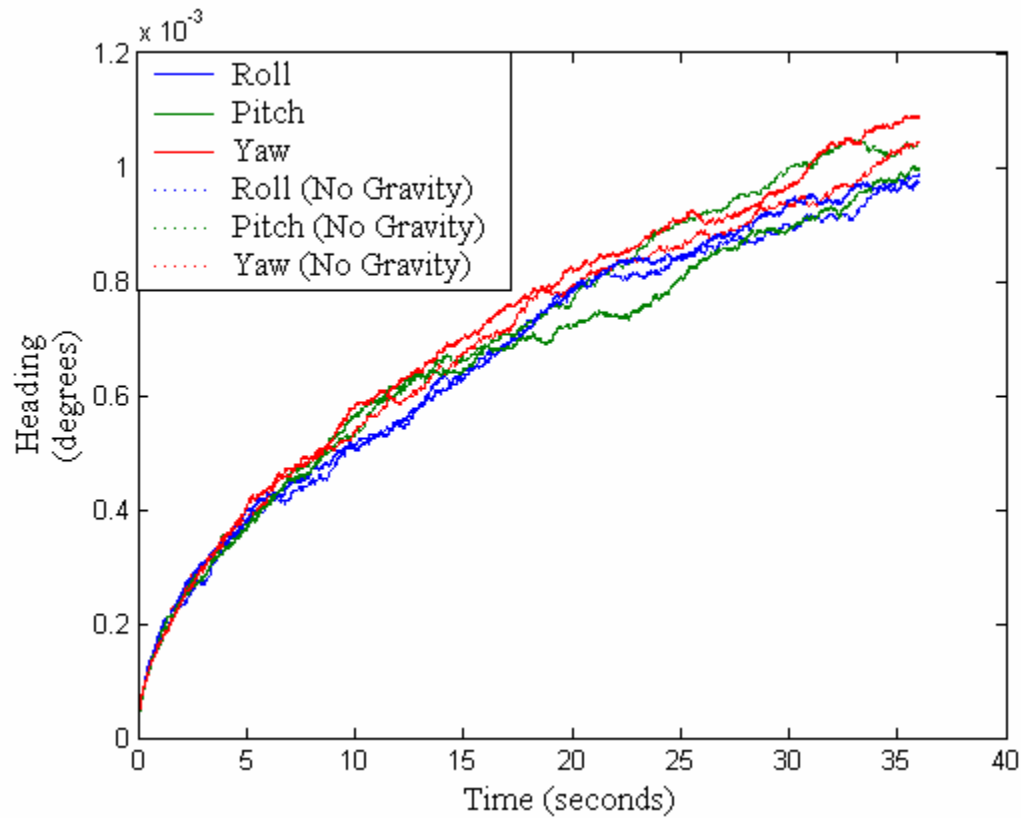


Figure 5.2 Heading Error in a Six DoF Tactical Grade IMU

Figure 5.3 is a plot of the roll, pitch, and yaw angle errors produced when a consumer grade IMU is integrated. The angles shown are between the body frame and the NEU coordinate frame. Again, the Monte Carlo simulation was run with and without a gravity field. As seen in the figure the introduction of gravity does not effect the heading calculations for a consumer grade IMU due to the reasons mentioned above.

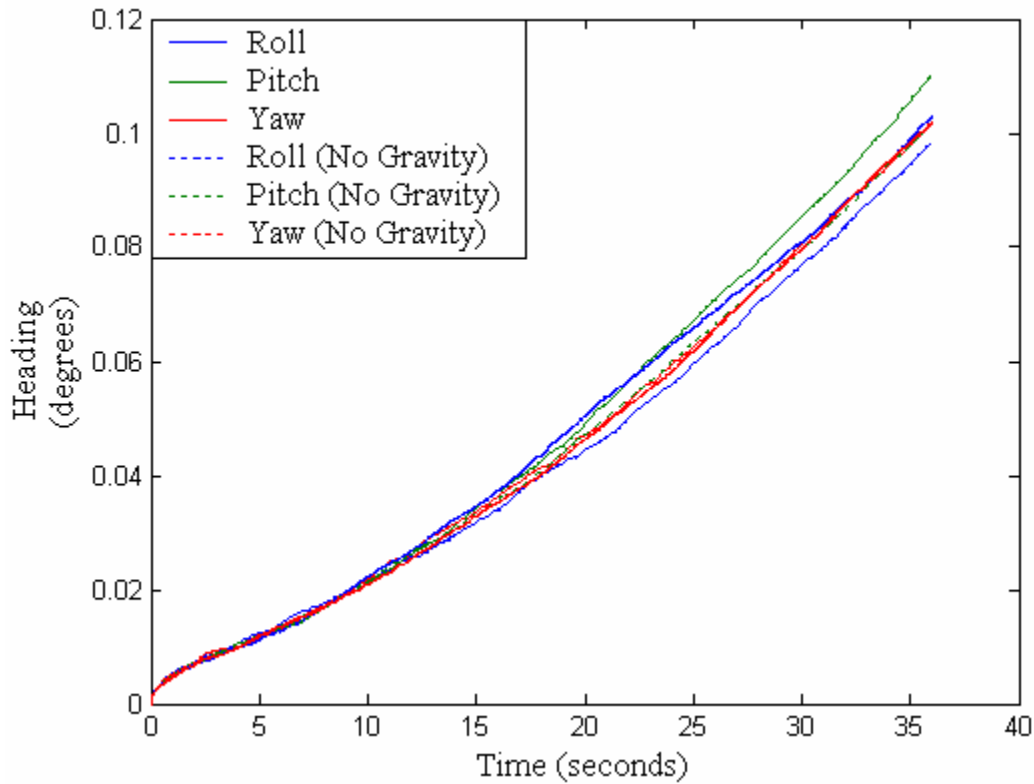


Figure 5.3 Heading Error in a Six DoF Consumer Grade IMU

5.5 Six Dof Inertial Measurement Unit Velocity Errors

Figure 5.4 is a plot of the longitudinal, lateral, and vertical velocity errors produced when a tactical grade IMU is integrated. The velocities shown are in the North East Up coordinate frame. The Monte Carlo simulation was run with and without a gravity field. As seen in the figure, the introduction of a gravity field causes the longitudinal and lateral velocity errors to grow at a rate slightly higher than the vertical velocity errors.

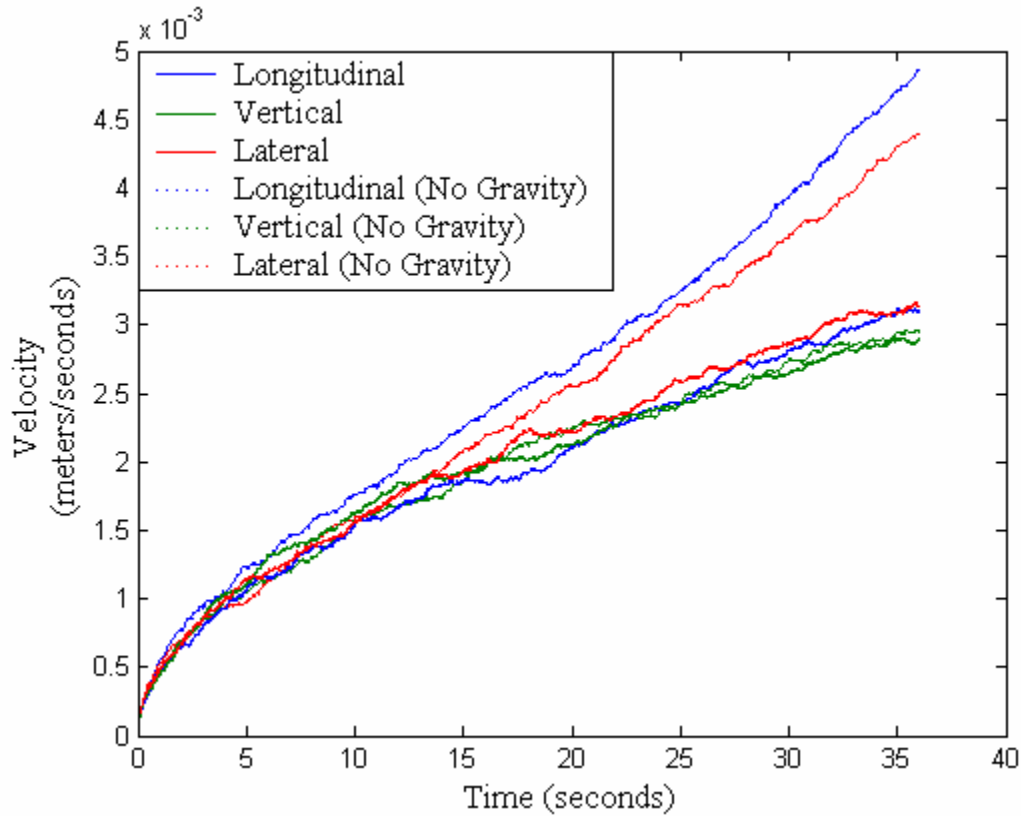


Figure 5.4 Velocity Errors in a Six DoF Tactical Grade IMU

Figure 5.5 is a plot of the longitudinal, lateral, and vertical velocity errors produced when a consumer grade IMU is integrated. The velocities shown are in the North East Up coordinate frame. The Monte Carlo simulation was run again and without a gravity field. As seen in the figure, the introduction of a gravity field causes the longitudinal and lateral velocity errors to grow at a much faster rate than the vertical velocity errors.

From an observational stand point, it is important to notice that the introduction of a gravity field causes the velocity error bounds to change. The magnitude of the change is dependent on the grade IMU.

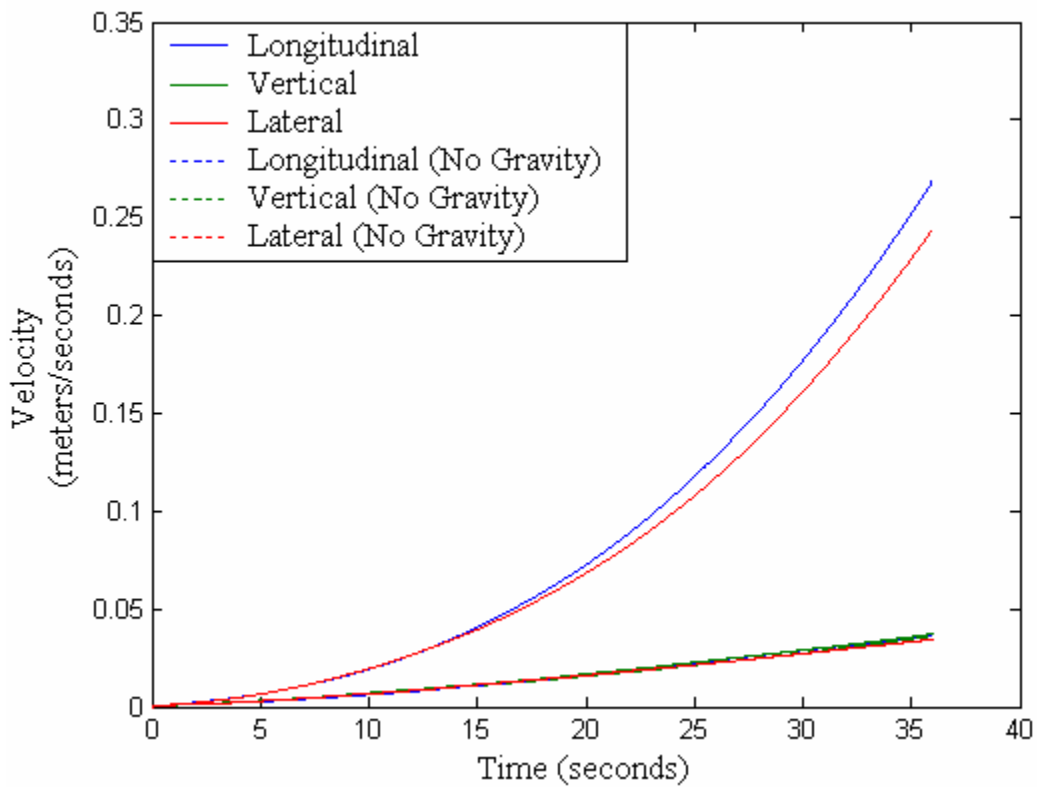


Figure 5.5 Velocity Error in a Six DoF Consumer Grade IMU

5.6 Six Dof Inertial Measurement Unit Position Errors

Figure 5.6 is a plot of the longitudinal, lateral and vertical position errors produced when a tactical grade IMU is integrated. The positions shown are in the North East Up coordinate frame. In the previous figures, it was shown that the introduction of a gravity field causes the longitudinal and lateral velocity errors to grow at a slightly faster rate than the vertical velocity errors. It should be expected that these increased errors will

induce similar errors in the longitudinal and lateral positions. This can be seen in Figure 5.6.

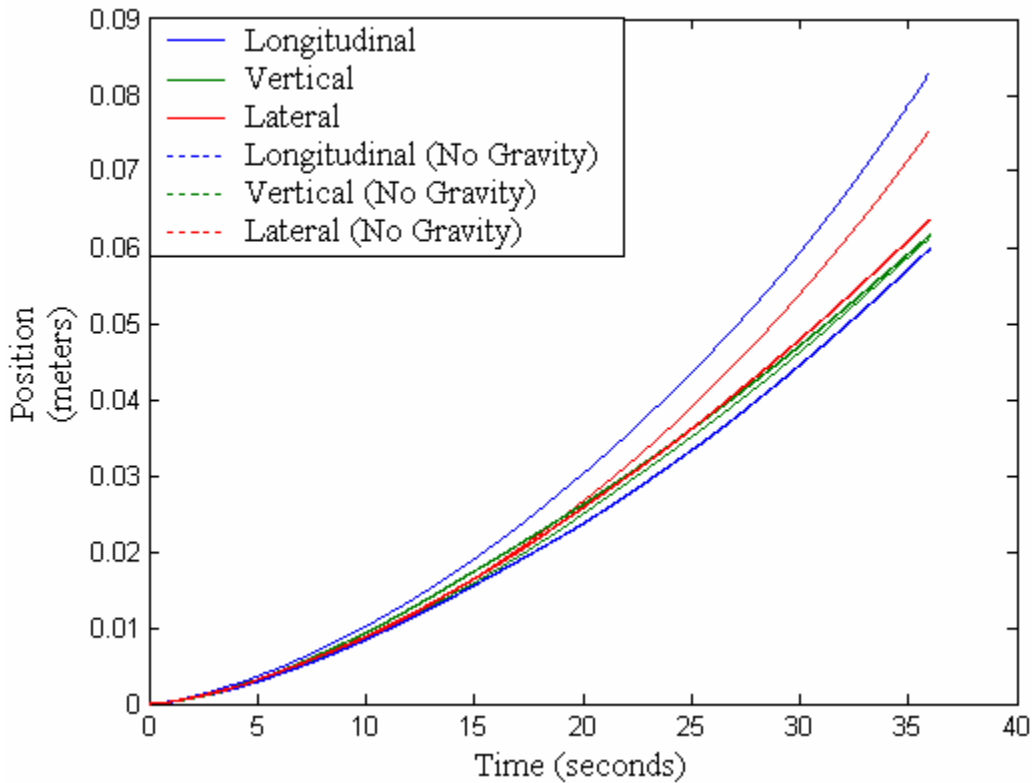


Figure 5.6 Position Error in a Six DoF Tactical Grade IMU

Figure 5.7 is a plot of the longitudinal, lateral, and vertical position errors produced when a consumer grade IMU is integrated. The positions shown are in the North East Up coordinate frame. In the previous figures it was shown that the introduction of a gravity field causes the longitudinal and lateral velocity errors to grow at a much faster rate than the vertical velocity errors. It should be expected that the

increased errors will induce similar errors in the longitudinal and lateral positions. This can be seen in Figure 5.7.

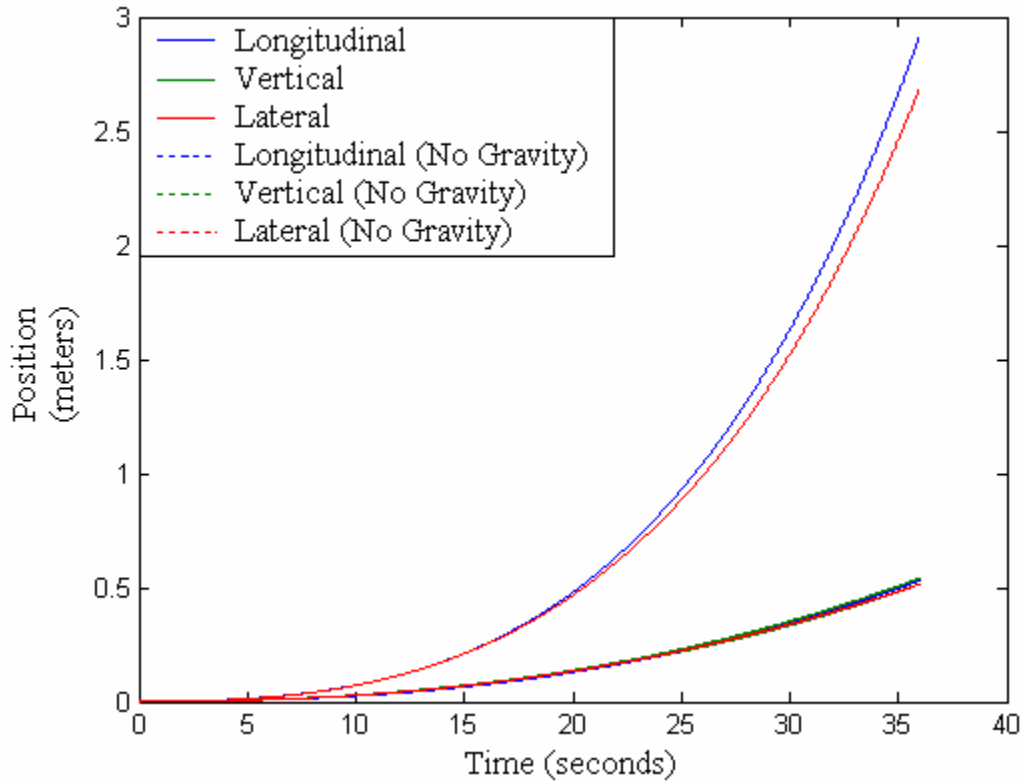


Figure 5.7 Position Error in a Six DoF Consumer Grade IMU

5.7 Summary and Conclusion

This chapter discussed the errors associated with the integration of three rate gyros and three accelerometers to calculate position, velocity and heading in a 3 dimensional setting. First, the IMU model was laid out along with the Runge-Kutta integration method. Then the error growth of the position, velocity, and heading

calculations were depicted using Monte Carlo simulations. Both a consumer grade and tactical grade inertial measurement unit were simulated and the effects of a gravity field were pictorially shown for each.

CHAPTER 6

ADVANCED SENSOR MODELING

6.1 Introduction

This chapter will lay out a more advanced six degree of freedom inertial sensor model for the rate gyros and accelerometers in the inertial measurement unit. The model presented in this chapter will introduce a variety of new terms. Each term is an error source which can be seen in the inertial sensors measurements. The advanced terms in the accelerometer model will include misalignment, nonorthogonality, scale factor, scale factor asymmetry, and nonlinearity. The advanced terms in the rate gyro model will include misalignment, nonorthogonality and scale factor. Each of these terms will be defined and pictorially presented. Finally, this chapter will define the errors due to incorrect initial conditions given to the integration routine. These errors are commonly known as the inertial measurement unit's initialization errors.

6.2 The Inertial Measurement Unit Accelerometer Triad Error Model

The inertial measurement accelerometer triad error model [Grewal], which contains a scale factor error, an asymmetric scale factor error, a nonlinear scale factor

error, misalignment errors, nonorthogonality errors and all the error terms presented in Chapter 5 is given as,

$$a_{\ddot{x}} = (1 + SF_x)\ddot{x} + SFA_x|\ddot{x}| + SFN_x\ddot{x}^2 + \sin(\Delta_{Az} + \delta_{Az})\ddot{y} + \sin(\Delta_{Ay} - \delta_{Ay})\ddot{z} + c_{\ddot{x}} + b_{\ddot{x}} + w_{accel_x} \quad (6.1)$$

$$a_{\ddot{y}} = (1 + SF_y)\ddot{y} + SFA_y|\ddot{y}| + SFN_y\ddot{y}^2 + \sin(\Delta_{Az} - \delta_{Az})\ddot{x} + \sin(\Delta_{Ax} + \delta_{Ax})\ddot{z} + c_{\ddot{y}} + b_{\ddot{y}} + w_{accel_y} \quad (6.2)$$

$$a_{\ddot{z}} = (1 + SF_z)\ddot{z} + SFA_z|\ddot{z}| + SFN_z\ddot{z}^2 + \sin(\Delta_{Ay} + \delta_{Ay})\ddot{x} + \sin(\Delta_{Ax} - \delta_{Ax})\ddot{y} + c_{\ddot{z}} + b_{\ddot{z}} + w_{accel_z} \quad (6.3)$$

where,

$a_{\ddot{x}}$, $a_{\ddot{y}}$ and $a_{\ddot{z}}$ are the measured accelerations,

\ddot{x} , \ddot{y} and \ddot{z} are the true accelerations,

and

$|\ddot{x}|$, $|\ddot{y}|$ and $|\ddot{z}|$ are the absolute value of the true accelerations.

The definitions of the error terms for the accelerometer are provided in Table 6.1.

The wide band sensor noise, w_{accel} , is assumed to be normally distributed with a zero mean and have the following sampled covariance:

$$E[w_{accel}^2] = \frac{\sigma_{accel}^2}{f_s} \quad (6.4)$$

The gyros walking bias, b , will be modeled as a first order Markov Process with defined statistics which account for its drift and are shown below:

$$b \subset [0, \sigma_{accelbias}^2] \quad (6.5)$$

$$\dot{b} = -\frac{1}{\tau}b + w_{gyro\,bias} \quad (6.6)$$

6.3 The Inertial Measurement Unit Rate Gyro Triad Error Model

The inertial measurement rate gyro triad error model [9], which contains scale factor errors, misalignment errors, nonorthogonality errors and all the error terms presented in Chapter 5 is given as,

$$g_\phi = (1 + SF_\phi)\dot{\phi} + \sin(\Delta_{Gy} + \delta_{Gy})\dot{\mathcal{G}} + \sin(\Delta_{Gz} - \delta_{Gz})\dot{\psi} + c_\phi + b_\phi + w_{gyro\,\phi} \quad (6.7)$$

$$g_g = (1 + SF_g)\dot{\mathcal{G}} + \sin(\Delta_{Gy} + \delta_{Gy})\dot{\phi} + \sin(\Delta_{Gx} - \delta_{Gx})\dot{\psi} + c_g + b_g + w_{gyro\,g} \quad (6.8)$$

$$g_\psi = (1 + SF_\psi)\dot{\psi} + \sin(\Delta_{Gz} - \delta_{Gz})\dot{\phi} + \sin(\Delta_{Gx} + \delta_{Gx})\dot{\mathcal{G}} + c_\psi + b_\psi + w_{gyro\,\psi} \quad (6.9)$$

where,

g_ϕ , g_g and g_ψ are the measured rotation rates,

$\dot{\phi}$, $\dot{\mathcal{G}}$ and $\dot{\psi}$ are the true rotation rates,

and

$|\dot{\phi}|$, $|\dot{\mathcal{G}}|$ and $|\dot{\psi}|$ are the absolute value of the true accelerations.

The wide band sensor noise, w_{gyro} , is assumed to be normally distributed with a zero mean and have the following sampled covariance:

$$E[w_{gyro}^2] = \frac{\sigma_{gyro}^2}{f_s} \quad (6.10)$$

The gyros walking bias, b , will be modeled as a first order Markov Process with defined statistics which account for its drift and are shown below:

$$b \subset [0, \sigma_{gyro\,bias}^2] \quad (6.11)$$

$$\dot{b} = -\frac{1}{\tau}b + w_{gyro\,bias} \quad (6.12)$$

A list of all of the error terms used in the triad accelerometer model (6.1-6.3) and the triad rate gyro model (6.7-6.9) are given below in Table 6.1

Table 6.1 Advanced IMU Error Parameters

Error Parameter	Symbol	Units
Roll Gyro Wide Band Noise Variance	$\sigma_{gyro\,\phi}^2$	$(\circ/\text{sec})^2$
Pitch Gyro Wide Band Noise Variance	$\sigma_{gyro\,\phi}^2$	$(\circ/\text{sec})^2$
Yaw Gyro Wide Band Noise Variance	$\sigma_{gyro\,\psi}^2$	$(\circ/\text{sec})^2$
Roll Gyro Constant Offset	c_ϕ	\circ/sec
Pitch Gyro Constant Offset	c_g	\circ/sec
Yaw Gyro Constant Offset	c_ψ	\circ/sec
Roll Gyro Bias Variance	$\sigma_{gyro\,bias\,\phi}^2$	$(\circ/\text{sec})^2$
Pitch Gyro Bias Variance	$\sigma_{gyro\,bias\,g}^2$	$(\circ/\text{sec})^2$
Yaw Gyro Bias Variance	$\sigma_{gyro\,bias\,\psi}^2$	$(\circ/\text{sec})^2$
Roll Gyro Bias Time Constant	τ_ϕ	sec
Pitch Gyro Bias Time Constant	τ_g	sec
Yaw Gyro Bias Time Constant	τ_ψ	sec
Roll Gyro Scale Factor Error	SF_ϕ	ppm
Pitch Gyro Scale Factor Error	SF_g	ppm
Yaw Gyro Scale Factor Error	SF_ψ	ppm

Gyro Triad Misalignment about X	δ_{Gx}	μrad
Gyro Triad Misalignment about Y	δ_{Gy}	μrad
Gyro Triad Misalignment about Z	δ_{Gz}	μrad
Gyro Triad Nonorthogonality about X	Δ_{Gx}	μrad
Gyro Triad Nonorthogonality about Y	Δ_{Gy}	μrad
Gyro Triad Nonorthogonality about Z	Δ_{Gz}	μrad
Longitudinal Accelerometer Wide Band Noise Variance	$\sigma_{accel\ x}^2$	g^2
Vertical Accelerometer Wide Band Noise Variance	$\sigma_{accel\ y}^2$	g^2
Lateral Accelerometer Wide Band Noise Variance	$\sigma_{accel\ z}^2$	g^2
Longitudinal Accelerometer Constant Offset	$c_{\ddot{x}}$	g
Vertical Accelerometer Constant Offset	$c_{\ddot{y}}$	g
Lateral Accelerometer Constant Offset	$c_{\ddot{z}}$	g
Longitudinal Accelerometer Bias Variance	$\sigma_{accel\ bias\ \phi}^2$	g^2
Vertical Accelerometer Bias Variance	$\sigma_{accel\ bias\ \theta}^2$	g^2
Lateral Accelerometer Bias Variance	$\sigma_{accel\ bias\ \psi}^2$	g^2
Longitudinal Accelerometer Bias Time Constant	τ_x	sec
Vertical Accelerometer Bias Time Constant	τ_y	sec
Lateral Accelerometer Bias Time Constant	τ_z	sec
Longitudinal Accelerometer Scale Factor Error	SF_x	ppm
Vertical Accelerometer Scale Factor Error	SF_y	ppm
Lateral Accelerometer Scale Factor Error	SF_z	ppm
Longitudinal Accelerometer Scale Factor Asymmetry	SFA_x	ppm
Vertical Accelerometer Scale Factor Asymmetry	SFA_y	ppm
Lateral Accelerometer Scale Factor Asymmetry	SFA_z	ppm
Longitudinal Accelerometer Scale Factor Nonlinearity	SFN_x	ppm
Vertical Accelerometer Scale Factor Nonlinearity	SFN_y	ppm
Lateral Accelerometer Scale Factor Nonlinearity	SFN_z	ppm
Accelerometer Triad Misalignment about X	δ_{Ax}	μrad
Accelerometer Triad Misalignment about Y	δ_{Ay}	μrad
Accelerometer Triad Misalignment about Z	δ_{Az}	μrad
Accelerometer Triad Nonorthogonality about X	Δ_{Ax}	μrad
Accelerometer Triad Nonorthogonality about Y	Δ_{Ay}	μrad
Accelerometer Triad Nonorthogonality about Z	Δ_{Az}	μrad

6.4 Model Error Parameter Descriptions

Figure 6.1 illustrates the individual input/output error types found in the advanced sensor model. Figure 6.1a, 6.1b and 6.1c are the graphical representation of scale factor, an offset bias and asymmetry, respectively. Figure 6.1d is the graphical representations of nonlinearity.

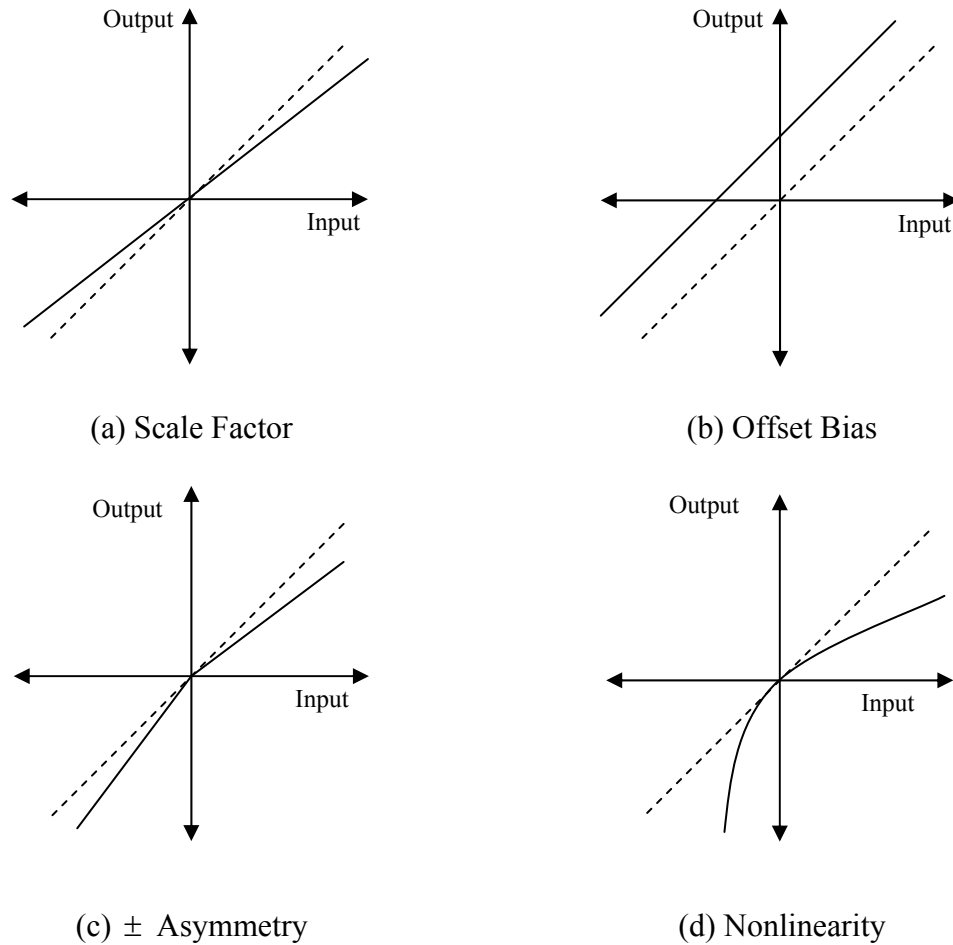


Figure 6.1 Inertial Measurement Unit Input/Output Error Types

Figure 6.2 illustrates the individual input axis misalignments. The large arrows in the figure represent the nominal input axis directions (labeled X, Y and Z). The smaller arrows (labeled m_{ij}) represent the directions of scale factor deviations when $i = j$ and axis misalignment when $i \neq j$.

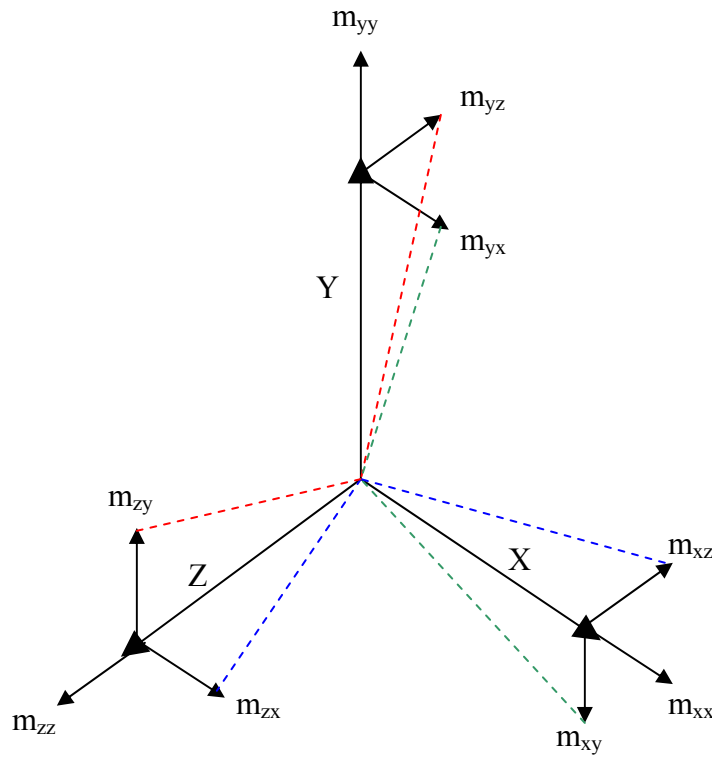


Figure 6.2 Inertial Measurement Unit Triad Misalignment

The following equations can be used to obtain the angular misalignment about a particular axis.

$$\delta_x = \arcsin\left(\frac{m_{yz}}{Y}\right) = \arcsin\left(\frac{m_{zy}}{Z}\right) \quad (6.13)$$

$$\delta_y = \arcsin\left(\frac{m_{xz}}{X}\right) = \arcsin\left(\frac{m_{zx}}{Z}\right) \quad (6.14)$$

$$\delta_z = \arcsin\left(\frac{m_{xy}}{X}\right) = \arcsin\left(\frac{m_{yx}}{Y}\right) \quad (6.15)$$

Figure 6.3 illustrates the individual input axis nonorthogonality. The large arrows in the figure represent the nominal input axis directions (labeled X, Y and Z). The smaller arrows (labeled m_{ij}) represent the directions of scale factor deviations when $i = j$ and axis nonorthogonality when $i \neq j$.

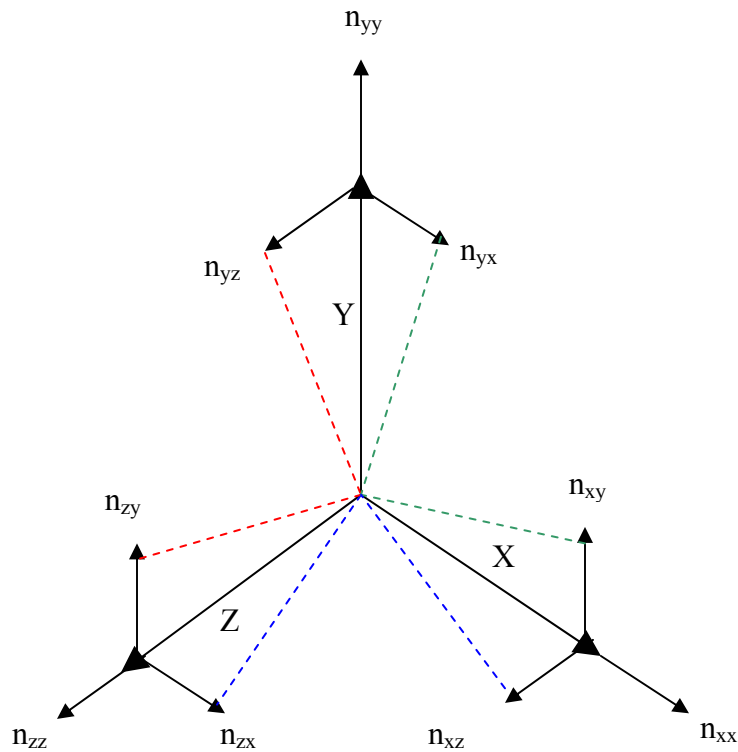


Figure 6.3 Inertial Measurement Unit Triad Nonorthogonality

The following equations can be used to obtain the angular nonorthogonality about a particular axis.

$$\Delta_x = \arcsin\left(\frac{n_{yz}}{Y}\right) = \arcsin\left(\frac{n_{zy}}{Z}\right) \quad (6.13)$$

$$\Delta_y = \arcsin\left(\frac{n_{xz}}{X}\right) = \arcsin\left(\frac{n_{zx}}{Z}\right) \quad (6.14)$$

$$\Delta_z = \arcsin\left(\frac{n_{zy}}{X}\right) = \arcsin\left(\frac{n_{yx}}{Y}\right) \quad (6.15)$$

6.5 Inertial Measurement Unit Initialization Errors

Before navigation can begin, the initial condition of the states must be given to the integration routine. The mean error of the calculated initial condition for each of the states are the initialization errors. In the previous chapter, the position of the body frame was represented in terms of the North-East-Up coordinate frame. This chapter will continue with that transformation. The initial attitude and position of the body frame will be input into the integration procedure. As the body frame moves, the position will then be calculated in terms of the NEU coordinate frame. The accuracies of the initial attitude and position measurement for the body frame are the initialization errors of the inertial measurement unit. Each degree of freedom will contain an initialization error, which are defined in Table 6.2 below.

Table 6.2 IMU Initialization Error Parameters

Error Parameter	Symbol	Units
North Position Error @ Beginning of Navigation	ρ_N	Degrees
East Position Error @ Beginning of Navigation	ρ_E	Degrees
Up Position Error @ Beginning of Navigation	ρ_U	Degrees
Roll Error @ Beginning of Navigation	ϕ_{error}	Meters
Pitch Error @ Beginning of Navigation	\mathcal{G}_{error}	Meters
Yaw Error @ Beginning of Navigation	ψ_{error}	Meters

Figure 6.4 shows the initialization vectors for a body coordinate frame. The perceived origin of the body frame is located at point $O = (N_0, E_0, U_0)$, The perceived heading of the body frame is $(\phi_0, \mathcal{G}_0, \psi_0)$. From Figure 6.4 the initialization errors can be defined as follows:

$$\rho_N = i_{xx} \quad (6.16)$$

$$\rho_E = i_{yy} \quad (6.17)$$

$$\rho_U = i_{zz} \quad (6.18)$$

$$\phi_{error} = \arcsin\left(\frac{i_{yz}}{Y}\right) = \arcsin\left(\frac{i_{zy}}{Z}\right) \quad (6.19)$$

$$\mathcal{G}_{error} = \arcsin\left(\frac{i_{yx}}{Y}\right) = \arcsin\left(\frac{i_{xy}}{X}\right) \quad (6.20)$$

$$\psi_{error} = \arcsin\left(\frac{i_{xz}}{X}\right) = \arcsin\left(\frac{i_{zx}}{Z}\right) \quad (6.21)$$

The actual origin of the body frame can be found with the following equations.

$$O_{actual} = (N_0 + \rho_N, E_0 + \rho_E, U_0 + \rho_U) \quad (6.22)$$

$$Heading_{actual} = (\phi_0 + \phi_{error}, \mathcal{G}_0 + \mathcal{G}_{error}, \psi_0 + \psi_{error}) \quad (6.23)$$

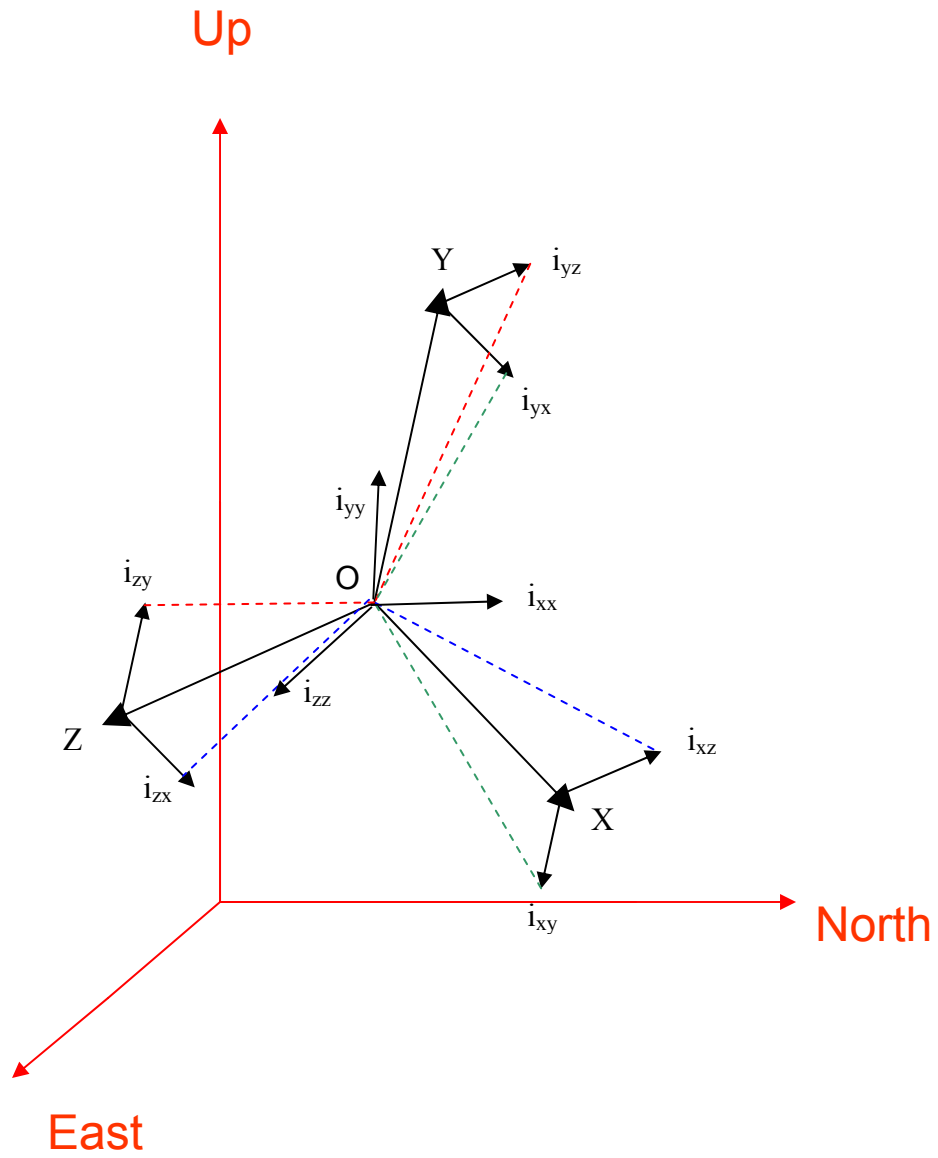


Figure 6.4 Initialization Vectors of the Body Coordinate Frame

6.6 Summary And Conclusion

This chapter laid out a more advanced six degree of freedom inertial sensor model which contained three rate gyros and three accelerometers with a variety of input/output error terms. The input/output error terms in the three accelerometer models included misalignment error, nonorthogonality error, scale factor error, scale factor asymmetry error and scale factor nonlinearity error. The input/output error terms in the three rate gyro models included misalignment errors, nonorthogonality errors and scale factor error. Each of these terms was defined and pictorially presented. Finally, this chapter defined the inertial measurement unit's initialization errors.

CHAPTER 7

INTEGRATION ERRORS OF THE SIX DEGREE OF FREEDOM ADVANCED INERTIAL MEASUREMENT UNIT MODEL

7.1 Introduction

This chapter will discuss the integration errors of the six degree of freedom advanced inertial measurement unit model presented in Chapter 6. A comparison of the advanced model versus the simple model of chapter five will be illustrated with a common rocket launch trajectory. The comparison will identify the effects the advanced models error parameters have on the inertial measurement unit's navigation capabilities.

7.2 Launch Trajectory Profile I

The trajectory chosen for this comparison is one which simulates a rocket launch. The rocket is elevated to a pitch angle of 55 degrees before ignition. The longitudinal and lateral axes are aligned with the north and east axis. A maximum thrust of 8 g's is introduced in the rockets longitudinal axis. The thrust is sufficient to project the rocket a distance of 84 km due north. The body frame accelerations and heading angles are shown in Figure 7.1a and Figure 7.1b. The rocket velocities in the NEU coordinate frame

are shown in Figure 7.1c. A graph of the rockets altitude versus range is shown in Figure 7.2.

As seen in Figure 7.1a, an initial thrust of 8 g's is introduced in the rockets longitudinal axis. Since the rocket is elevated to a pitch angle of 55 degrees, the longitudinal accelerometer will read a negative component of gravity. As the rocket peaks and begins its downward slope, the longitudinal accelerometer will begin to read a positive component of gravity. The existence of the gravity field will introduce a slight error in the position calculation as shown previously in Chapter 5

As seen in Figure 7.1b, the rocket is elevated to a 55 degree pitch angle. After the initial thrust is introduced, the rocket maintains this pitch angle for approximately 6 seconds. After 6 seconds, a -10 degree per second pitch rate begins for 15 seconds. This results in a final pitch angle of -88 degrees.

As seen in Figure 7.1c, the initial thrust brings the northern and upward velocities to approximately 550 meters per second. After the rocket peaks and begins its downward part of the trajectory, it reaches a final impact velocity of nearly 600 meters per second.

As seen in Figure 7.2, the rocket travels down range 86 kilometers in 165 seconds. In 40 seconds it reaches a peak altitude of 24 kilometers

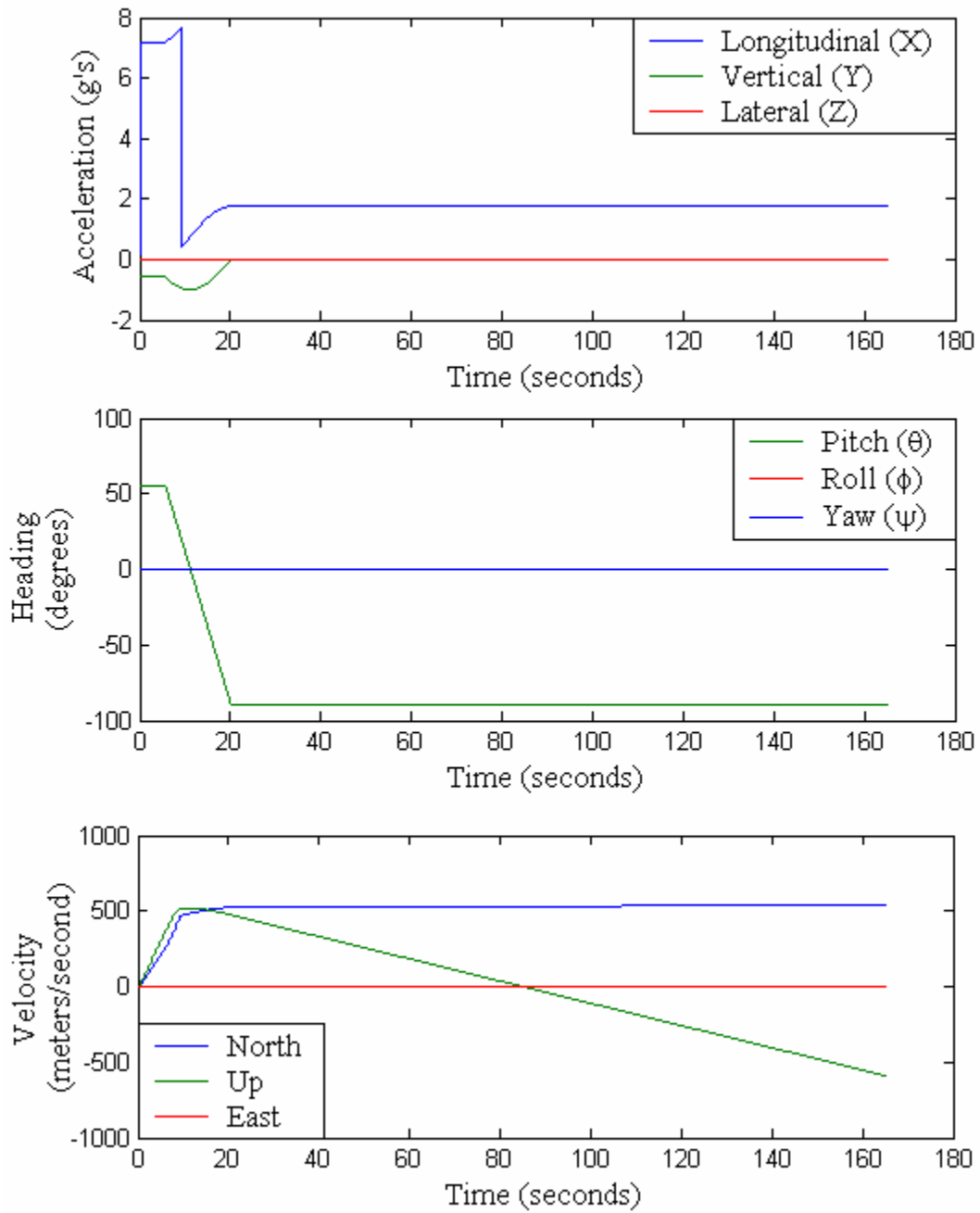


Figure 7.1

Rocket Launch Trajectory I
 Body Accelerations, Body Headings and ENU Velocities

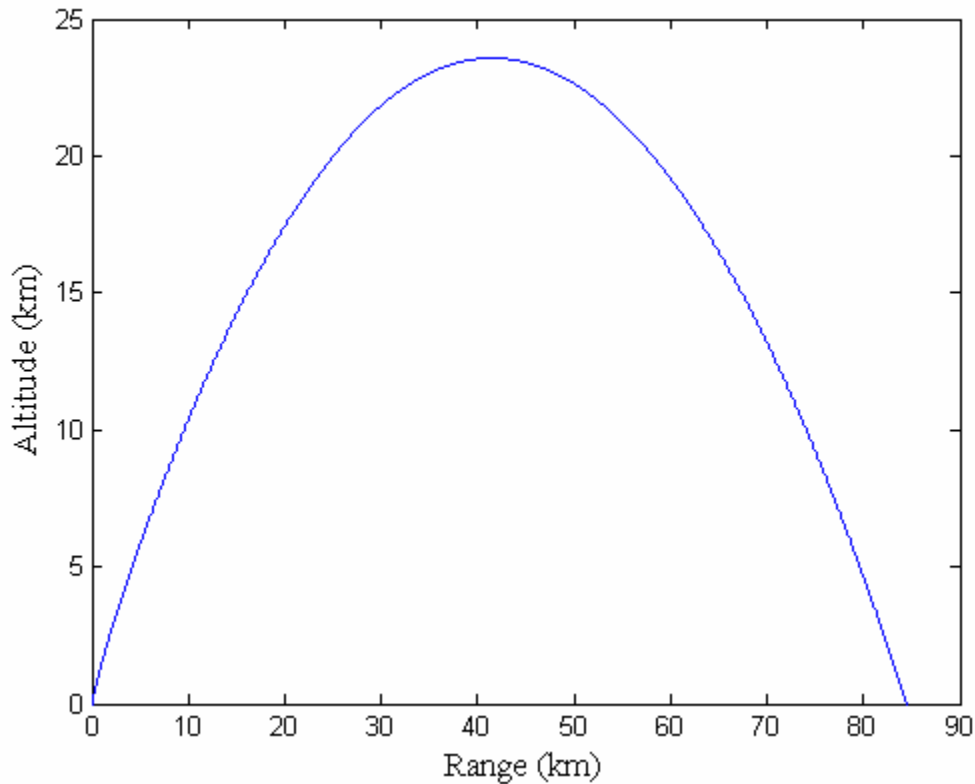


Figure 7.2 Rocket Launch Trajectory I Altitude Vs. Range

7.3 Comparison of the Simple and Advanced IMU Models

To compare the simple model to the advanced model, the above trajectory was used. Each six degree of freedom model was run in a Monte Carlo simulation for 200 iterations. Tactical grade IMU specifications were used in both the simple and advanced models. The purpose of this comparison is to evaluate the effects that the additional terms in the advanced model have on the navigation capabilities of an IMU. To do this, the constant bias offset must be very small or non existent. Normally a tactical grade IMU contains as little as 1 deg per hour of bias offset in the rate gyros and as little as 400

micro g's of bias offset in the accelerometers. For this comparison, the constant bias offset of the tactical IMU was set to zero. The initialization errors discussed in chapter 6 were also neglected in order to identify the input/output parameter with the largest impact. The comparison point was chosen to be at the point of impact. Figure 7.3 is a scatter plot of the calculated impact point for both of the inertial measurement unit models.

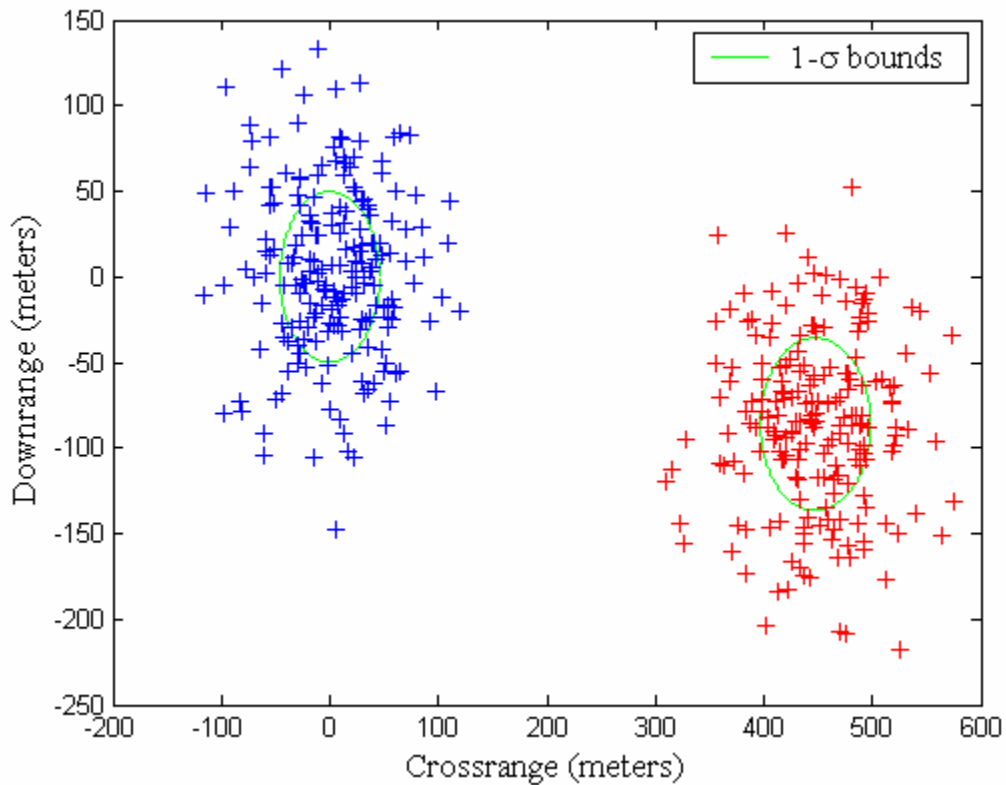


Figure 7.5 Rocket Launch Trajectory Impact Point Scatter Plot

The blue data clusters represent the impact point calculated by the simple model. The red data clusters represent the impact point calculated by the advanced model. The standard deviation for both clusters is 50 meters downrange and 50 meters cross range.

However, from the plot it is evident that the two clusters have different downrange and cross range means. The simple model of chapter five has a mean center line at the origin of the downrange and cross range axes. This is expected because the wide band noise and Markov process for each inertial sensor in the simple model have a mean of zero. The advanced model has a mean cross range center line of 450 meters east of the actual impact point and a mean downrange center line of 86 meters south of the actual impact. Because the moving bias and wide band noise statistics are the same for each model, the shifting of the center line can only be contributed to the additional input/output parameters modeled in the advanced model.

7.4 Advanced Model Error Parameter Contribution Levels

To determine the contribution level each of the input output error parameters has on the total error, a simulation was run for each error parameter individually. The magnitude of the contribution level for each error parameter was calculated by taking the second norm of an error vector at the impact point. Figure 7.4 is a bar graph of each of the error parameters contribution levels as well as the total error level.

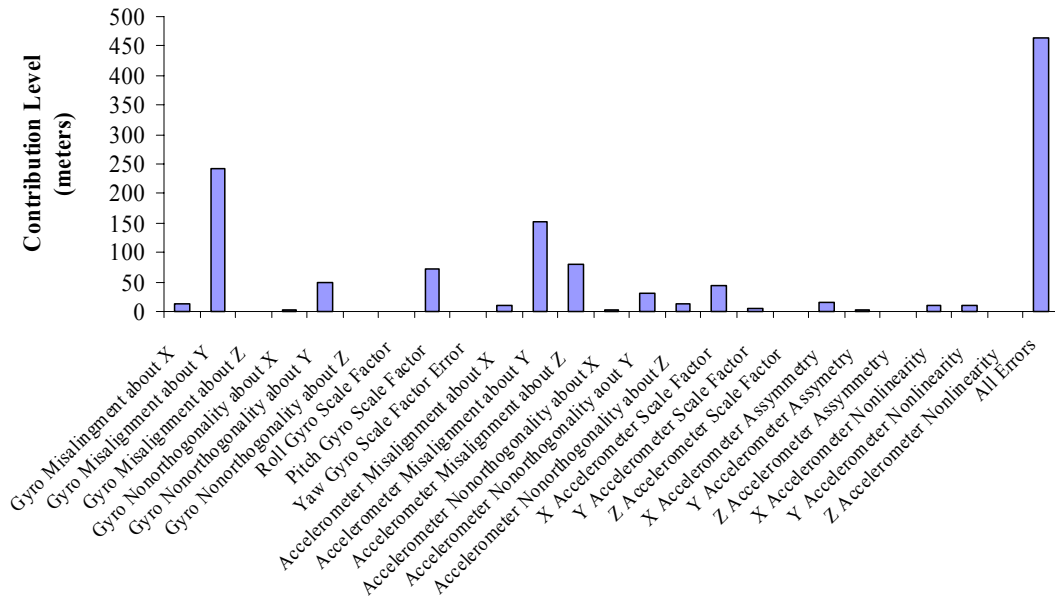


Figure 7.4 Rocket Launch Trajectory I Error Parameters Contribution Levels

From the bar graph, it is now possible to identify the error parameters which contribute the greatest to the total error in the impact point calculation for this rocket launch trajectory. The gyro misalignment about Y has the highest contribution level for this simple trajectory. This is due to the fact that the roll measurement is directly affected when there is a pitch rate applied to the body frame, as seen in Equation (6.7). The accelerometer misalignment about Y is the second highest contributor to error. This effect is due to the fact that the lateral acceleration is directly affected when there is a longitudinal acceleration applied to the body frame, as shown previously in Equation (6.3).

7.5 Summary and Conclusion

This chapter discussed the integration errors of the six degree of freedom advanced inertial measurement unit model presented in Chapter 6. A comparison of the advanced model versus the simple model of Chapter 5 was illustrated with a common rocket launch trajectory. The comparison showed that the advanced models error parameters caused the calculated position to be skewed away from the actual position. It was also shown that the contribution level for each of the error parameters was dependent on the trajectory.

CHAPTER 8

CONCLUSION

8.1 Summary

In Chapter 2, a simple sensor model was laid out that incorporated a moving bias, a constant bias, and a random error. The biases and random error sources were analyzed statistically. The numerical values for the time constants, means, and variances were obtained by using common statistical methods, Allan Variance charts, Autocorrelation functions, and Monte Carlo Simulations. The statistical parameters of the error sources were used to categorize and characterize the sensors. The inertial sensors were categorized into four basic grades: navigational, tactical, automotive, and consumer. Several sensor grades were simulated and experimentally validated. A group of tables was provided which contained the specification for a number commonly used rate gyros and accelerometers. Additional tables were also provided which can be used to classify the sensors.

Chapter 3 discussed the errors associated with the integration of a single rate gyro and single accelerometers to calculate position, velocity and heading in a planar setting. The error growths of the position, velocity, and heading calculation were depicted with the use of a Monte Carlo Simulation. Both consumer and tactical grade sensor characteristics were compared and experimental data was used to validate the bounds of

the Monte Carlo simulations. The Monte Carlo simulations were validated by showing the error growths of rate gyros and accelerometers which contain moving biases and comparing them to simulations where the only error source was wide-band noise. Analytical solutions for position, velocity and heading errors were derived which plot the error growths depicted by the integration of rate gyros and accelerometers which contain only one error source, wide-band noise. Finally, a gravity field was introduced. The error growths of the position and velocity calculations were compared with a gravity field and without.

Chapter 4 implemented a Kalman Filter which combined the GPS position, velocity and heading measurements with the inertial sensor measurements. The Kalman filter incorporated the sensor model presented in Chapter 2. It was shown that the coupling of the GPS measurements and the sensor model to calculate the position, velocity and heading from the combined GPS and IMU measurements resulted in new error bounds for position, velocity and heading. It also was shown that the steady state error bounds were the same for both the two state Kalman filter and the three state Kalman filter when used to estimate heading. The two state Kalman filter provided an estimation of the rate gyros biases. However, the bias had to be either modeled as a random walk or a first order Markov process. Monte Carlo simulations were used to demonstrate the difficulty in choosing the model type. The three state Kalman filter provided an estimation of the rate gyros bias and was able to estimate both a constant component as well as a moving component. Experimental data was used to validate the bias estimations in the three state Kalman filter. A five state model was laid out which

estimates two bias components in an accelerometer. These components include a constant part and a moving part.

Chapter 5 discussed the errors associated with the integration of three rate gyros and three accelerometers to calculate position, velocity and heading in a 3 dimensional setting. First the IMU model was laid out along with the Runge-Kutta order four integration routine. Then the error growth of the position, velocity, and heading calculations were depicted using Monte Carlo simulations. Both a consumer grade and tactical grade inertial measurement unit were simulated and the effects of a gravity field were pictorially shown for each.

Chapter 6 laid out a more advanced six degree of freedom inertial sensor model which contained three the rate gyros and three accelerometers with a variety of input/output error terms. The input/output error terms in the three accelerometer models included misalignment error, nonorthogonality error, scale factor error, scale factor asymmetry error and scale factor nonlinearity error. The input/output error terms in the three rate gyro models included misalignment errors, nonorthogonality errors and scale factor error. Each of these terms was defined and pictorially presented. Finally, this chapter defined the inertial measurement unit's initialization errors.

Chapter 7 discussed the integration errors of the six degree of freedom advanced inertial measurement unit model presented in Chapter 6. A comparison of the advanced model versus the simple model of Chapter 5 was illustrated with a common rocket launch trajectory. The comparison showed that the advanced models error parameters caused the calculated position to be skewed away from the actual position. It was also shown

that the contribution level for each of the error parameters was dependent on the trajectory.

8.2 Recommendations for Future Work

Future work should include using the procedure laid out in Chapter 2 to determine the statistical properties of a variety of other consumer, automotive and tactical grade sensors not listed in this work. The error analysis performed in Chapter 3 should be done for cases where the sensors are not static in order to validate the robustness of the procedure. Equations should be derived that represent the error growth for a non static sensor and compare these equations to the ones derived in Chapter 3. This comparison can be used to analyze the effects dynamics play in the sensor error growth. Equations should be derived which depict the error growth for the contribution of the walking bias. These equations, in conjunction with the equations derived in Chapter 3, then can be used to predict the total error growth due to wide band noise and the walking bias modeled as a first order Markov process. Equations should be derived which depict the error growth due to the introduction of a gravity field. These equations can then be used to analyze the effects gravity has on the error growth in a two degree of freedom scenario and possibly a six degree of freedom scenario. The bounded error shown in Chapter 4, which is the result of the coupling of the IMU with a GPS signal, should be derived analytically. With the analytical solution for these error bounds, it would be possible to determine what grade sensor is necessary for a particular coupling application. The error bounds for a six degree of freedom in Chapter 5 should be derived analytically. With the analytical

solution of a six degree of freedom system, it would be possible to compare them to the error bounds of a two degree of freedom system. The comparison could reveal the effects the rotation matrix has on the error growth. The stability of the input/output terms presented in Chapter 6 should be studied and a procedure to determine their stability should be created. Finally, more trajectories should be used to analyze the contribution levels of these input/output terms.

REFERENCES

- [1] Allan D.W, “*Statistics of Atomic Frequency Standards*” 1966 Vol. 54 pp 221-230, Institute of Electrical and Electronics Engineers Proceedings.
- [2] Beckwith, Thomas G. Mechanical Measurements 5th Ed. Addison-Wesley Publishing Company. 1993.
- [3] BEI. Systron Donner Inertial Division. “BEI Gyrochip Model AQRS”. BEI technologies, INC. 1998.
- [4] Bennett, S.M. “*Fiber Optic Rate gyros as Replacements fro Mechanical Gyros*”. KVH Industries. 1998.
- [5] Bevly David M. “*Comparison of INS vs. Carrier-Phase DGPS for Attitude Determination in the Control of Off Road Vehicles*”. *Navigation: Journal of the Institute of Navigation*. Vol. 47, Number 4. Winter 2000-2001, pp 257-266.
- [6] Bevly, David M. “*Evaluation of a Blending Dead Reckoning and Carrier Phase Differential GPS System for Control of an Off-Road Vehicle*” 1999 ION/GPS Proceedings
- [7] Bevly, David M. High Speed, Dead Reckoning, Towed Implement Control for Automatically Steered Farm Tractors Using GPS. A Dissertation submitted to the Department of Aeronautics and Astronautics and the committee on graduate studies of Stanford University, Stanford University 2001.
- [8] Borenstein, Johann, “Experimental Evaluation of a Fiber Optics Gyroscope for Improving Dead Reckoning Accuracy in Mobile Robots” Proceedings of the IEEE International Conference on Robotics and Automation. 1998 pp3456-3461
- [9] Bosch, P. P. J. van den. Modeling Identification and Simulation of Dynamic Systems. CRC Press. 1994.
- [10] Brogan, Willam L. Modern Control Theory. Prentice Hall. 1991.
- [11] Brown, Robert G. Introduction to Random Signals and Applied Kalman Filtering 3rd Ed. John Wiley and Sons. 1997.

- [12] Burden, Richard L. Numerical Analysis 7th Ed. Wadsworth Group. 2001.
- [13] Chatfield, Averil B. Fundamentals of High Accuracy Inertial Navigation. American Institute of Aeronautics and Astronautics, Inc. 1997.
- [14] Chobotov, Vladimir A. Orbital Mechanics 3rd Ed. American Institute of Aeronautics and Astronautics, Inc. 2002.
- [15] Demoz, Gebre-Egziabher. “An Inexpensive DME-Aided Dead reckoning Navigator”. *Navigation: Journal of the Institute of Navigation*. Vol. 50, Number 4. Winter 2003-2004, pp 247-264.
- [16] Demoz, Gebre-Egziabher Design and Performance Analysis of a Low-Cost Aided Dead Reckoning Navigator A Dissertation submitted to the Department of Aeronautics and Astronautics and the committee on graduate studies of Stanford University, Stanford University 2003.
- [17] Devore, Jay L. Probability and Statistics. Duxbury. 2000.
- [18] Dorf, Richard C. Modern Control Systems. Addison-Wesley. 1998.
- [19] Ellum, Cameron. “*Inexpensive Kinematic Attitude Determination from MEMS-Based Accelerometers and GPS-Derived Accelerations*”. *Navigation: Journal of the Institute of Navigation*. Vol. 49, Number 3. Fall 2002, pp 117-126.
- [20] Farrel, J. L. “*Comments on Performance Analysis of a Tightly Couple GPS/Inertial System for Two integrity Monitoring Methods*”. *Navigation: Journal of the Institute of Navigation*. Vol. 48, Number 2. Summer 2001, pp 131-132.
- [21] Ford, Tom. “*MEMS Inertial on RTK GPS Receiver: Integration Options and Test Results*”. Honeywell International Inc. 2002
- [22] Franklin, Gene F. Feedback Control of Dynamic Systems. Prentice Hall. 2002.
- [23] Gelb, Arthur. Applied Optimal Estimation. The M.I.T. Press. 1974.
- [24] Ginsberg, Ferry H. Advanced Engineering Dynamics 2nd Ed. Cambridge University Press 1998
- [25] Ginsberg, Jerry H. Advanced Engineering Dynamics 2nd Ed. Cambridge University Press. 1998.
- [26] Grewal, Mohinder S. Global Positioning System, Inertial Navigation and Integration. A John Wiley and Sons, Inc. 2001

- [27] Hamm, C., Flenniken, W., Bevely, D.M., and Lawrence, D. "Comparative Performance Analysis of Aided Carrier Tracking Loop Algorithms in High Noise/High Dynamic Environments". Proceedings of the 2004 ION-GNSS Conference.
- [28] Honeywell. "*HG1700 Inertial Measurement Unit*". Honeywell International Inc. 2002.
- [29] Honeywell. "*HG1900 Inertial Measurement Unit*". Honeywell International Inc. 2002.
- [30] Kreyszig, Erwin. Advanced Engineering Mathematics 8th ED. John Wiley and Sons. 1999.
- [31] Leach, Barrie W. "*Operational Experience with Optimal Integration of Low-Cost Inertial Sensors and GPS for Flight Test Requirements.*" Flight Test Laboratory. Volume 49, Number 2 June 2003. pp 41-54
- [32] Lee, Young. "*Reply to Comments on Performance Analysis of a Tightly Couple GPS/Inertial System for Two integrity Monitoring Methods*". *Navigation: Journal of the Institute of Navigation*. Vol. 48, Number 2. Summer 2001, pp 133.
- [33] Leon, Steven J. Linear Algebra with Applications. Prentice Hall. 1998.
- [34] Nassar, Sameh. "*Modeling Inertial Sensor Errors Using Autoregressive (AR) Models*". *Navigation: Journal of the Institute of Navigation*. Vol. 51, Number 4. Fall Winter 2004, pp 259-268.
- [35] Northrup Grumman. "*Summary of LN-200 IMU Characteristics*". The Northrup Grumman Group. 2002.
- [36] Ogata, Katsuhiko. System Dynamics 4th Ed. Prentice Hall. 2004
- [37] Petovello, M.G. . "*Benefits of Using a Tactical-Grade IMU for High Accuracy Positioning*". *Navigation: Journal of the Institute of Navigation*. Vol. 51, Number 1. Spring 2004, pp 1-12.
- [38] Selby, Samuel M. Standard Mathematical Tables 12th Ed. The Chemical Rubber Co. 1972.
- [39] Skaloud, Jan. "*Reducing the GPS Ambiguity Search Space by Including Inertial Data*". 2004 ION/GPS Proceedings
- [40] Stengel, Rober F. Optimal Control and Estimation. Dover Publications. 1994.
- [41] Webster, Noah. Webster's third New International Dictionary. G and C Merriam

Company. 1966.

- [42] Welch, Greg. “*An Introduction to the Kalman Filter*”. UNC-Chapel Hill, TR 95-041, April 5, 2004.
- [43] Zhang, Yufeng. “*Performance Analysis of a Tightly Coupled Kalman Filter for the Integration of Un-differenced GPS and Inertial Data*” 2004 ION/GPS Proceedings
- [44] Zifel, Peter H. Modeling and Simulation of Aerospace Vehicle Dynamics. American Institute of Aeronautics and Astronautics, Inc. 2000.

APPENDICES

APPENDIX A

THE ALLAN VARIANCE

A.1 Introduction

The Allan variance was developed by David W. Allan. A full explanation of the technique can be found in [3]. The Allan variance can be viewed as the time domain equivalent of the power spectrum. However, the Allan variance plots power as a function of time averaging blocks as opposed to plotting power as a function of frequency. This appendix introduces the basic equations needed to plot an Allan variance. Examples are provided showing how the Allan variance chart changes for various values of wide band noise. Finally Allan variance charts are given for various Markov process parameters. For a more detailed description of the Allan variance, including error identification, review Appendix C [4].

A.2 The Allan Variance Computation

To construct an Allan variance for some process $\omega(t)$, the data is sampled at a predefined frequency (f_s). The total number of data points will then be defined as,

$$N = f_s T \tag{A.1}$$

where T is the duration of the series in seconds

Once the data series has been sampled, the Allan variance chart is constructed using the following procedure:

1. Create a vector of averaging times, τ_{av} :

$$\tau_{av} = \left[1 \quad 2 \quad \dots \quad \frac{T}{2} \right] \text{ seconds} \quad (\text{A.2})$$

2. For each τ_{av} , divide the series $\omega(t)$ into M clusters

$$M(\tau_{av}) = T / \tau_{av} \quad (\text{A.3})$$

3. For each cluster M compute $\bar{\omega}$, the time average of $\omega(t)$.

$$\bar{\omega}(\tau_{av}, k) = \frac{1}{L} \sum_{i=1}^L \omega_i, \quad L = f_s \tau_{av}, \quad \text{and } k = [1 \quad 2 \quad \dots \quad M(\tau_{av})] \quad (\text{A.4})$$

4. Use each of these cluster averages from a specific τ_{av} to form a new variable called the Allan variance $\sigma^2(\tau_{av})$.

$$\sigma^2(\tau_{av}) = \frac{1}{2} E[\bar{\omega}(\tau_{av}, k+1) - \bar{\omega}(\tau_{av}, k)] \quad (\text{A.5})$$

5. Plot each Allan variance, $\sigma^2(\tau_{av})$, versus τ_{av} on a log log scale. This plot is known as the Allan variance chart.

A.3 Wide Band Noise Characteristics

The power of the Allan variance can be seen when analyzing data that is dominated by wide band noise, which is defined below.

$$w \sim N[0, \sigma_{noise}] \quad (\text{A.6})$$

By using the Allan variance chart, it is possible to determine the random walk statistics of a data series. The random walk of a series $w(t)$ is defined at the point where $\sigma^2(\tau_{av})$ crosses $\tau_{av} = 1$. The follow equation can be used to calculate this intersection.

$$\sigma^2(1) = \sigma_{noise} / \sqrt{f_s} \quad (\text{A.6})$$

Figure A.1 is an Allan variance chart for 7 sets of data. The data used was created with a random number generator with a sampling frequency of 100 Hertz, each having a different variance. The sets of random series have a range of variances from 10^{-6} to 10^6 . It is clear that $\sigma^2(\tau = 1)$ maps exactly where the above equation predicts.

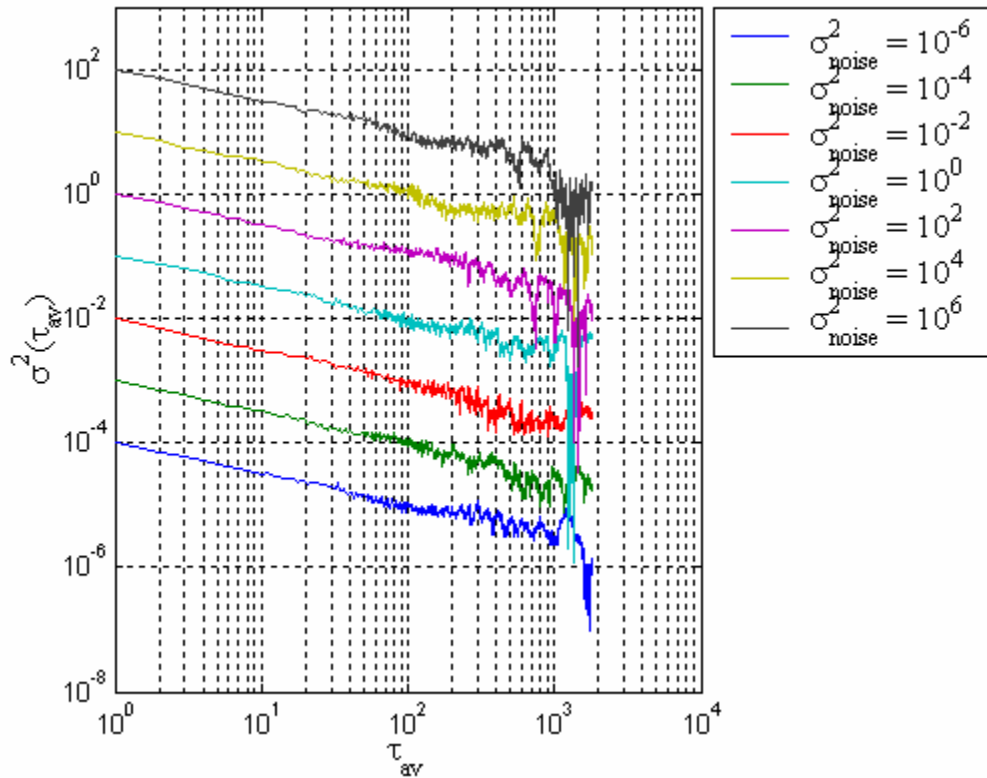


Figure A.1 Wide Band Noise Allan Variance Comparison

A.4 Markov Process Characteristics

Another strength of the Allan variance is the ability to recognize noise characteristics which are easily modeled as 1st Order Markov Processes. A 1st Order Markov Process is defined as:

$$\dot{b} = \frac{1}{\tau} b + \omega$$

$$b \sim N[0, \sigma_b]$$

The rate at which the differential equation decays is determined by the time constant, τ . When evaluating noise characteristics with an Allan variance chart, an upward sloping curve of $\frac{1}{2}$ denotes a noise which is best modeled as a Markov process with a very slow decay, other Allan variance characteristic errors are given in Table A.1. Curves with flatter slopes denote noises which are best modeled as Markov processes with faster decay time (as determined by the time constant (τ)). Downward sloping curves indicate noises with very fast time constants and are better modeled as wide band noise but can be modeled as a Markov Process if enough information is available. Figure A.2 is a comparison of Allan variances from data generated by Markov Processes with time constants ranging from 10^{-2} to 10^4 seconds and a variance of σ_b^2 equal to 1.

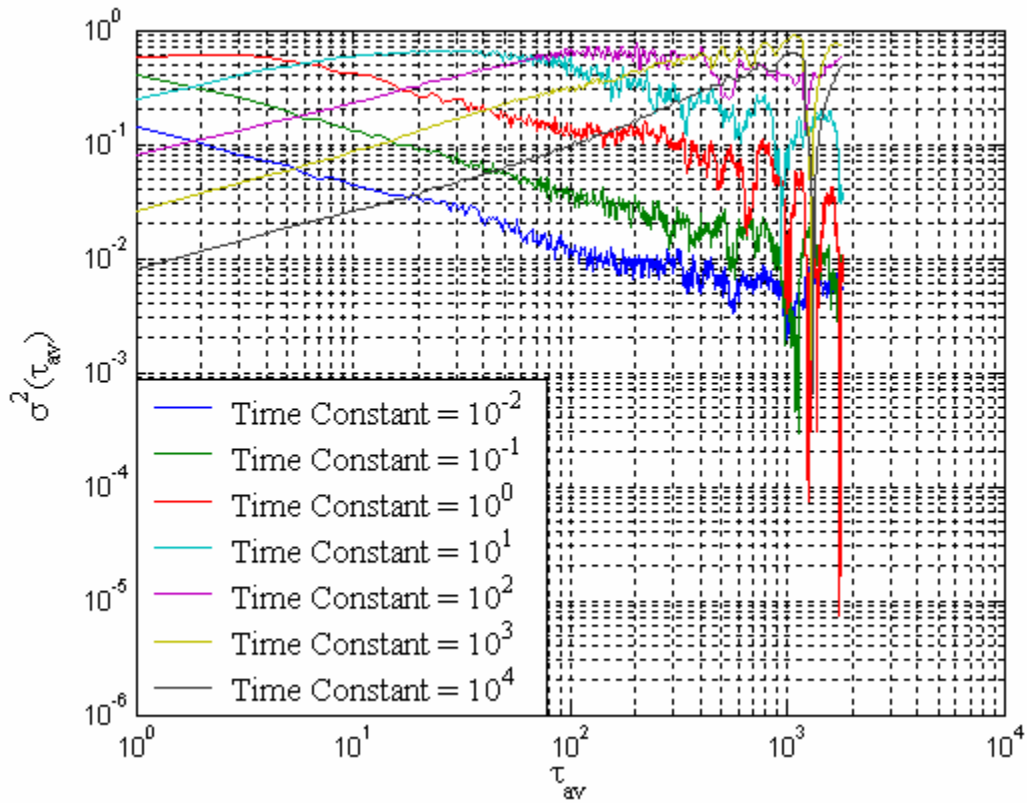


Figure A.1 Wide Band Noise Allan Variance Comparison

Table A.1 Allan Variance Characteristic Error Mechanisms

Error Mechanism	Allan Variance Slope
Wide-Band Noise	- 1/2
Exponentially Correlated Noise (First Order Markov Process)	1/2
Rate Random Walk	1/2
Linear Rate Ramp	1
Quantization Noise	-1
Sinusoidal Input	1
Flicker Noise	0

APPENDIX B

MARKOV PROCESS STATISTICS

B.1 Introduction

This appendix presents a derivation of the statistics for the input white noise of a First Order Markov Process. A Markov process is a stochastic process where all future values are scaled values of past values plus a random input (described by a first order differential equation). In the case of a first order process, the future value is only dependent on a scaled portion of the first previous value. The follow differential equation represents this:

$$\dot{b} = \frac{1}{\tau}b + \omega \quad (\text{B.1})$$

One purpose of a the Markov Process is to filter wide band noise and produce a data set which is zero mean specific standard deviation. The following is a statistical representation of this.

$$b \sim [0, \sigma_b] \quad (\text{B.2})$$

B.2 Derivation

The ability to control the output statistics is the key to the Markov process. The derivation of the standard deviation of the input noise (ω) is obtained by:

$$b = \int (\dot{b}) dt \quad (\text{B.3})$$

Substituting the Markov differential equation (B.1):

$$b = \int \left(-\frac{1}{\tau} b + \omega \right) dt \quad (\text{B.4})$$

Use Euler integration to simplify,

$$b_{k+1} = b_k + T_s \left(-\frac{1}{\tau} b_k + \omega_k \right) \quad (\text{B.5})$$

$$b_{k+1} = \left(1 - \frac{T_s}{\tau} \right) b_k + T_s (\omega_k) \quad (\text{B.6})$$

The expected value of both sides is then taken to find the covariance of the bias.

$$E[bb^T] = E \left[\left(1 - \frac{T_s}{\tau} \right) b \left(\left(1 - \frac{T_s}{\tau} \right) b \right)^T \right] + E[T_s \omega (T_s \omega)^T] \quad (\text{B.7})$$

$$\sigma_b^2 = \left(1 - \frac{T_s}{\tau} \right)^2 \sigma_b^2 + T_s^2 \sigma_\omega^2 \quad (\text{B.8})$$

$$\sigma_{\omega}^2 = \left(\frac{2}{T_s \tau} + \frac{1}{\tau^2} \right) \sigma_b^2 \quad (\text{B.9})$$

Because the time constant (τ) is generally a large value, the inverse square can be assumed to be very small and the second term in Equation (B.9) can be ignored. This results in the following equation for the standard deviation of the input noise.

$$\sigma_{\omega} = \sqrt{\frac{2\sigma_b^2}{T_s \tau}} \quad (\text{B.10})$$

Where T_s is the sampling interval.

B.3 Example

To help better understand the use of the Markov process an example with the following desired statistics is performed.

$$\begin{aligned} b &\sim [0,1] \\ \tau &= 100 \\ T_s &= .01 \end{aligned}$$

Note: τ and T_s are both expressed in seconds.

Using Euler's integration method and a random number generator the following data series was created using the following statistical values.

$$\sigma_b = 1$$

$$\sigma_\omega = \sqrt{\frac{2\sigma_b^2}{T_s \tau}} = 1$$

Figure B.1a provides a plot of the Markov process input noise. Equation B.1 is used to produce the Markov output seen in Figure B.1b.

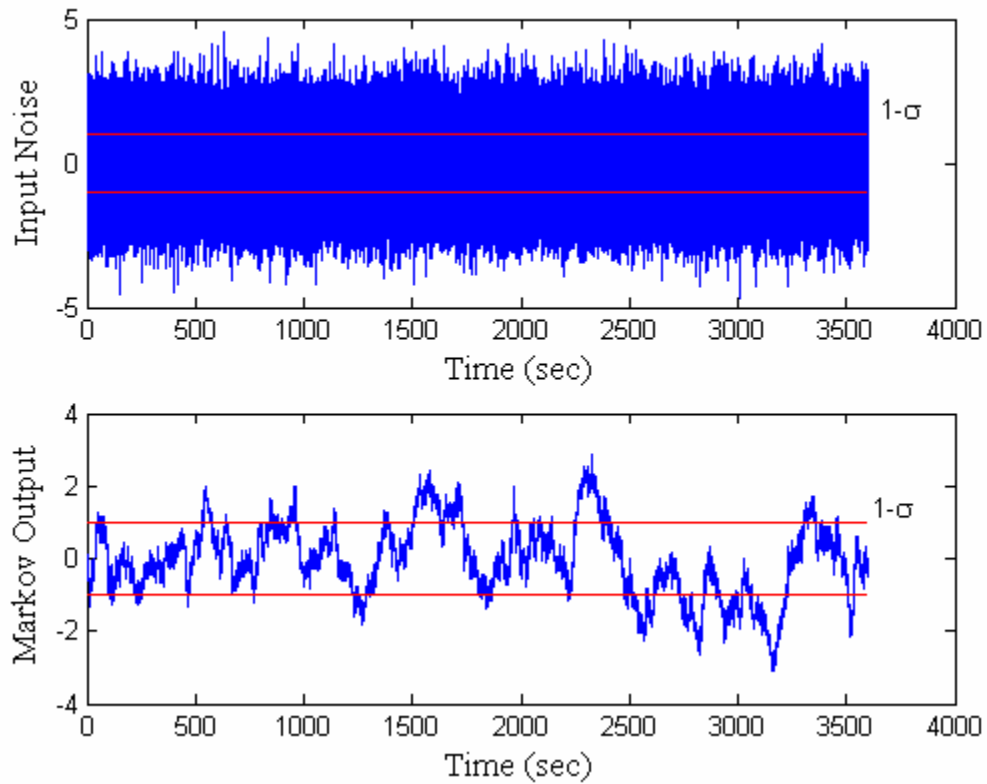


Figure B.1 Input and Output Data for a Markov Process

The actual statistical values which are represented by the red lines in Figure B.1 are as follows.

$$\sigma_b = 1.01246110628949$$

$$\sigma_\omega = \sqrt{\frac{2\sigma_b^2}{T_s \tau}} = 0.99952355902917$$

The desired output statistic was met to within 1%. An autocorrelation function shown below in Figure B.2 was used to validate that the time constant (τ) was preserved.

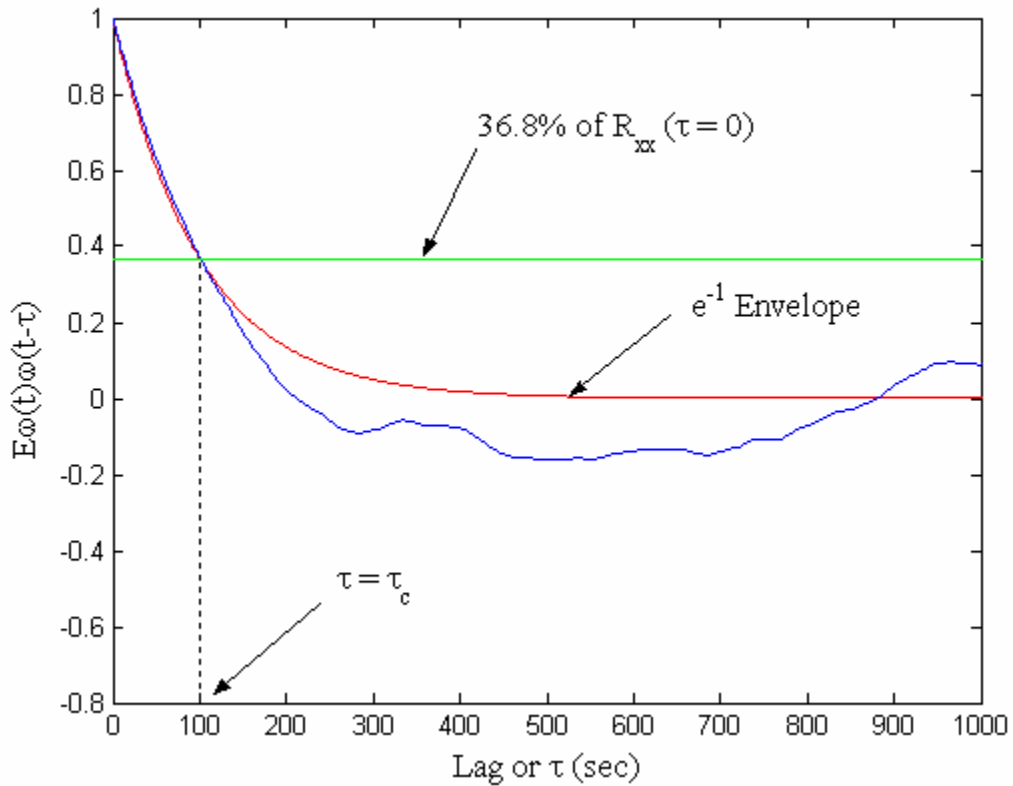


Figure B.2 Markov Process Autocorrelation function

B.5 Monte Carlo Simulation

A Monte Carlo simulation (using 100 iterations) was used to verify that as the frequency, time constant and bias standard deviation are changed, the first order Markov process continues to meet the desired output requirements. The results of the Monte Carlo simulation are shown in Figure B.3. Although there are some discrepancies in the magnitude of the Markov outputs, as the desired bias standard deviation increases these errors are still acceptable. The errors are acceptable for this work because the average Markov output used will be much less than ten.

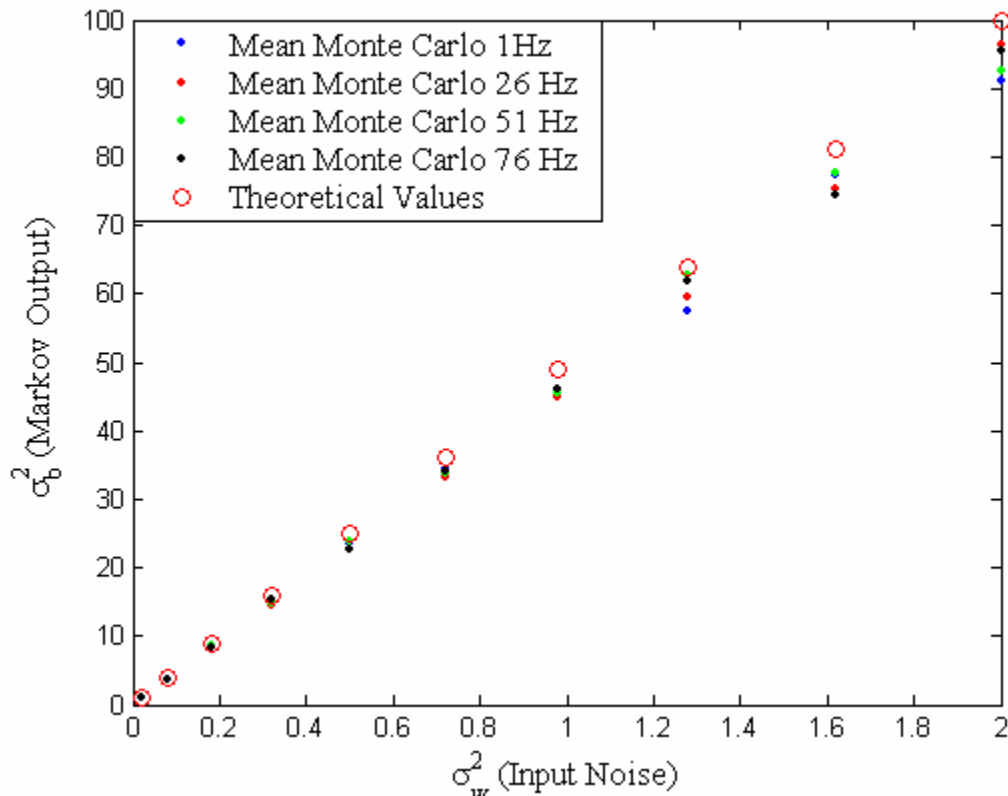


Figure B.2 Markov Process Comparison Plot

APPENDIX C

AN INTROCUCTION TO THE KALMAN FILTER

C.1 Introduction

The Kalman filter is a set of mathematical equations that provides an efficient computational (recursive) means to estimate the state of a process in a way that minimizes the mean of the squared error. The filter is very powerful in several aspects. It supports estimations of past, present, and even future states, even when the precise nature of the modeled system is unknown. It also allows for methods to fuse high rate input, such as rate gyroscopes and accelerometers with GPS. Although these estimates are not observable, they have been shown capable of being used in many navigation and control systems. [Bevly] [Demoz]

C.2 System Format

The Kalman Filter will estimate the states, $x \in \mathfrak{R}^n$, of a discrete system that are governed by the linear stochastic difference equation

$$x_k = A_d x_{k-1} + B_d u_{k-1} + w_{k-1} \quad (\text{C.1})$$

and are observed with the measurements $y \in \mathfrak{R}^m$ which are represented as

$$y_k = C_d x_k + v_k \quad (\text{C.2})$$

The random variables w_k and v_k represent the process and measurement noises.

They are assumed to be white, normally distributed and independent of each other.

$$E[ww^T] = Q_d$$

$$E[w] = 0, E[v] = 0$$

$$Q_d = E[ww^T] = \sigma_w^2, R_d = E[vv^T] = \sigma_v^2$$

$$w \sim N[0, Q_d], v \sim N[0, R_d]$$

In practice, the process noise covariance matrix, Q_d and the measurement noise covariance matrix, R_d might change with each time step. However, in this work both are assumed to be constant for all time.

The $n \times n$ matrix A_d relates the state at the current time step k to the state at the next time step $k+1$. The $n \times l$ matrix B_d relates the input $u \in \mathfrak{R}^l$ to the states x . The $m \times n$ matrix C_d relates the states to the measurements z . In this work, the matrix C_d will change depending on the output rate of the IMU and the output rate of the GPS receiver.

C.3 State Format

Defining $\hat{x}_k^{(-)} \in \mathfrak{R}^n$ to be the state estimate at time step k given knowledge of the process prior to step k , and defining $\hat{x}_k^{(+)} \in \mathfrak{R}^n$ to be the state estimate at step k given measurement z_k , the state estimate error then becomes

$$e_k^{(-)} = x_k - \hat{x}_k^{(-)} \quad (C.3)$$

$$e_k^{(+)} = x_k - \hat{x}_k^{(+)} \quad (C.4)$$

The state estimate error $e_k^{(-)}$ covariance matrix is defined as

$$P_k^{(-)} = E[e_k^{(-)}(e_k^{(-)})^T] \quad (C.5)$$

and the state estimate error $e_k^{(+)}$ covariance matrix is defined as

$$P_k^{(+)} = E[e_k^{(+)}(e_k^{(+)})^T] \quad (C.6)$$

The equation which computes the state estimate $\hat{x}_k^{(+)}$ is a linear combination of the state estimate $\hat{x}_k^{(-)}$ and a weighted difference between an actual measurement z_k and a predicted measurement $C_d \hat{x}_k^{(-)}$. This measurement update equation is as follows:

$$\hat{x}_k^{(+)} = \hat{x}_k^{(-)} + L_d (z_k - C_d \hat{x}_k^{(-)}) \quad (C.7)$$

The difference $(z_k - C_d \hat{x}_k^{(-)})$ is called the measurement innovation. It reflects the discrepancy between the predicted measurement and the actual measurement. An innovation of zero would mean that both are in complete agreement.

C.4 Gain Format

The $n \times m$ matrix L_k is the gain that minimizes the error covariance matrix $P_k^{(+)}$, known as the Kalman gain. The following equation is used to calculate the Kalman gain.

$$L_k = \frac{P_k^{(-)} C_d^T}{C_d P_k^{(-)} C_d^T - R_d} \quad (C.8)$$

By observation, it can be seen that when the measurement noise covariance matrix R approaches zero, the gain matrix L weights the measurement innovation more heavily.

$$\lim_{R_d \rightarrow 0} L_k = C_d^{-1}$$

However, when the state estimation error covariance matrix $P_k^{(-)}$ approaches zero, the gain matrix L weights the measurement innovation less heavily.

$$\lim_{P_k^{(-)} \rightarrow 0} L_k = 0$$

Therefore, the measurement noise covariance matrix approaches zero and the actual measurement is trusted more and more while the predicted measurement is trusted less and less. Likewise, when the state estimation error covariance matrix approaches the actual measurement it is trusted less and the predicted measurement is trusted more

C.5 Kalman Filter Flow Chart

The steps laid out in the above sections are shown a flow chart below.

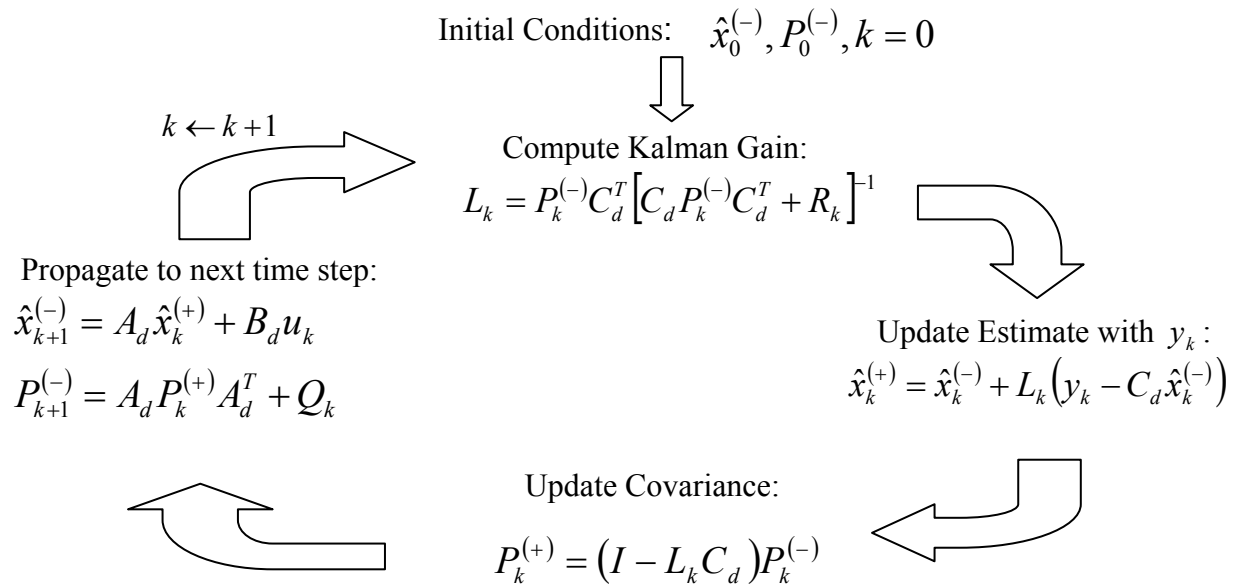


Figure C.1 Kalman Filter Flow Chart

APPENDIX D

THE AUTOCORRELATION FUNCTION

D.1 Introduction

For a discrete-time stochastic series, $x(k)$, the autocorrelation function $R_x(\tau)$ is defined by the following equation:

$$R_x(\tau) = E[x(k)x(k-\tau)] = \lim_{N \rightarrow \infty} \frac{1}{N} \sum_{k=0}^N x(k)x(k-\tau) \quad (\text{D.1})$$

Note that the autocorrelation function is symmetric therefore the following is true:

$$R_x(\tau) = R_x(-\tau) \quad (\text{D.2})$$

The 2nd Moment of a stochastic series is defined as:

$$E[x(k)^2] = \lim_{N \rightarrow \infty} \frac{1}{N} \sum_{k=0}^N x(k)^2 \quad (\text{D.3})$$

Therefore the autocorrelation function is equal to the 2nd Moment of the stochastic series when τ is equal to zero as shown below

$$R_x(0) = E[x(k)x(k-0)] = \lim_{N \rightarrow \infty} \frac{1}{N} \sum_{k=0}^N x(k)x(k-0) \quad (\text{D.4})$$

$$R_x(0) = \lim_{N \rightarrow \infty} \frac{1}{N} \sum_{k=0}^N x(k)^2 \quad (\text{D.5})$$

$$R_x(0) = E[x(k)^2] \quad (\text{D.6})$$

The autocorrelation function can be thought of as a means to determine how much the series, $x(k)$, looks like the series, $x(k - \tau)$, a delayed version of $x(k)$. To understand the utility of the autocorrelation function, a known discrete series will be shown.

Given the function:

$$x(k) = \sin\left(\frac{2\pi}{100}k\right) \quad (\text{D.7})$$

where the second moment is:

$$E[x(k)^2] = 0.5 \quad k \rightarrow \infty \quad (\text{D.8})$$

Figure D.1 contains a plot of the above function. It also contains a plot of the above function shifted for various values of τ . As expected, the plot shows the function diverging from itself as $0 < \tau \leq 50$ and then converging on itself as $50 < \tau \leq 100$.

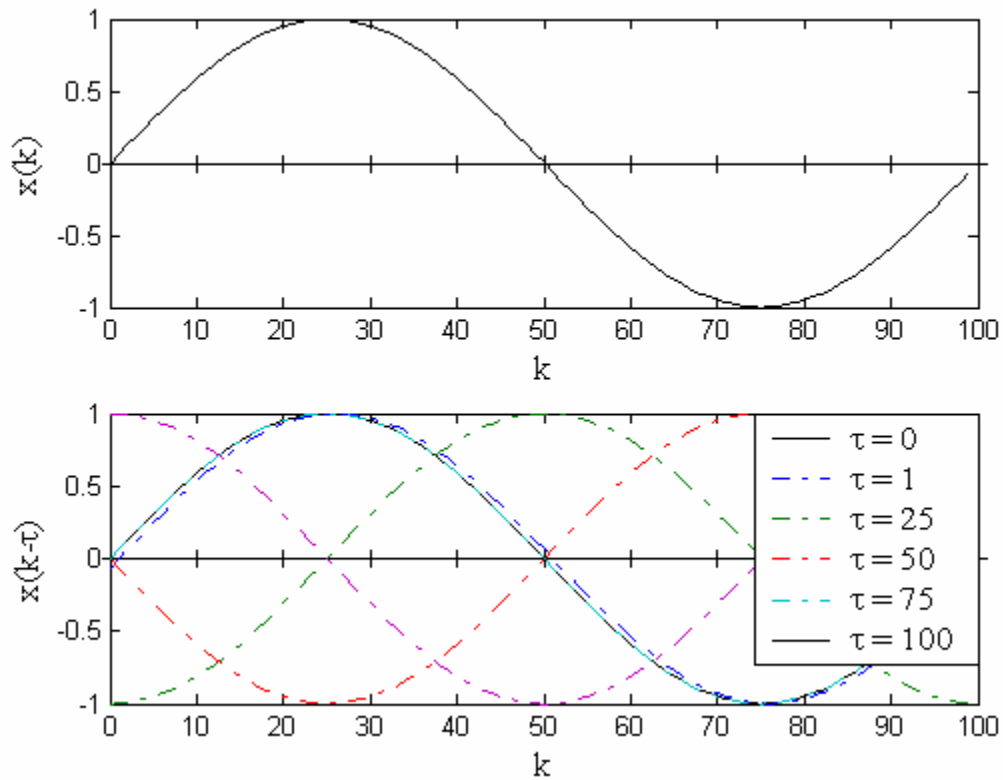


Figure D.1 Plot of a Sine Wave

The autocorrelation function can be used to represent this convergence and divergence numerically. For any giving value of τ , a numerical value of the autocorrelation function can be calculated. The larger this numerical value is, positive or negative, the better the prediction of how the series will look in the future. Figure D.2 is a plot of the autocorrelation for the previous function. As seen in Figure D.2, the highest correlation is when τ is equal to 100 and 50. The lowest correlation is when τ is equal to 25 and 75 (representing the sine wave being 180° out of phase).

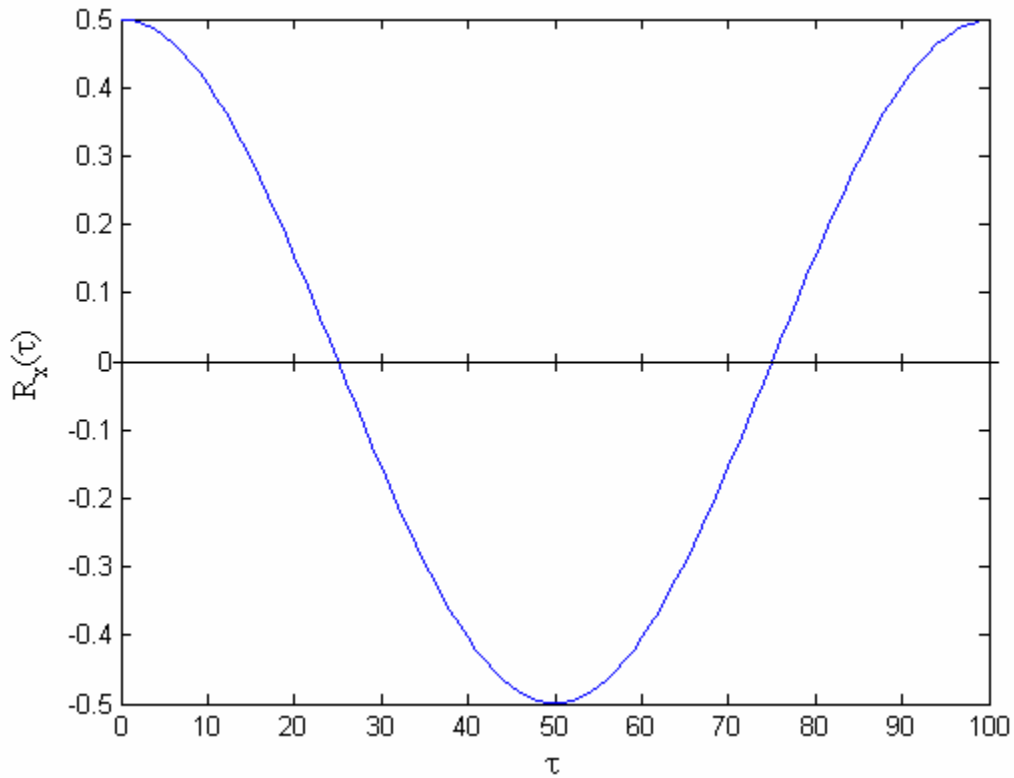


Figure D.2 Autocorrelation of a Sine Wave

To better understand the autocorrelation function, the following discrete random series is now examined.

$$x(k) \sim N[0, \sigma_{x(k)}^2] \quad (\text{D.9})$$

$$\sigma_{x(k)}^2 = .5 \quad k \rightarrow \infty \quad (\text{D.10})$$

Figure D.3 contains a plot of a random series with the above statistics. It also contains a plot of the above series shifted for various values of τ . By definition, a random series can not be predicted by shifting the series in time. Therefore, as seen in Figure D.3, the series will always diverge from itself when $\tau \neq 0$.

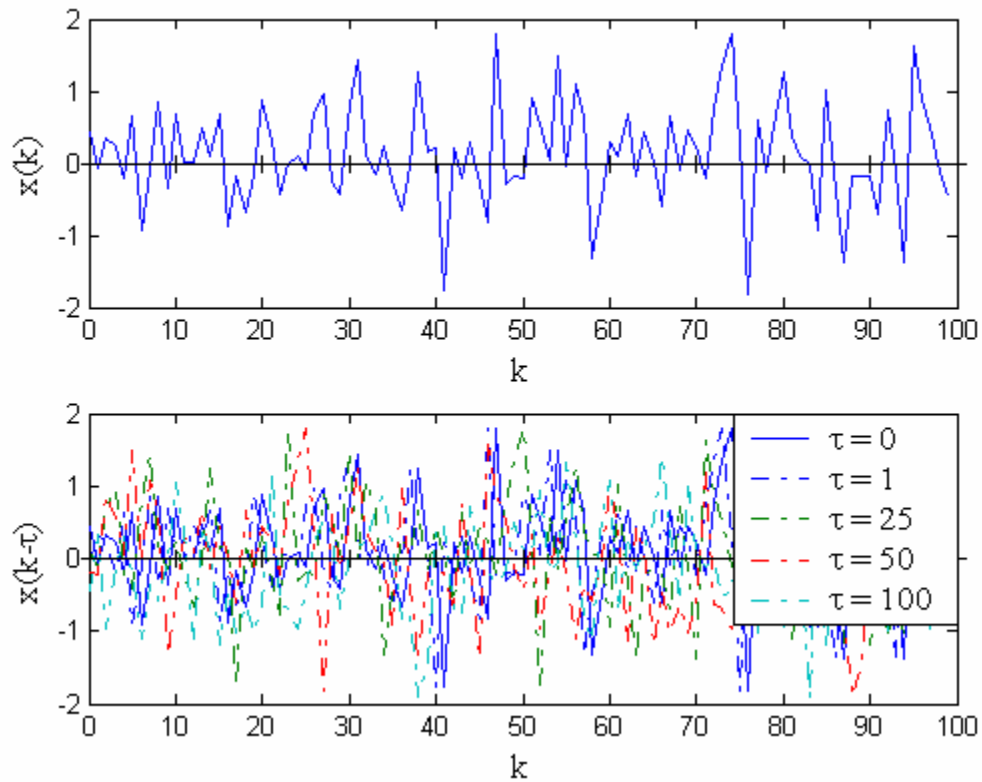


Figure D.3 Plot of a Random Series

Since the random series will never repeat itself the autocorrelation is derived to be as follows. A full derivation can be found in [11].

$$R_x(0) = \sigma_x^2 \quad (\text{D.11})$$

$$R_x(\tau > 0) = 0 \quad (\text{D.12})$$

Figure D.4 is a plot of the autocorrelation for the above random series. At τ equal to zero the autocorrelation is equal to the 2nd Moment of the series and for $\tau > 0$ the autocorrelation is approximately equal to zero. The error in the autocorrelation for the values of $\tau > 0$ can be contributed to the number of data point in the series and the integrity of the random number generator used.

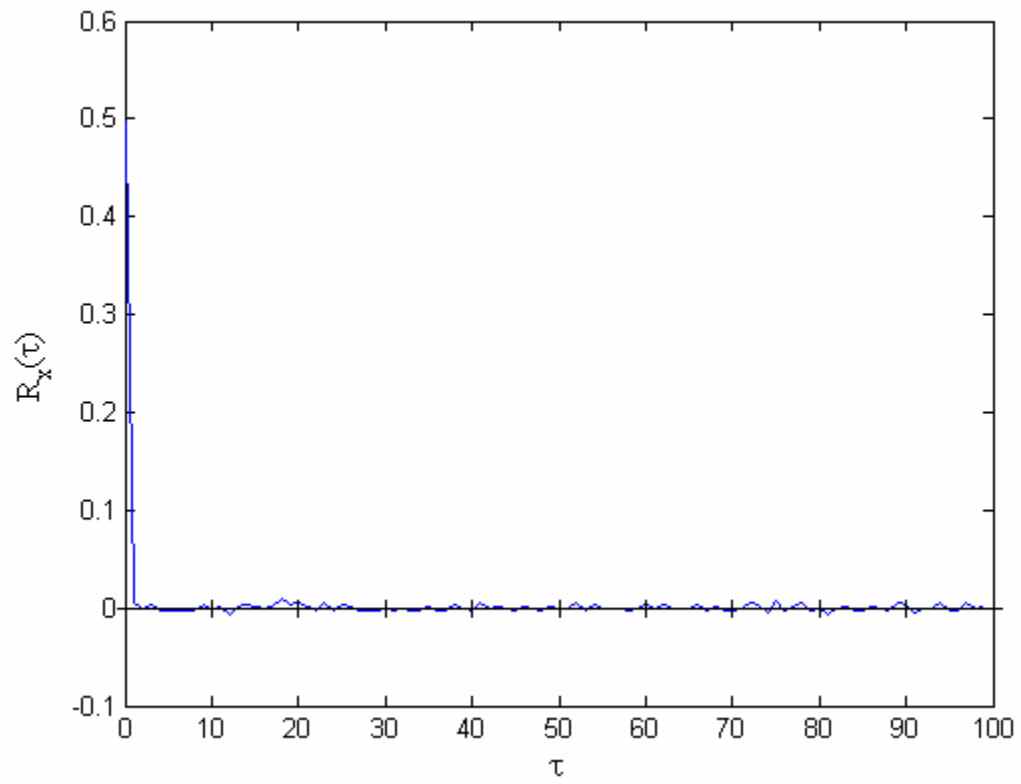


Figure D.4 Autocorrelation of a Random Series